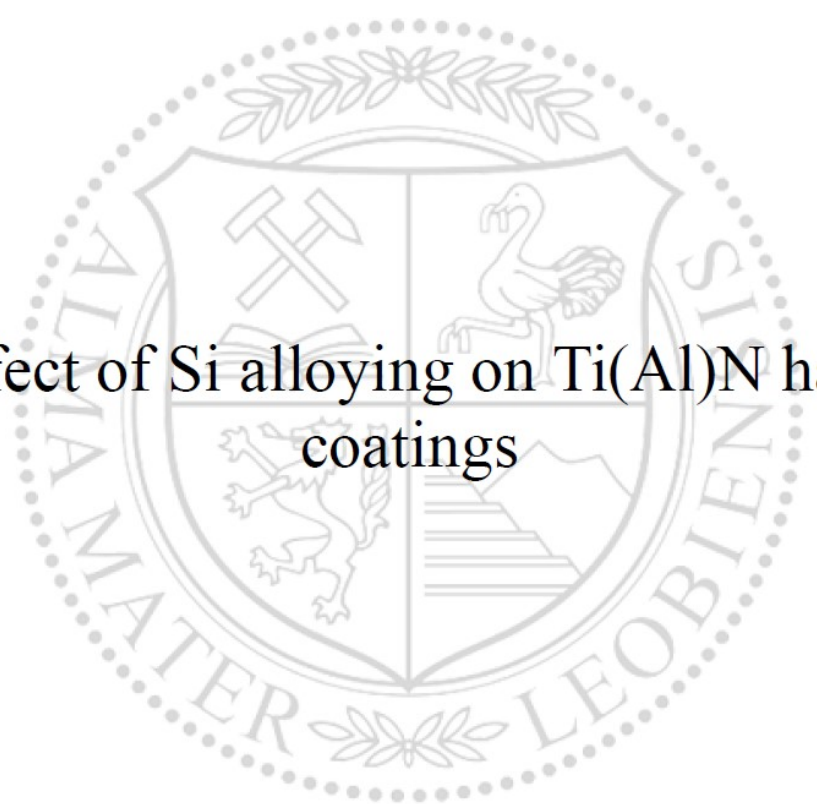




Chair of Functional Materials and Materials Systems

Doctoral Thesis



Effect of Si alloying on Ti(Al)N hard  
coatings

Dipl.-Ing. Yvonne Moritz, BSc.

April 2023



**MONTANUNIVERSITÄT LEOBEN**  
www.unileoben.ac.at

**AFFIDAVIT**

I declare on oath that I wrote this thesis independently, did not use other than the specified sources and aids, and did not otherwise use any unauthorized aids.

I declare that I have read, understood, and complied with the guidelines of the senate of the Montanuniversität Leoben for "Good Scientific Practice".

Furthermore, I declare that the electronic and printed version of the submitted thesis are identical, both, formally and with regard to content.

Date 03.04.2023

*Yvonne Moritz*

Signature Author  
Yvonne Moritz

## Acknowledgments

First of all, I am sincerely grateful to my supervisor Priv.-Doz. Dr. Nina Schalk for giving me the opportunity to conduct this thesis within the Christian Doppler Laboratory for Advanced Coated Cutting Tools. Also, I would like to deeply thank her for the countless helpful corrections of my drafts, her great support, valuable advice, encouragement and guidance throughout the years of my dissertation project, which greatly helped me to push my own limits in becoming a better researcher. Furthermore, I would like to express my gratitude to Prof. Dr. Christian Mitterer for the possibility to carry out my research work at the Chair of Functional Materials and Materials Systems, for his valuable advice and input on many challenging research questions. Also, I would like to thank Prof. Dr. Jozef Keckes for being my mentor for this thesis.

Special thanks goes to Dr. Michael Tkadletz and Dr. Christian Saringer for their constant support with various measurement techniques, fruitful discussions on different research topics, for their great input when correcting my drafts and for taking me on an exciting and informative trip to the synchrotron radiation facility in Hamburg.

Furthermore, I would like to express my gratitude to Dr. Christoph Czettel and Dr. Markus Pohler from Ceratizit Austria for the countless helpful discussions during our project meetings and for the pleasant cooperation throughout the last years.

I want to thank all of my colleagues at the Chair of Functional Materials and Materials Systems, who made working at the Institute a both fun and informative experience. Special thanks to my coworkers Dr. Christina Kainz, Dr. Helene Waldl and Dr. Fabian Konstantiniuk for making my PhD studies an unforgettable and great time.

Many thanks to my family and especially to my parents, without whom I would not be where I am today. Thank you Jenny, for not only being the best twin sister but also my best friend, for always believing in me and for helping me to overcome any obstacles

when feeling overburdened. Special thanks to my dear friends Carina, Kathi, Elli and Sabsi for never doubting me and for making me laugh in stressful times.

Last but certainly not least I would like to thank the most important person in my life, my fiancé Florian. Thank you for taking this PhD journey together with me, for your endless support and your great patience, for making me believe in myself when struggling with self-doubts and above all, thank you for your love.

The financial support by the Austrian Federal Ministry for Digital and Economic Affairs and the National Foundation for Research, Technology and Development is gratefully acknowledged.

*“Nothing in life is to be feared, it is only to be understood. Now is the time to understand more, so that we may fear less.”*

Marie Curie

## Abstract

Physical and chemical vapor deposited protective hard coatings are commonly used to enhance the lifetime and performance of cutting tools. These protective coatings need to fulfill certain requirements such as high hardness, good wear resistance and fracture toughness as well as a high thermal stability and oxidation resistance in order to withstand extreme conditions during machining applications.

The aim of the present work was to develop an in-depth understanding of the structure-property relationship of the Ti(Al,Si)N hard coating system by applying a wide range of advanced characterization techniques. In a first step, the microstructure of the Ti(Al,Si)N coating system was investigated in detail and correlated with the chemical composition and mechanical properties including fracture toughness and fracture stress. Addition of Si led to a fine-grained and nanocomposite structure for both TiSiN and TiAlSiN coatings, which exhibited an identical high hardness of ~40 GPa. Moreover, for the TiAlSiN coating with an Al metal fraction of 14 % the fracture stress and toughness were significantly enhanced compared to the Al-free coating.

Since also the oxidation resistance of protective hard coatings is essential for their performance in cutting applications, in a next step, the oxidation mechanism of TiSiN coatings was illuminated in detail by conducting *in-situ* synchrotron X-ray diffraction measurements and high-resolution scanning transmission electron microscopy studies. It was found that during oxidation of the nanocomposite TiSiN coatings - consisting of nanocrystalline TiN grains embedded in an amorphous SiN<sub>x</sub> (a-SiN<sub>x</sub>) phase - both, rutile and anatase TiO<sub>2</sub> are formed up to a temperature of ~1020 °C. Above this temperature, the transformation of the metastable anatase TiO<sub>2</sub> phase to the stable rutile TiO<sub>2</sub> modification starts. Deposition of a three-layer model system consisting of SiN<sub>x</sub>/TiN/SiN<sub>x</sub> by magnetron sputtering allowed to gain further insight into the influence of the thickness of the a-SiN<sub>x</sub> tissue phase on the oxidation resistance of TiSiN coatings. Here, it was shown that a higher thickness of the SiN<sub>x</sub> layers correlates with an enhanced oxidation resistance

of the crystalline TiN layer, the former being significantly more resistant to oxidation than the crystalline TiN phase. Moreover, the effect of the addition of small amounts of Al on the oxidation resistance of TiSiN coatings was evaluated by assessing the oxidation mechanism of two powdered TiAlSiN coatings with different Al contents by *in-situ* X-ray diffraction. A higher Al content could be related to higher fractions of anatase TiO<sub>2</sub>, being a result of suppressed grain growth during oxidation.

In summary, this thesis establishes the relationship between chemical composition, microstructure and mechanical properties of the Ti(Al,Si)N coating system and further provides a comprehensive understanding of the oxidation mechanism of Ti(Al)SiN coatings. Additionally, the importance of the combinatorial application of advanced characterization techniques for the detailed analysis of protective hard coatings is highlighted.



## Kurzfassung

Mittels physikalischer und chemischer Gasphasenabscheidung synthetisierte Hartstoffschichten werden häufig eingesetzt, um die Lebenszeit und Leistung von Schneidwerkzeugen zu verbessern. Diese Hartstoffschichten müssen bestimmte Anforderungen erfüllen, wie z.B. eine hohe Härte, gute Verschleißbeständigkeit und Bruchzähigkeit, sowie eine gute thermische Stabilität und Oxidationsbeständigkeit.

Das Ziel der vorliegenden Arbeit war es, mit Hilfe einer Auswahl an modernen Charakterisierungsmethoden ein tiefgreifendes Verständnis für den Zusammenhang von Mikrostruktur und Eigenschaften von Ti(Al,Si)N Hartstoffschichten zu entwickeln. Der erste Schritt dieser Arbeit bestand darin, die mechanischen Eigenschaften einschließlich der Bruchzähigkeit und Bruchfestigkeit des Ti(Al,Si)N Schichtsystems zu evaluieren und mit der jeweiligen chemischen Zusammensetzung und Mikrostruktur zu korrelieren. Sowohl TiSiN als auch TiAlSiN Schichten wiesen eine sehr feinkörnige, Nanokomposit Struktur und eine idente hohe Härte von ~40 GPa auf. Die TiAlSiN Schicht mit einem Al Gehalt im metallischen Gitter von 14 % zeigte darüber hinaus signifikant verbesserte Brucheigenschaften verglichen mit der Al-freien Schicht.

Da die Oxidationsbeständigkeit von verschleißfesten Hartstoffschichten einen maßgeblichen Einfluss auf die Leistung des Schneidwerkzeugs hat, bestand der nächste Schritt dieser Arbeit darin, den Oxidationsmechanismus von TiSiN Schichten im Detail zu verstehen, indem *in-situ* Synchrotron Röntgenbeugungs-Experimente sowie hochauflösende Rastertransmissionselektronenmikroskopie Messungen durchgeführt wurden. Es zeigte sich, dass während der Oxidation von Nanokomposit TiSiN Schichten - welche aus nanokristallinen TiN Körnern umgeben von einer amorphen SiN<sub>x</sub> (a-SiN<sub>x</sub>) Phase bestehen - zwei Phasen, nämlich Rutil und Anatas TiO<sub>2</sub>, bis zu einer Temperatur von ~1020 °C gebildet werden. Wenn diese Temperatur überschritten wird, wandelt sich die metastabile Anatas TiO<sub>2</sub> Phase in die stabile Rutil TiO<sub>2</sub> Modifikation um. Die Abscheidung eines dreilagigen SiN<sub>x</sub>/TiN/SiN<sub>x</sub> Modell Schichtsystems mittels

Magnetronspütern erlaubt darüber hinaus den Einfluss der Dicke der  $\alpha$ -SiN<sub>x</sub> Phase auf die Oxidationsbeständigkeit von TiSiN Schichten zu untersuchen. Hierbei wurde beobachtet, dass eine verbesserte Oxidationsbeständigkeit der kristallinen TiN Lage mit einer höheren Dicke der SiN<sub>x</sub> Lagen korreliert, wobei letztere verglichen mit der kristallinen TiN Phase eine signifikant bessere Oxidationsbeständigkeit aufweisen. Des Weiteren wurde der Effekt der Zugabe kleiner Mengen Al auf die Oxidationsbeständigkeit von TiSiN Schichten untersucht, indem wiederum der Oxidationsmechanismus von zwei TiAlSiN Schichten mit unterschiedlich niedrigem Al Gehalt mittels *in-situ* Röntgenbeugung untersucht wurde. Ein etwas höherer Al Gehalt stand hierbei im Zusammenhang mit einer höheren Quantität der Anatas TiO<sub>2</sub> Phase, was auf ein unterdrücktes Kornwachstum während der Oxidation zurückgeführt wurde.

Zusammenfassend demonstrieren die wissenschaftlichen Ergebnisse, die in dieser Dissertation präsentiert werden, den Zusammenhang zwischen chemischer Zusammensetzung, Mikrostruktur und mechanischen Eigenschaften des Ti(Al,Si)N Schichtsystems und erlauben darüber hinaus ein detailliertes Verständnis des Oxidationsmechanismus von Ti(Al)SiN Schichten. Des Weiteren wird in dieser Arbeit die Bedeutung der Kombination mehrerer moderner Charakterisierungsmethoden zur umfassenden Untersuchung von Hartstoffschichten hervorgehoben.

# Content

1	Introduction .....	1
2	Coating deposition.....	3
2.1	Cathodic arc evaporation.....	3
2.2	Magnetron sputter deposition .....	4
2.3	Coating growth .....	6
3	Protective hard coating materials .....	10
3.1	Ti(Si)N coatings.....	10
3.2	TiAl(Si)N coatings .....	15
4	Advanced characterization techniques.....	18
4.1	<i>In-situ</i> synchrotron X-ray diffraction .....	18
4.2	X-ray photoelectron spectroscopy .....	19
5	Summary and Conclusion .....	23
6	References.....	25
7	Publications.....	36
7.1	List of included publications.....	36
	Publication I.....	37
	Publication II .....	62
	Publication III.....	91
	Publication IV.....	114

# 1 Introduction

The ever increasing industrial demands in the market sector for protective hard coatings used for cutting applications lead to a continuous search for cost-efficient coating systems with enhanced lifetime and cutting performance [1]. A common method to deposit these protective coatings onto the respective cutting tools is physical vapor deposition (PVD) [2,3].

For several decades, TiN hard coatings have been commonly used as protective coatings in the cutting industry, owing to their reasonable hardness of ~20-30 GPa, good wear resistance and attractive golden color [4–7]. However, especially the rather low oxidation resistance of 500-550 °C limits the use of these binary coatings in severe machining applications in ambient air [8]. A common strategy to overcome this drawback is the addition of further elements to TiN such as Al, Si, B or C [8–10]. TiAlN coatings, for example, have shown to exhibit a retarded oxidation onset compared to TiN by ~250 °C and additionally show improved mechanical properties such as an increased hardness up to ~37 GPa [8,11,12]. Furthermore, TiSiN coatings have attracted special attention due to their complex nanocomposite structure, consisting of nanocrystalline TiN grains embedded in an amorphous SiN<sub>x</sub> (a-SiN<sub>x</sub>) matrix phase [13–15]. The presence of the a-SiN<sub>x</sub> phase leads to favorable properties of the TiSiN system such as high hardness values above 40 GPa, high oxidation resistance of ~800 °C, and an increased thermal stability under inert conditions up to 1300 °C [16–18]. Due to the complex microstructure of Ti(Al)SiN coatings, in-depth analysis of coating properties requires the application of a wide range of advanced characterization techniques including high-resolution and *in-situ* characterization methods.

The aim of this thesis is to push the limits of the present understanding of the complex Ti(Al)SiN coating system within the hard coating community. Hereby, special focus was placed on revealing the correlation between microstructure and mechanical properties and on understanding the oxidation mechanism of PVD Ti(Al)SiN coatings in

detail. Therefore, in Publication I, the relationship between chemical composition, microstructure and mechanical properties such as hardness, fracture stress and fracture toughness of Ti(Al,Si)N coatings is illuminated, giving insight into the suitability of this coating system for various cutting applications [19]. Furthermore, in publication II, a thorough *in-situ* synchrotron X-ray diffraction (XRD) study on the temperature-dependent phase evolution of TiSiN coatings during oxidation is presented. Additionally, the complex microstructure of both the as-deposited and oxidized nanocomposite TiSiN coatings is illuminated by means of high-resolution scanning transmission electron microscopy [17]. Further insight into the oxidation mechanism of TiSiN coatings is provided by depositing a three-layer model coating system consisting of SiN<sub>x</sub>/TiN/SiN<sub>x</sub> described in publication III. Here, the efficiency of the shielding effect of the a-SiN<sub>x</sub> phase against oxidation of TiN is evaluated in dependence of the thickness of the SiN<sub>x</sub> layers [20]. Finally, in order to analyze the alterations in oxidation mechanism occurring when adding Al to TiSiN, another *in-situ* XRD oxidation study is presented in publication IV, highlighting the oxidation behavior of two TiAlSiN coatings with different low Al content [21].

## 2 Coating deposition

Protective hard coatings are commonly synthesized by physical vapor deposition (PVD). PVD is a stochastic process where solid target materials are brought to the vapor phase by either thermal evaporation or by sputtering with gas ions. Subsequently, the material is transported from the vapor source towards the substrate [22]. The vapor then condenses on the substrate surface, leading to nucleation and coating growth [22,23]. PVD is a line-of-sight process, meaning that the substrate is only coated on the side, which is facing the target [1]. In addition to the working gas (e.g. Ar), also reactive gases such as N<sub>2</sub> or O<sub>2</sub> can be introduced into the deposition chamber in order to form nitride or oxide coatings, respectively [24]. Coatings synthesized by PVD are usually deposited under conditions far from thermodynamic equilibrium and frequently exhibit characteristics such as compressive residual stresses, a small grain size, high defect densities and metastable phases [3]. One way to control these microstructural features is by applying a negative bias voltage between the substrate holder and the deposition chamber, which increases the kinetic energy of the ions impinging on the substrate surface [1,3,25]. Two frequently used PVD methods for the deposition of hard coatings are cathodic arc evaporation (CAE) and magnetron sputter deposition. Both methods were used to deposit coatings within this work and the working principles will be described in the following.

### 2.1 Cathodic arc evaporation

The evaporation of target material is achieved by applying a high current and low voltage between the target material, acting as the cathode and the chamber wall being the anode. The discharge is triggered by creating a short circuit between the two electrodes, leading to the formation of a nano to micrometer sized non-stationary spot of high current densities ( $10^6$  to  $10^{12}$  A/m<sup>2</sup>) on the target surface [1,3,26]. This so-called cathode spot extinguishes and reignites rapidly at a random location, resulting in an apparent motion of the spot over the target surface. The cathode spot motion can be guided by magnetic fields behind the target and is confined by an insulating border between the target and

the chamber wall [26]. Due to the high current densities and consequently high local temperatures at the target surface, target material and electrons are evaporated in explosion-like events, leading to high ionization rates up to 100 % of the target material, which is beneficial for the formation of dense and wear resistant coatings [1,3,26,27]. A major disadvantage of CAE is the emission of droplets of molten target material, which are created from the cathode spots and can be incorporated as defects in the growing coating [3]. Droplets in the coating can be detrimental to the coatings properties, as they cause the formation of voids and microstructural coarsening, presenting mechanically weak spots, as well as diffusion paths for O and also an increased surface roughness [1,27–29]. One possibility to avoid the incorporation of droplets into the coating is by applying magnetic filtering. Hereby, the magnetic field forces ions to follow a specific bend path, while the heavier droplets cannot follow the path due to the higher mass to charge ratio and are thus filtered from the ion flux [27].

## 2.2 Magnetron sputter deposition

Magnetron sputtering is the evaporation of atoms from a solid target material by momentum transfer of highly energetic ions bombarding the target surface [30]. The degree of ionization of the ejected species is low and mainly neutral atoms are ejected. The ion bombardment is provided by an inert working gas (e.g. Ar), which is introduced into the deposition chamber at pressures in the range of  $10^{-3}$  to  $10^{-2}$  mbar. By applying a voltage between the target and the deposition chamber wall, a glow discharge is ignited, which results in the ionization of the working gas and consequently the formation of a plasma. The ions of the working gas impinging on the target surface create a collision cascade in the target material that ejects target atoms with energies in the range of 10 to 40 eV [3,31]. The deposition rate of magnetron sputtering is increased by placing permanent magnets behind the target, which generate a magnetic field that confines electrons in the vicinity of the target. Thus, the ionization rate is increased in this region due to electron impact ionization, which densifies and concentrates the plasma and

consequently increases the sputter rate significantly [32]. Furthermore, substrate heating due to electron bombardment is decreased by this technique [3]. Generally, there are two different magnetic field configurations that can be realized between the inner and outer magnets. In a conventional magnetic field configuration, which is called balanced magnetron sputtering, the magnetic field lines loop between the two magnets, which have an identical magnetic field strength [23]. In the unbalanced configuration, the magnetic field strength of one of the magnets is increased, which leads to the formation of magnetic field lines that are extended towards the substrate (Fig. 1). Consequently, also the plasma extends towards the substrate, enabling the ion bombardment of the substrate with low energetic ions, which promotes coating growth [24,33]. Compared to CAE, magnetron sputtering produces smooth coatings without the formation of droplets.

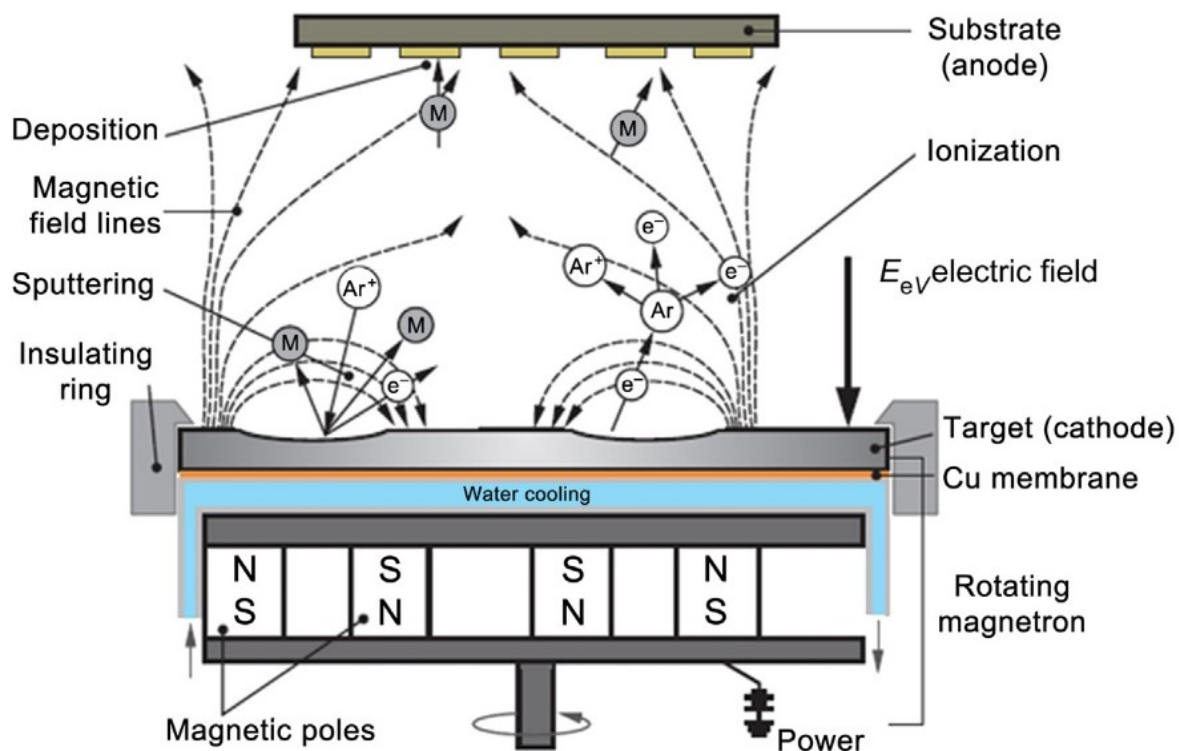


Fig. 1: Schematic of an unbalanced magnetron system. The magnetic field lines reach from the target towards the substrate [3].



### 2.3 Coating growth

The individual processes occurring during coating growth are schematically depicted in Fig. 2. As a first step of coating growth the vaporized particles hit the surface of the substrate and are then either reflected or condensed. On the surface they diffuse and are either desorbed after some dwell time or adsorbed at energetically favorable sites such as lattice defects, point defects, kinks, grain boundaries or already adsorbed atoms [22,24]. The adsorbed atoms can diffuse on the substrate surface and agglomerate to form islands and coat the substrate material. Also, inter-diffusion between the adsorbed particles and the substrate material might occur [22,24,34].

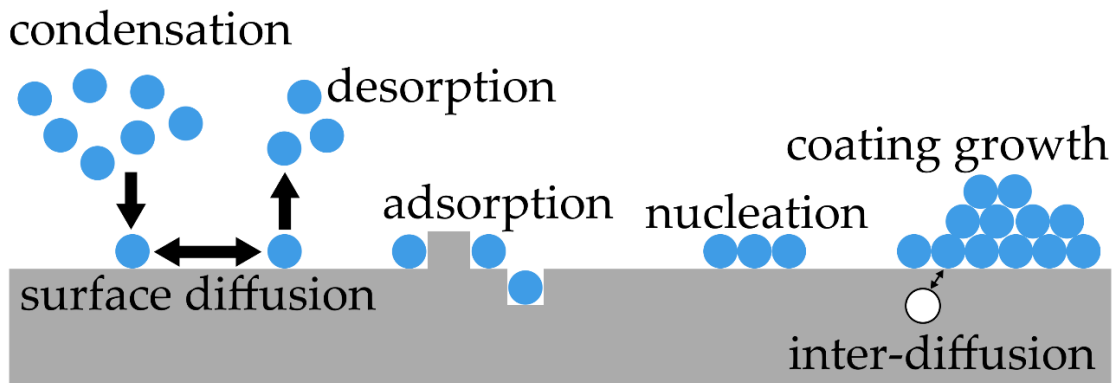


Fig. 2: Schematics of the various processes taking place during coating growth, redrawn after [34].

Depending on the binding energy of the substrate material and the particles, different growth modes are possible, which are shown in Fig.3: layer-by-layer (Frank-Van der Merwe), island-growth (Volmer-Weber), or a combination of these growth modes (Stranksi-Krastanov) [22,24,34]. Frank-Van der Merwe growth occurs when the binding energy between the coating atoms and the substrate is higher than between the coating atoms, which leads to two-dimensional or layer-by-layer growth. In contrast, when the binding energy between the coating atoms surpasses the binding between coating atoms and substrate, islands are formed on the substrate and Volmer-Weber growth occurs. Stranksi-Krastanov growth is a mixed form of layer and island growth. After the initial formation of one or a few monolayers, islands are formed due to energetically favorable

growth conditions [22,24,34]. Hard coatings usually follow the Stranksi-Krastanov growth mode [35].

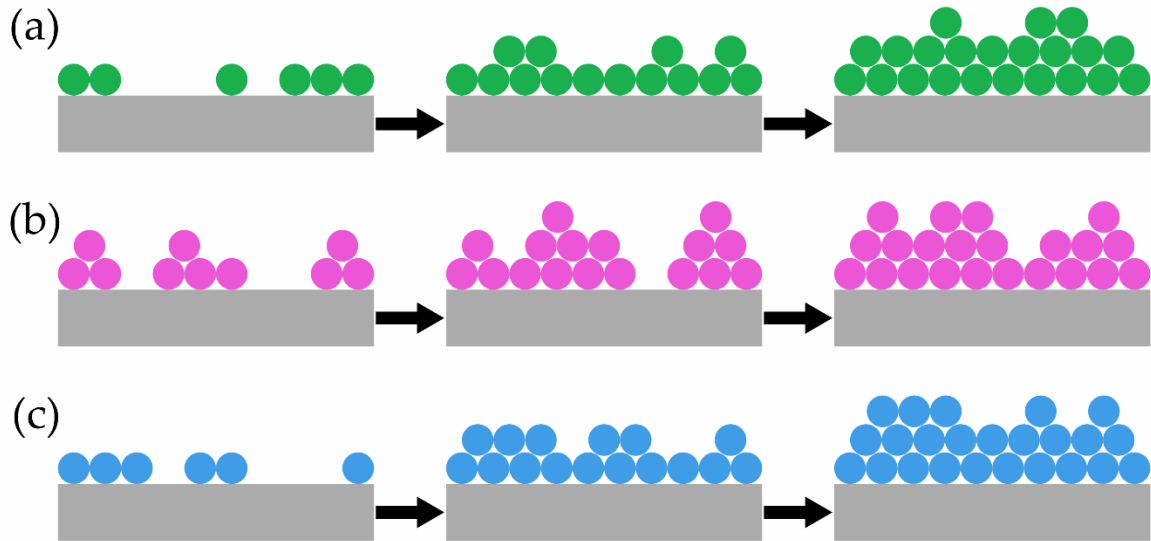


Fig. 3: Schematics of the three different modes of coating growth including (a) layer-by-layer growth (Frank-Van der Merwe), (b) island-growth (Volmer-Weber) and (c) a combination of these two growth modes (Stranski-Kastranow). Redrawn after [24].

Besides the interaction between the coating material and the substrate, the deposition parameters influence the nucleation and growth behavior and consequently the microstructure of the coatings. The relation between the deposition parameters and the microstructure is described by the so-called structure zone models (SZM). The first SZM was developed by Movchan and Demchishin for thick coatings deposited by thermal evaporation [36]. They identified three different zones for the structure of the coating and related them to the homologous temperature ( $T_h$ , i.e. the deposition temperature divided by the melting temperature of the coating material). A porous structure is found in zone 1, which develops due to the low surface mobility of the condensed atoms. In zone 2, dense coatings are formed due to a higher surface mobility and surface diffusion. In zone 3, bulk diffusion and recrystallization is dominant, leading to the formation of large equiaxed grains [36]. In order to extend the applicability of the SZM to other PVD methods, several

authors adapted the SZM by including additional deposition parameters. Thornton included the pressure of the working gas as parameter and introduced a transition zone (zone T) between zone 1 and zone 2, making the model applicable to sputter deposition. The condensed atoms in zone T show a higher surface mobility than in zone 1, leading to competitive growth and a denser fibrous structure [37]. The bias voltage was further included by Messier et al. in another modified model of the SZM [38]. In order to find a generalized SZM that relates the deposition parameters to the coating microstructure, a revised version of Thornton's SZM was proposed by Anders in 2010, which is shown in Fig. 4 [39]. While the already established zones 1-3 and T are still considered, the generalized temperature  $T^*$ , the normalized energy  $E^*$  and the net film thickness  $t^*$  are introduced. In addition to  $T_h$ ,  $T^*$  also includes a thermal shift, stemming from the potential energy of the particles reaching the substrate surface. The pressure of the working gas according to Thornton is replaced by  $E^*$ , which includes atomic scale heating and displacement effects due to the kinetic energy of the incoming particles [25,39]. The third axis  $t^*$  qualitatively displays the effect of the deposition parameters on the coating thickness, including a decrease in coating thickness with increasing  $E^*$  and  $T^*$  due to densification and re-sputtering of the already deposited coating material [39]. Within the diagram, also an area of "negative thickness" can be observed, which is a result of the ion etching process at high ion energies [39].

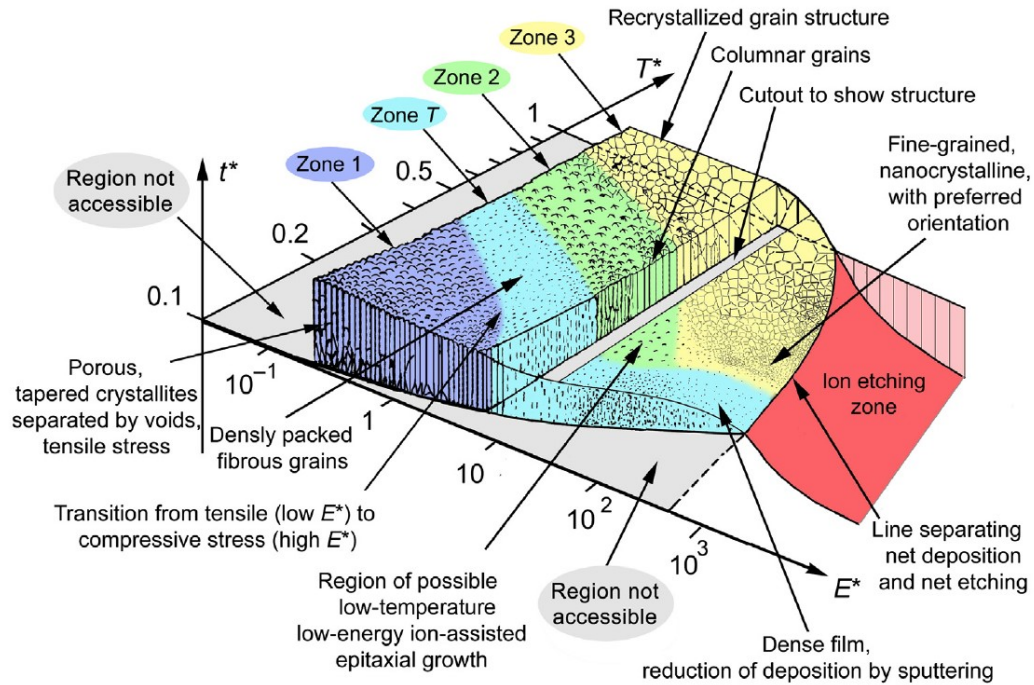


Fig. 4: Structure zone model (SZM) displaying the correlation of deposition parameters and microstructure of the coating. Here,  $T^*$  stands for generalized temperature,  $E^*$  equals the normalized energy flux and  $t^*$  describes the coating thickness [39].

### 3 Protective hard coating materials

Industrial cutting tools are required to withstand extreme conditions during machining applications and are therefore commonly coated with protective hard coatings exhibiting favorable properties such as high hardness, good wear resistance and thermal stability [40]. In order to meet continuously rising industrial demands concerning the performance and lifetime of cutting tools, the search for sophisticated wear protective coatings and their detailed characterization is still an ongoing task, involving various different strategies such as development of new coating materials, tailored coating architectures or optimized deposition conditions [1,40]. One milestone regarding the search for sophisticated coating materials was reached with the development of nanocomposite protective coatings [13,15,41,42]. These nanocomposites typically exhibit a two-phase structure, consisting of a (nano)crystalline phase embedded within an amorphous matrix. The nanocomposite structure of hard coatings was found to promote exceptionally high hardness values, improved wear resistance and enhanced oxidation resistance of the coating material. Optimized hardness values were observed to correlate with a domain size of the nanocrystalline phase below 10 nm and a thickness of the amorphous layer of only a few atomic bond lengths [43]. Popular representatives of nanocomposite coating materials within the hard coating community are TiSiN and TiAlSiN coatings [16,44,45].

In the following, an overview of the characteristics of the PVD coating materials investigated in this work, namely Ti(Si)N and TiAl(Si)N, will be given.

#### 3.1 Ti(Si)N coatings

For several decades, TiN hard coatings have been considered suitable candidates for protective coatings for cutting tools as they exhibit reasonable hardness, good wear resistance and fracture toughness and the ability to act as efficient diffusion barriers [4,6–8,46,47]. TiN coatings are commonly synthesized by chemical vapor deposition (CVD)

and PVD and display a distinct golden color, making it a popular coating system not only for the cutting industry but also for decorative purposes such as jewelry [48–52]. TiN exhibits a face-centered cubic (fcc) crystal structure and the microstructure is often described as columnar grains extending from the substrate towards the surface of the coating [19]. The texture of TiN coatings has been evaluated in detail by several researchers and has shown to be strongly dependent on the deposition method and deposition conditions [53–55]. For example, Mayrhofer et al. evaluated the influence of different deposition parameters, such as the substrate temperature, on the texture evolution of sputter-deposited TiN coatings [54]. A texture development from (111) towards (001) was found for an increasing substrate temperature, due to (001) being the orientation with lowest surface energy, which is preferred for high adatom mobilities during grain growth [54,56]. Knowledge about the texture development of TiN coatings for varying deposition conditions is essential for the cutting industry, since properties such as the wear resistance were found to strongly depend on the preferred orientation of the coating, where a (111) preferred orientation correlates with the highest wear resistance [57].

One major drawback of TiN coatings remains their rather low oxidation stability of ~500-550 °C, limiting their application in high speed machining carried out in ambient air [8]. Therefore, ternary coating systems, which would outperform the binary TiN system, were investigated, leading to the development of TiSiN coatings with highly favourable properties for the cutting industry. When adding Si to TiN, a significantly altered microstructure is obtained, which correlates with improved coating properties in regards to hardness, thermal stability and oxidation resistance [9,13,14,16,41]. In contrast to the typically rather large columnar grains of PVD TiN coatings, TiSiN coatings are frequently described as exhibiting a feather-like and fine-grained structure [16,19,58]. The microstructure of TiSiN can further be labelled as nanocomposite, consisting of nanocrystalline TiN (nc-TiN) grains embedded within an amorphous SiN<sub>x</sub> (a-SiN<sub>x</sub>) tissue

phase [13,15,41]. This amorphous tissue phase can be observed using advanced characterization techniques such as high-resolution scanning transmission electron microscopy (HR-STEM) [16,17,59]. In Fig. 5, typical HR-STEM images taken of a CAE TiSiN coating are depicted. An overview image of the cross-section of the lamella and an image of the cross-section at higher magnification are shown in Fig. 5(a) and (b), respectively, which reveal the typical fine-grained and feather-like structure of the TiSiN coating. Taking a look at even higher resolution in Fig. 5(c), elongated crystalline regions surrounded by the a-SiN<sub>x</sub> tissue phase can be observed, which is more clearly visible in the inverse fast Fourier transformation (IFFT) image (Fig. 5(d)), which proves the nanocomposite structure of this coating system. However, concerning the microstructure of TiSiN coatings, it needs to be pointed out that recent works also consider the possibility of Si being present in both the a-SiN<sub>x</sub> phase and additionally within a TiSiN solid solution, where the Si substitutes for Ti atoms in the lattice [16,17,59]. The formation of a TiSiN solid solution is indicated by a peak shift to higher diffraction angles in the X-ray diffractograms, occurring due to a slight decrease in the stress-free lattice parameter of the nanocrystalline phase when compared to TiN [17,59].

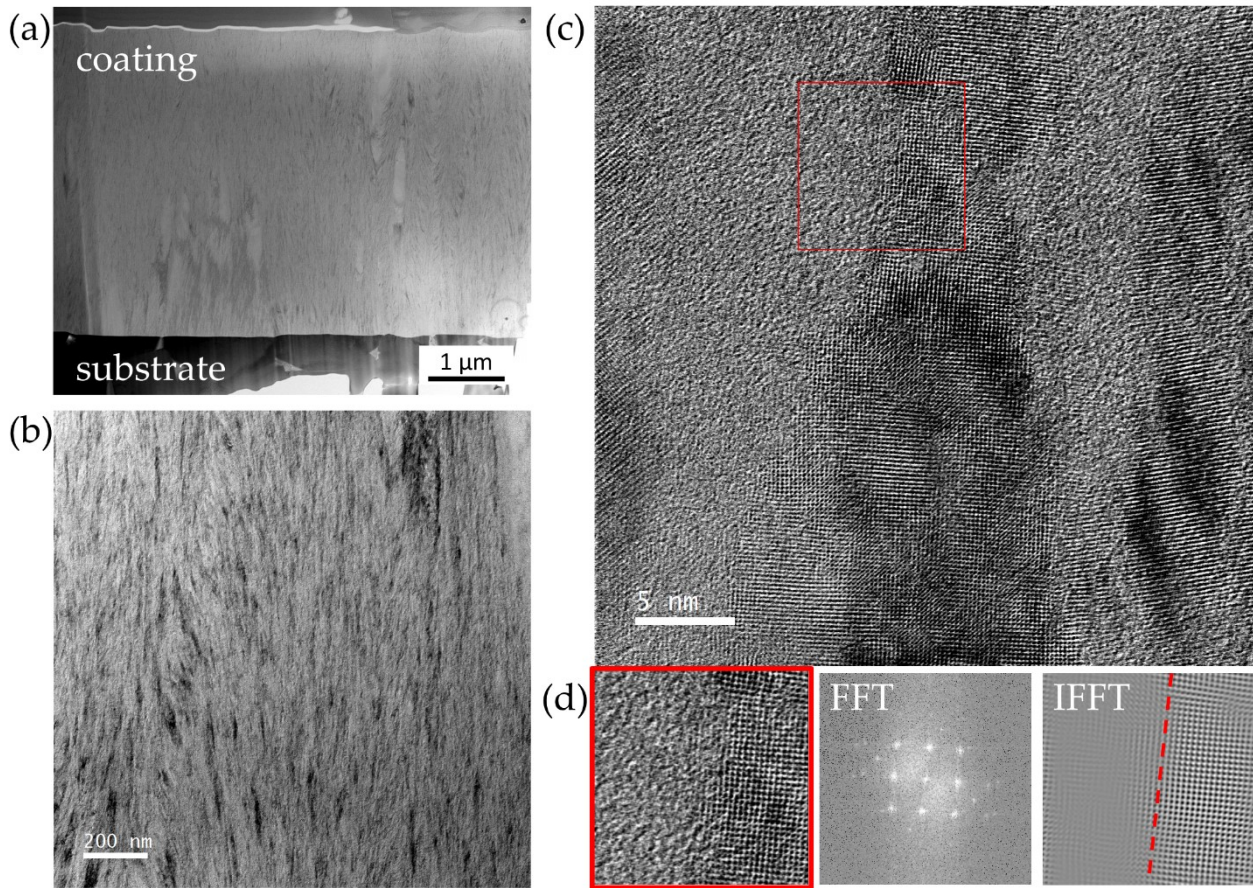


Fig. 5: Scanning transmission electron microscopy (STEM) cross-sectional overview image of a lamella of a TiSiN coating (a) and annular dark-field image of the cross-section of the coating at higher magnification showing a feather-like, fine-grained structure (b). High-resolution scanning transmission electron microscopy (HR-STEM) image revealing elongated crystalline and amorphous regions (c) that can be differentiated and visualized better in the cut-out (red frame) and inverse fast Fourier Transformation (IFFT) shown in (d). Crystalline reflexes stemming from the nanocrystalline face-centered cubic TiN phase are additionally depicted in the fast Fourier Transformation (FFT) (d) [own work].

Adding Si to TiN has commonly shown to result in a change in texture from a (mixed) (111) preferred orientation for TiN to a (200) preferred orientation for TiSiN [19,60,61], which is discussed in detail in Publication I [19]. This phenomenon was attributed to the presence of the  $a\text{-SiN}_x$  phase favouring re-nucleation of [001]-oriented



TiN grains, corresponding to the plane with lowest surface energy for the fcc-phase [19,62].

While for PVD TiN coatings typically hardness values in the range of 20-30 GPa are reported [5,8,19,63,64], PVD TiSiN coatings have shown to reach an exceptionally high hardness above 40 GPa, owing to the presence of the  $\alpha$ -SiN<sub>x</sub> phase [14,18,19,60]. Firstly, the  $\alpha$ -SiN<sub>x</sub> phase is known to hinder grain growth during deposition, resulting in smaller grain sizes and thus an enhanced resistance to plastic deformation. Secondly, the  $\alpha$ -SiN<sub>x</sub> phase limits dislocation movement and grain boundary sliding, again positively impacting the hardness of the TiSiN coating system [15,65].

TiSiN coatings have proven to be thermally stable under inert conditions up to temperatures of ~1300 °C. Only above this value decomposition of the coating material takes place and the formation of TiSi<sub>2</sub>, diamond cubic Si and  $\beta$ -Si<sub>3</sub>N<sub>4</sub> can be found [16]. While for TiN usually significant grain coarsening is observed when annealing at high temperatures of ~1000 °C, this does not become evident for TiSiN coatings. Here, again the  $\alpha$ -SiN<sub>x</sub> acts as an inhibitor for grain growth and thus allows for the preservation of the good mechanical properties (e.g. hardness) of TiSiN coatings even after annealing at high temperatures of ~1000 °C [16]. Since many machining applications take place in ambient air at high temperatures, protective hard coatings are further required to exhibit a sufficient oxidation resistance [66]. The oxidation resistance of TiN coatings up to ~550 °C was frequently regarded a limiting factor for using this coating system in severe machining applications [8], however, TiSiN coatings are able to outperform the binary TiN system by a more than 200 °C higher onset of oxidation [9,18,67]. Already the addition of small amounts of Si in the range of ~1.2 at.% has shown to drastically reduce the thickness of the formed oxide layer after subjecting the coating to oxidation for a specific time [60]. When investigating the TiSiN oxidation mechanism in more detail, Steyer et al. discovered the formation of the metastable anatase TiO<sub>2</sub> phase besides the stable rutile TiO<sub>2</sub> modification [9]. Anatase TiO<sub>2</sub> had not been reported to occur for the

oxidation of binary TiN, thus this phenomenon was assumed to be a result of the addition of Si [9]. The grain refinement and inhibited grain growth at high temperatures due to the presence of the  $\alpha$ -SiN<sub>x</sub> phase was found to be responsible for the occurrence of the anatase TiO<sub>2</sub> phase, which is known to be stabilized at small grain sizes < 11 nm [9,60,68]. In Publication II, the oxidation mechanism of TiSiN coatings was studied in unprecedented detail by means of *in-situ* synchrotron X-ray diffraction (XRD) and the formation of both, anatase and rutile TiO<sub>2</sub> up to a temperature of ~1020 °C was observed. When exceeding this threshold temperature, the metastable anatase TiO<sub>2</sub> transformed into the stable rutile modification, since a critical grain size had been reached at this elevated temperature [17].

### 3.2 TiAl(Si)N coatings

Prior to the establishment of quaternary TiAlSiN coatings as protective coatings for cutting tools, ternary TiAlN coatings had been developed as an improved coating material compared to TiN especially in regards to mechanical properties and oxidation stability [8,69,70]. Up to a certain threshold value of incorporated Al, Ti<sub>1-x</sub>Al<sub>x</sub>N coatings exhibit an fcc-structure and form a metastable solid solution, where Al substitutes for Ti atoms within the lattice [69,71]. Depending on the deposition conditions, the solubility limit of Al within a Ti<sub>1-x</sub>Al<sub>x</sub>N solid solution may vary, whereby the maximum solubility limit for PVD Ti<sub>1-x</sub>Al<sub>x</sub>N coatings was reported to be  $x \leq 0.66$  [11,69,72,73]. When this limit is exceeded, wurtzitic AlN (w-AlN) is formed, which is generally accompanied by a drastic deterioration of the mechanical properties [11,71,74]. Hardness values reported for Ti<sub>1-x</sub>Al<sub>x</sub>N coatings typically range from ~25-37 GPa [11,12] and can further increase when exposing the coatings to temperatures between 600-1000 °C [75,76]. This increase in hardness at elevated temperatures is a result of the age-hardening effect, occurring due to coherency strains caused by spinodal decomposition into fcc-TiN and AlN domains [75,76]. Also the oxidation stability of Ti<sub>1-x</sub>Al<sub>x</sub>N is strongly enhanced compared to TiN by ~250 °C, owing to the formation of an Al<sub>2</sub>O<sub>3</sub> top layer preventing further inwards diffusion of O [8]. Upon striving for even higher thermal stabilities and enhanced mechanical

properties, quaternary coating materials have been developed by addition of further elements to TiAlN, among which especially TiAlSiN coatings have found to be excellent in meeting increasing industrial demands. Similar to TiSiN coatings, TiAlSiN coatings exhibit a nanocomposite structure consisting of nc-TiAlN grains embedded within an a-SiN<sub>x</sub> phase [44,45]. Again, however, the possibility of Si being present in both, the a-SiN<sub>x</sub> phase and the nc-TiAlSiN phase in form of a solid solution needs to be considered [44,77]. As for TiAlN coatings, also for the TiAlSiN coating system incorporation of Al beyond a certain threshold value leads to the formation of w-AlN. The solubility limit of Al within the solid solution, has been shown to decrease when adding Si to TiAlN, since Si is known to foster the formation of w-AlN [44,78,79]. Regarding the mechanical properties of the TiAlSiN coating system, high hardness values in the range of ~30-40 GPa are reported [19,44,80]. Besides the hardness also fracture toughness and fracture stress are crucial mechanical properties for obtaining an optimized cutting performance. In Publication I, it is demonstrated that TiAlSiN coatings with a rather low Al metal fraction of 14 % (Ti<sub>0.70</sub>Al<sub>0.14</sub>Si<sub>0.16</sub>N) exhibit an equally high hardness of ~40 GPa as found for Al-free Ti<sub>0.84</sub>Si<sub>0.16</sub>N coatings, but at the same time show drastically improved fracture stress and toughness. The enhanced fracture properties were on the one hand attributed to the fine grained microstructure as a result of the Si addition and on the other hand to a local stress-induced transformation of fcc-AlN to w-AlN during fracture [19].

The oxidation resistance upon addition of Si to TiAlN coatings has been evaluated by several researchers and a decrease of the thickness of the formed oxide layer was already observed when adding only 2 at.% of Si to the TiAl target material [81]. Also for TiAlSiN coatings with higher Si contents of 8-10 % of the metal fraction a strongly enhanced oxidation resistance compared to Si-free TiAlN was found, which was attributed to a smaller grain size of the nanocomposite TiAlSiN coating system and to the formation of two efficient diffusion barrier layers for O, namely Al<sub>2</sub>O<sub>3</sub> and SiO<sub>2</sub> [78,82]. Since literature had been lacking an investigation of the oxidation mechanism for TiAlSiN

coatings with varying Al content but constant Si content, this research question was addressed in Publication IV [21]. *In-situ* XRD studies of two powdered  $\text{Ti}_{37}\text{Al}_2\text{Si}_7\text{N}_{54}$  and  $\text{Ti}_{33}\text{Al}_6\text{Si}_7\text{N}_{54}$  coatings revealed the formation of a significantly higher quantity of the anatase  $\text{TiO}_2$  phase for the coating with higher Al content of 6 at.%. This observation was attributed to a more efficiently suppressed grain growth during oxidation for the  $\text{Ti}_{33}\text{Al}_6\text{Si}_7\text{N}_{54}$  coating [21].

## 4 Advanced characterization techniques

### 4.1 *In-situ* synchrotron X-ray diffraction

Hard coatings have to withstand high temperatures that arise during machining applications, thus making it mandatory to be aware of the high temperature and oxidation behavior of the respective coating material [83]. Although it is possible to determine the temperature-dependent phase evolution *in-situ* and *ex-situ* under non-oxidizing and oxidizing conditions on laboratory scale X-ray diffractometers [66,84,85], the low energy resolution, low brilliance and usually slow data acquisition time of these diffractometers do not present optimal settings for precise measurements. These drawbacks of laboratory X-ray diffractometers can be overcome by employing *in-situ* synchrotron XRD [86]. This technique offers a precise method to determine the temperature-dependent phase evolution during annealing experiments. Coating powders are heated in a furnace, while Debye-Scherrer rings are recorded using a 2D flat-panel detector [86]. The high brilliance of the synchrotron radiation enables fast data acquisition times of only a few seconds, making it possible to determine phase transition temperatures, oxidation behavior and changes in microstructure with a high resolution on the temperature scale [17,86]. The investigation of coating powders instead of compact coatings offers the possibility to investigate the properties of the coating material without interference of the substrate and further allows to correlate the data with other investigation methods, such as differential scanning calorimetry [86]. The measured 2D Debye-Scherrer rings are integrated in azimuthal direction, leading to a set of 1D diffractograms as a function of the temperature. The resulting data can be plotted in a so-called phase plot, which is depicted exemplarily for the oxidation of a CAE TiSiN coating in Fig. 6. The diffractograms contain information about the qualitative phase evolution, given by the peak position of the individual phases. In order to quantify the phase composition, the peak intensity and peak width has to be taken into account and patterns can be simulated and refined using Rietveld refinement [87,88].

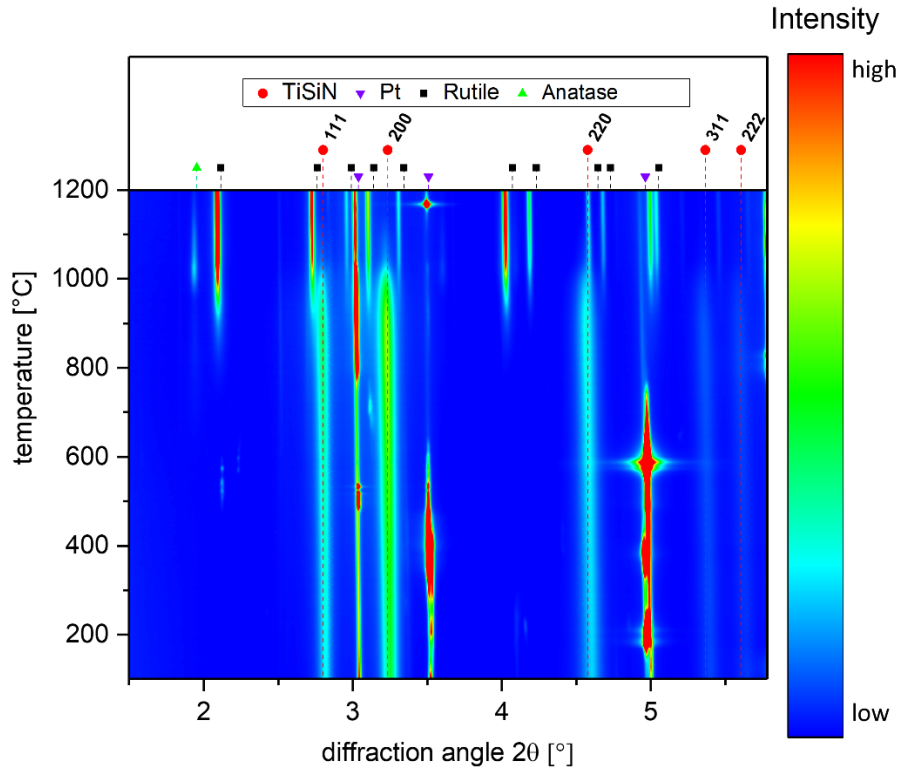


Fig. 6: Phase plot showing the color-coded intensity of the azimuthally integrated 1D diffractograms of a cathodic arc evaporated powdered TiSiN coating as a function of the oxidation temperature. The Pt peaks arise due to placing the powdered sample into a Pt crucible [own work].

## 4.2 X-ray photoelectron spectroscopy

One problem that is frequently encountered when characterizing nanocomposite coatings consisting of nanocrystalline and amorphous regions, is the impossibility to monitor the X-ray amorphous phases by XRD, as shown for *in-situ* XRD oxidation studies of Ti(Al)SiN coatings in Publication II or Publication IV [17,21]. In order to gain further insight whether also the a-SiN<sub>x</sub> phase is oxidized at a specific temperature, X-ray photoelectron spectroscopy (XPS) is a suitable method.

XPS is a characterization method to determine the chemical composition and binding state of electrons of the investigated material. During the measurement, the surface of the sample is irradiated using mono-energetic photons with energies in the soft X-ray spectrum, usually ranging from 1-10 keV [89]. Due to the photoelectric effect, so-

called photoelectrons are emitted from the sample and their kinetic energy ( $E_{kin}$ ) is detected [90]. Excitation energies in the soft X-ray spectrum are usually sufficient to excite core-level electrons from the atoms. Although the penetration depth of the X-rays is in the range of few  $\mu\text{m}$ , photoelectrons originating from a depth of only about a few atomic layers are detected, which can be related to the small mean-free-path of electrons in solids [89,91,92]. Therefore, XPS is a surface sensitive investigation method, giving insight only into the top atomic layers of the coating material. An illustration of the energy levels relevant for XPS is shown in Fig. 7. The  $E_{kin}$  of the detected photoelectrons can be related to the binding energy ( $E_b$ ) of the electrons using the equation

$$E_b = h\nu - E_{kin} - \Phi_{spec}, \quad (1)$$

whereby  $h\nu$  is the excitation energy and  $\Phi_{spec}$  the work function of the detector. In XPS of solid materials,  $E_b$  is expressed relative to the Fermi level of the material. The Fermi levels of the sample and the detector are aligned, which is the case for electrically conducting materials. Although the work function of the sample ( $\Phi_s$ ) has to be overcome by the excited photoelectron, only  $\Phi_{spec}$  is needed for the evaluation of  $E_b$  of the sample [93]. The investigation of semiconducting or insulating samples with XPS is also possible, although surface charging effects and the unknown Fermi level of the sample have to be taken into account. One common approach to investigate these samples is by depositing a conducting layer (mostly Au) on top on the sample to calibrate the energy spectrum with the well-known Au core level energies. Another method is to calibrate the energy spectrum by measuring a well-known feature of the binding energy spectrum of the sample, e.g. C 1s peak or the valence band edge [93,94].

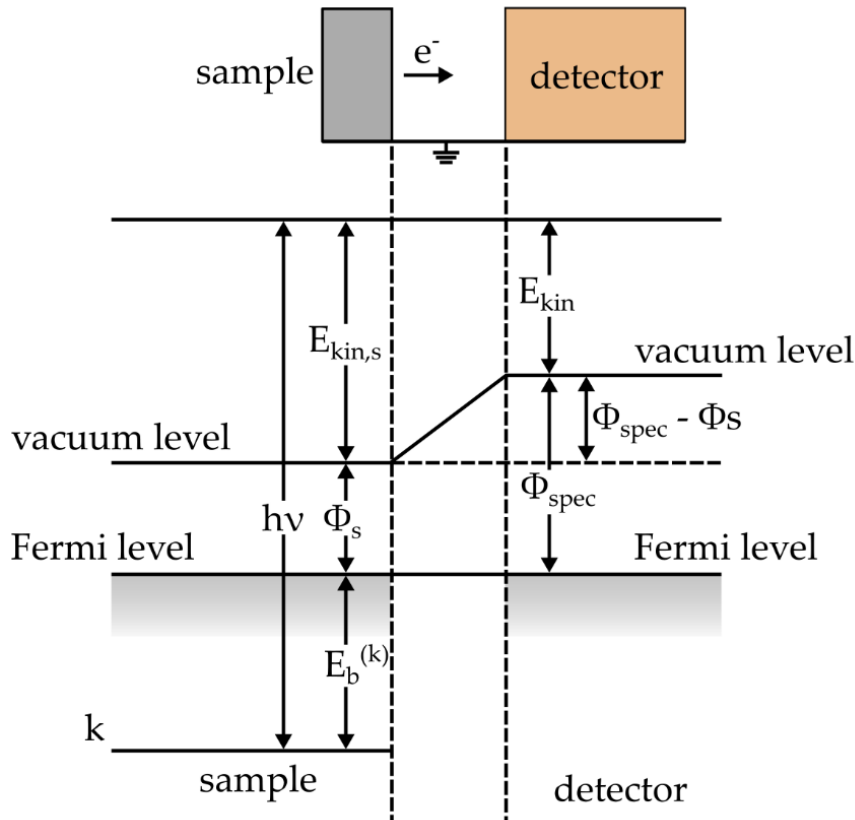


Fig. 7: Sample and spectrometer energy levels for a conducting sample. The excitation energy of the incoming photons is given by  $h\nu$ . The kinetic energy  $E_{kin}$  of the emitted photoelectrons is detected by the spectrometer with a work function  $\Phi_{spec}$ . The binding energy  $E_b$  of the photoelectrons is related to the  $E_{kin}$  by the relation  $E_b = h\nu - E_{kin} - \Phi_{spec}$ . Redrawn after [93].

In order to compare XPS spectra that were recorded with different excitation energies, the measured intensity, i.e. the amount of collected electrons on the detector, is plotted over  $E_b$  [94]. The core level energies of the electrons depend not only on the nuclear charge of the atoms that comprise the investigated material, but also on the chemical environment of these atoms. Owing to the different bonds, the core level electrons are exposed to a different potential energy, resulting in a chemical shift in the  $E_b$  spectrum [89,93]. An example of a chemical shift in an XPS spectrum due to the chemical environment is displayed by the Si 2p peak in Fig. 8. A peak shift in  $E_b$  of approximately



4 eV can be seen when measuring the Si 2p peak of Si present within the SiO<sub>2</sub> compound compared to the measurement of pure Si [93,95].

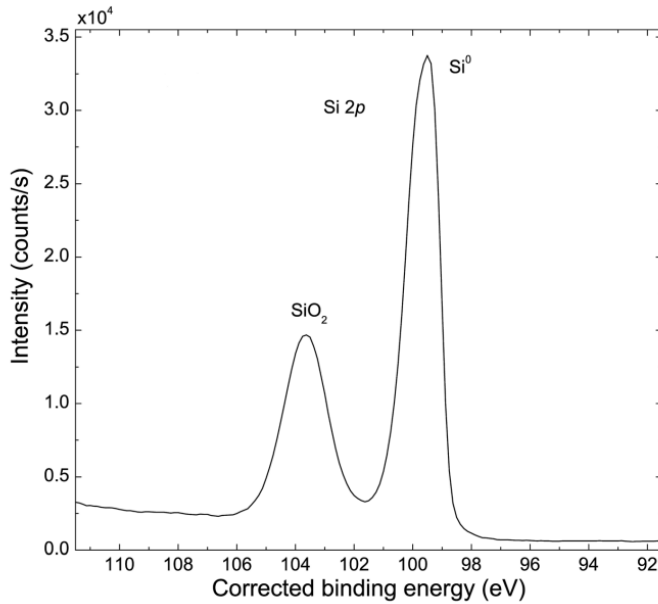


Fig. 8: Binding energy spectrum of the Si 2p peak of a Si (100) sample. Depending on the chemical environment, the peak shifts from pure Si at 99.15 eV to SiO<sub>2</sub> at 103.4 eV [95].

In order to extend the capabilities of XPS investigations, depth profiles of the sample material can be obtained. There, material is removed from the sample surface by ion sputtering with e.g. Ar<sup>+</sup> ions and XPS spectra are recorded in cyclic progression [94]. This method is especially powerful to determine the energy states of multilayer coatings as a function of the coating thickness [96–98], although special care has to be taken when recording and evaluating the data [99]. Sputtering might lead to changes in E<sub>b</sub> and the chemical composition, peak broadening and the appearance of new features in the spectrum. The significance of these changes depends on the sputter conditions, as well as on the investigated material [100].

## 5 Summary and Conclusions

The aim of this work was to thoroughly characterize Ti(Al,Si)N hard coatings using a variety of advanced characterization techniques, thereby allowing to establish a detailed understanding of the relationship between chemical composition, microstructure and mechanical and thermal properties of the coating material. In a first step of this thesis in Publication I, the microstructure of the Ti(Al,Si)N coating system was analyzed in detail and correlated with the fracture properties evaluated by micromechanical bending tests. A similar fine-grained, feather-like and nanocomposite structure was attained when adding small amounts of Al to TiSiN and additionally an identical high hardness of ~40 GPa was found for both TiSiN and TiAlSiN coatings. However, a significant enhancement was observed when taking a look at the fracture stress and toughness of the TiAlSiN coating with an Al metal fraction of 14 % compared to the Al-free TiSiN coatings. This drastic improvement of fracture properties was assumed to be a result of local stress-induced transformation of face-centered cubic AlN to wurtzitic AlN during fracture of the coating.

Special focus of this thesis was further placed on evaluating the oxidation mechanism of Ti(Al)SiN coatings, starting with an *in-situ* synchrotron X-ray diffraction study of a powdered cathodic arc evaporated TiSiN coating, summarized in Publication II. TiSiN was shown to exhibit an excellent oxidation stability up to ~800 °C, upon which the formation of rutile and anatase TiO<sub>2</sub> was found. The quantity of the metastable anatase TiO<sub>2</sub> phase increased up to a temperature of ~1020 °C, above which it transformed into the stable rutile modification, since a critical grain size for the stabilization of anatase was encountered. Additionally conducted differential scanning calorimetry and X-ray photoelectron spectroscopy investigations gave insight into the oxidation behavior of the amorphous SiN<sub>x</sub> (a-SiN<sub>x</sub>) phase, revealing a significantly retarded oxidation compared to the nanocrystalline TiN phase. The influence of the a-SiN<sub>x</sub> phase on the oxidation resistance was evaluated in more detail in Publication III by deposition of a three-layer

model coating system consisting of  $\text{SiN}_x/\text{TiN}/\text{SiN}_x$ . Investigation of these magnetron sputtered model coatings deposited with varying  $\text{SiN}_x$  layer thickness revealed an enhanced oxidation stability of the TiN phase for thicker  $\text{SiN}_x$  layers, proving the excellent shielding effect of the a- $\text{SiN}_x$  phase. Furthermore, the a- $\text{SiN}_x$  layers as well as the crystalline TiN layers were found to become porous at elevated temperatures of  $\sim 1200$  °C, enabling oxygen diffusion throughout the coating architecture. In Publication IV, the oxidation mechanism of TiAlSiN coatings with low Al content was assessed. When increasing the Al content from 2 to 6 at.% a significant change in oxidation behavior was observed, meaning that a two-fold increase of the maximum quantity of the anatase  $\text{TiO}_2$  phase was found, which was attributed to a more sufficiently suppressed grain growth during oxidation for the higher Al content. Furthermore, the formed protective  $\text{Al}_2\text{O}_3$  toplayer for the TiAlSiN coating with 6 at.% was shown to break by the growth of  $\text{TiO}_2$  grains after oxidation at 950 °C

The present thesis contributes to a detailed and thorough understanding of the relationship between chemical composition, microstructure and coating properties of the Ti(Al,Si)N coating system. The combinatorial approach of advanced characterization techniques allows to analyze the complex nanocomposite Ti(Al)SiN coatings in previously inaccessible depth.

## 6 References

- [1] N. Schalk, M. Tkadletz, C. Mitterer, Hard coatings for cutting applications: Physical vs. chemical vapor deposition and future challenges for the coatings community, *Surf. Coat. Technol.* 429 (2022) 127949.
- [2] P.H. Mayrhofer, C. Mitterer, Structure/property relations in PVD hard coatings, in: S. Pandalai (Ed.), *Recent Res. Devel. Vac. Sci. Tech., Transworld research network, Trivandrum, 2003*: pp. 71–97.
- [3] C. Mitterer, PVD and CVD Hard Coatings, in: V.K. Sarin (Ed.), *Compr. Hard Mater., Vol. 2*, Elsevier Ltd, Amsterdam, 2014: pp. 449–467.
- [4] P. Hedenqvist, M. Olsson, P. Wallén, Å. Kassman, S. Hogmark, S. Jacobson, How TiN coatings improve the performance of high speed steel cutting tools, *Surf. Coatings Technol.* 41 (1990) 243–256.
- [5] L.C. Hernández, L. Ponce, A. Fundora, E. López, E. Pérez, Nanohardness and Residual Stress in TiN Coatings, *Materials (Basel)*. 4 (2011) 929–940.
- [6] S. Kataria, S.K. Srivastava, P. Kumar, G. Srinivas, Siju, J. Khan, D.V. Sridhar Rao, H.C. Barshilia, Nanocrystalline TiN coatings with improved toughness deposited by pulsing the nitrogen flow rate, *Surf. Coat. Technol.* 206 (2012) 4279–4286.
- [7] J.-E. Sundgren, Structure and properties of TiN coatings, *Thin Solid Films*. 128 (1985) 21–44.
- [8] W. Münz, Titanium aluminum nitride films: A new alternative to TiN coatings, *J. Vac. Sci. Technol. A Vacuum, Surfaces, Film*. 4 (1986) 2717–2725.
- [9] P. Steyer, D. Pilloud, J.F. Pierson, J.P. Millet, M. Charnay, B. Stauder, P. Jacquot, Oxidation resistance improvement of arc-evaporated TiN hard coatings by silicon addition, *Surf. Coatings Technol.* 201 (2006) 4158–4162.
- [10] C. Kainz, N. Schalk, M. Tkadletz, C. Mitterer, C. Czettel, The effect of B and C addition on microstructure and mechanical properties of TiN hard coatings grown by chemical vapor deposition, *Thin Solid Films*. 688 (2019) 137283.

- [11] B. Grossmann, N. Schalk, C. Czettl, M. Pohler, C. Mitterer, Phase composition and thermal stability of arc evaporated  $Ti_{1-x}Al_xN$  hard coatings with  $0.4 \leq x \leq 0.67$ , *Surf. Coat. Technol.* 309 (2017) 687–693.
- [12] M. Ahlgren, H. Blomqvist, Influence of bias variation on residual stress and texture in TiAlN PVD coatings, *Surf. Coat. Technol.* 200 (2005) 157–160.
- [13] S. Vepřek, S. Reiprich, A concept for the design of novel superhard coatings, *Thin Solid Films.* 268 (1995) 64–71.
- [14] S. Veprek, R.F. Zhang, M.G.J. Veprek-Heijman, S.H. Sheng, A.S. Argon, Superhard nanocomposites: Origin of hardness enhancement, properties and applications, *Surf. Coat. Technol.* 204 (2010) 1898–1906.
- [15] S. Vepřek, Conventional and new approaches towards the design of novel superhard materials, *Surf. Coatings Technol.* 97 (1997) 15–22.
- [16] F. Pei, Y.X. Xu, L. Chen, Y. Du, H.K. Zou, Structure, mechanical properties and thermal stability of  $Ti_{1-x}Si_xN$  coatings, *Ceram. Int.* 44 (2018) 15503–15508.
- [17] Y. Moritz, C. Saringer, M. Tkadletz, A. Stark, N. Schell, I. Letofsky-Papst, C. Czettl, M. Pohler, N. Schalk, Oxidation behavior of arc evaporated TiSiN coatings investigated by in-situ synchrotron X-ray diffraction and HR-STEM, *Surf. Coat. Technol.* 404 (2020) 126632.
- [18] A. Mège-Revil, P. Steyer, G. Thollet, R. Chiriach, C. Sigala, J.C. Sánchez-Lopéz, C. Esnouf, Thermogravimetric and in situ SEM characterisation of the oxidation phenomena of protective nanocomposite nitride films deposited on steel, *Surf. Coatings Technol.* 204 (2009) 893–901.
- [19] Y. Moritz, C. Kainz, M. Tkadletz, C. Czettl, M. Pohler, N. Schalk, Microstructure and mechanical properties of arc evaporated Ti(Al,Si)N coatings, *Surf. Coat. Technol.* 421 (2021) 127461.
- [20] Y. Moritz, C. Kainz, P. Peritsch, C. Mitterer, N. Schalk, Oxidation mechanism of sputter deposited model  $SiN_x/TiN/SiN_x$  coatings, *Under Rev. Surf. Coatings*

- Technol. (2023).
- [21] Y. Moritz, C. Saringer, M. Tkadletz, A. Fian, C. Czettl, M. Pohler, N. Schalk, In-situ X-ray diffraction study of the oxidation behavior of arc evaporated TiAlSiN coatings with low Al contents, *Submitt. to Surf. Coatings Technol.* (2023).
- [22] R.F. Bunshah, *Handbook of deposition technologies for films and coatings: Science, technology, and applications*, 2nd ed., Noyes Publications, Park Ridge, N.J., 1994.
- [23] D.M. Mattox, *Handbook of Physical Vapor Deposition (PVD) Processing*, 2nd ed., Elsevier, Oxford, 2010.
- [24] M. Ohring, *Materials Science of Thin Films: Deposition and Structure*, 2nd ed., Academic Press, San Diego, 2002.
- [25] I. Petrov, P.B. Barna, L. Hultman, J.E. Greene, Microstructural evolution during film growth, *J. Vac. Sci. Technol. A*. 21 (2003) 117–128.
- [26] A. Anders, *Cathodic Arcs: From Fractal Spots to Energetic Condensation*, 1st ed., Springer, New York, 2008.
- [27] D.M. Sanders, A. Anders, Review of cathodic arc deposition technology at the start of the new millennium, *Surf. Coatings Technol.* 133–134 (2000) 78–90.
- [28] A. Hörling, L. Hultman, M. Odén, J. Sjöln, L. Karlsson, Thermal stability of arc evaporated high aluminum-content  $Ti_{1-x}Al_xN$  thin films, *J. Vac. Sci. Technol. A Vacuum, Surfaces, Film*. 20 (2002) 1815–1823.
- [29] M. Tkadletz, C. Mitterer, B. Sartory, I. Letofsky-Papst, C. Czettl, C. Michotte, The effect of droplets in arc evaporated TiAlTaN hard coatings on the wear behavior, *Surf. Coatings Technol.* 257 (2014) 95–101.
- [30] D.M. Mattox, Physical vapor deposition (PVD) processes, *Met. Finish.* 100 (2002) 394–408.
- [31] P. Sigmund, Theory of Sputtering. I. Sputtering Yield of Amorphous and Polycrystalline Targets, *Phys. Rev.* 184 (1969) 383–416.
- [32] W.D. Westwood, Sputter Deposition Processes, *MRS Bull.* 13 (1988) 46–51.

- [33] B. Window, Issues in magnetron sputtering of hard coatings, *Surf. Coatings Technol.* 81 (1996) 92–98.
- [34] H. Lüth, *Solid Surfaces, Interfaces and Thin Films*, 5th ed., Springer Berlin, Heidelberg, 2010.
- [35] P.B. Barna, M. Adamik, Fundamental structure forming phenomena of polycrystalline films and the structure zone models, *Thin Solid Films.* 317 (1998) 27–33.
- [36] B.A. Movchan, A.V. Demchishin, Study of the structure and properties of thick vacuum condensates of nickel titanium tungsten aluminium-oxide and zirconium dioxide, *Phys. Met. Met.* 28 (1969) 653–660.
- [37] J. Thornton, Influence of apparatus geometry and deposition conditions on the structure and topography of thick sputtered coatings, *J. Vac. Sci. Technol.* 11 (1974) 666–670.
- [38] R. Messier, A.P. Giri, R.A. Roy, Revised structure zone model for thin film physical structure, *J. Vac. Sci. Technol. A Vacuum, Surfaces, Film.* 2 (1984) 500–503.
- [39] A. Anders, A structure zone diagram including plasma-based deposition and ion etching, *Thin Solid Films.* 518 (2010) 4087–4090.
- [40] Y. Deng, W. Chen, B. Li, C. Wang, T. Kuang, Y. Li, Physical vapor deposition technology for coated cutting tools: A review, *Ceram. Int.* 46 (2020) 18373–18390.
- [41] S. Vepřek, The search for novel, superhard materials, *J. Vac. Sci. Technol. A.* 17 (1999) 2401–2420.
- [42] S. Veprek, M.G.J. Veprek-Heijman, P. Karvankova, J. Prochazka, Different approaches to superhard coatings and nanocomposites, *Thin Solid Films.* 476 (2005) 1–29.
- [43] J. Patscheider, Nanocomposite Hard Coatings for Wear Protection, *MRS Bull.* 28 (2003) 180–183.
- [44] F. Pei, H.J. Liu, L. Chen, Y.X. Xu, Y. Du, Improved properties of TiAlN coating by

- combined Si-addition and multilayer architecture, *J. Alloys Compd.* 790 (2019) 909–916.
- [45] D. Rafaja, A. Poklad, V. Klemm, G. Schreiber, D. Heger, M. Šíma, M. Dopita, Some consequences of the partial crystallographic coherence between nanocrystalline domains in Ti–Al–N and Ti–Al–Si–N coatings, *Thin Solid Films.* 514 (2006) 240–249.
- [46] L. Gao, J. Gstöttner, R. Emling, M. Balden, C. Linsmeier, A. Wiltner, W. Hansch, D. Schmitt-Landsiedel, Thermal stability of titanium nitride diffusion barrier films for advanced silver interconnects, *Microelectron. Eng.* 76 (2004) 76–81.
- [47] S. Massl, W. Thomma, J. Keckes, R. Pippan, Investigation of fracture properties of magnetron-sputtered TiN films by means of a FIB-based cantilever bending technique, *Acta Mater.* 57 (2009) 1768–1776.
- [48] J.M. Chappé, A.C. Fernandes, L. Cunha, C. Moura, F. Vaz, N. Martin, D. Munteanu, B. Borcea, TiN-based decorative coatings: Colour change by addition of C and O, *J. Optoelectron. Adv. Mater.* 10 (2008) 900–903.
- [49] W. Schintlmeister, O. Pacher, Preparation and properties of hard-material layers for metal machining and jewelry, *J. Vac. Sci. Technol.* 12 (1975) 743–748.
- [50] J. Wagner, C. Mitterer, M. Penoy, C. Michotte, W. Wallgram, M. Kathrein, The effect of deposition temperature on microstructure and properties of thermal CVD TiN coatings, *Int. J. Refract. Met. Hard Mater.* 26 (2008) 120–126.
- [51] H.E. Rebenne, D.G. Bhat, Review of CVD TiN coatings for wear-resistant applications: deposition processes, properties and performance, *Surf. Coat. Technol.* 63 (1994) 1–13.
- [52] A. Matthews, Titanium nitride PVD coating technology, *Surf. Eng.* 1 (1985) 93–104.
- [53] Y.H. Cheng, B.K. Tay, Development of texture in TiN films deposited by filtered cathodic vacuum arc, *J. Cryst. Growth.* 252 (2003) 257–264.
- [54] P.H. Mayrhofer, M. Geier, C. Löcker, L. Chen, Influence of deposition conditions on texture development and mechanical properties of TiN coatings, *Int. J. Mater. Res.*



- 100 (2009) 1052–1058.
- [55] H.Q. Lou, N. Axén, R.E. Somekh, I.M. Hutchings, Effect of deposition conditions on the characteristics of reactively sputtered titanium nitride films, *Surf. Coat. Technol.* 90 (1997) 123–127.
- [56] I. Petrov, L. Hultman, J.-E. Sundgren, J.E. Greene, Polycrystalline TiN films deposited by reactive bias magnetron sputtering: Effects of ion bombardment on resputtering rates, film composition, and microstructure, *J. Vac. Sci. Technol. A Vacuum, Surfaces, Film.* 10 (1992) 265–272.
- [57] J. Ishii, Y. Haruyama, S. Kawamura, N. Horikawa, Y. Iwai, Tribological performance evaluation of (1 1 1) preferred oriented TiN duplex coating, *Wear.* 267 (2009) 2173–2178.
- [58] A. Flink, T. Larsson, J. Sjöln, L. Karlsson, L. Hultman, Influence of Si on the microstructure of arc evaporated (Ti,Si)N thin films; evidence for cubic solid solutions and their thermal stability, *Surf. Coatings Technol.* 200 (2005) 1535–1542.
- [59] M. Sperr, Z.L. Zhang, Y.P. Ivanov, P.H. Mayrhofer, M. Bartosik, Correlating elemental distribution with mechanical properties of TiN/SiN<sub>x</sub> nanocomposite coatings, *Scr. Mater.* 170 (2019) 20–23.
- [60] D. Pilloud, J.F. Pierson, M.C. Marco de Lucas, A. Cavaleiro, Study of the structural changes induced by air oxidation in Ti-Si-N hard coatings, *Surf. Coatings Technol.* 202 (2008) 2413–2417.
- [61] A. Flink, M. Beckers, J. Sjöln, T. Larsson, S. Braun, L. Karlsson, L. Hultman, The location and effects of Si in (Ti<sub>1-x</sub>Si<sub>x</sub>)N<sub>y</sub> thin films, *J. Mater. Res.* 24 (2009) 2483–2498.
- [62] G. Abadias, V.V. Uglov, I.A. Saladukhin, S.V. Zlotski, G. Tolmachova, S.N. Dub, A. Janse van Vuuren, Growth, structural and mechanical properties of magnetron-sputtered ZrN/SiN<sub>x</sub> nanolaminated coatings, *Surf. Coat. Technol.* 308 (2016) 158–167.
- [63] C.L. Chang, C.T. Lin, P.C. Tsai, W.Y. Ho, W.J. Liu, D.Y. Wang, Mechanical and

- corrosion properties of (Ti,Si)N coating synthesized by cathodic arc plasma evaporation, *Surf. Coatings Technol.* 202 (2008) 5516–5520.
- [64] L. Chen, Y. Du, S.Q. Wang, A.J. Wang, H.H. Xu, Mechanical properties and microstructural evolution of TiN coatings alloyed with Al and Si, *Mater. Sci. Eng. A.* 502 (2009) 139–143.
- [65] F. Vaz, L. Rebouta, P. Goudeau, J. Pacaud, H. Garem, J.P. Rivière, A. Cavaleiro, E. Alves, Characterisation of  $Ti_{1-x}Si_xN_y$  nanocomposite films, *Surf. Coatings Technol.* 133–134 (2000) 307–313.
- [66] C. Kainz, N. Schalk, C. Saringer, C. Czettel, In-situ investigation of the oxidation behavior of powdered TiN, Ti(C,N) and TiC coatings grown by chemical vapor deposition, *Surf. Coat. Technol.* 406 (2021) 126633.
- [67] M. Diserens, J. Patscheider, F. Lévy, Mechanical properties and oxidation resistance of nanocomposite TiN-SiN<sub>x</sub> physical-vapor-deposited thin films, *Surf. Coatings Technol.* 120–121 (1999) 158–165.
- [68] Y. Hu, H.L. Tsai, C.L. Huang, Effect of brookite phase on the anatase-rutile transition in titania nanoparticles, *J. Eur. Ceram. Soc.* 23 (2003) 691–696.
- [69] A. Kimura, H. Hasegawa, K. Yamada, T. Suzuki, Effects of Al content on hardness, lattice parameter and microstructure of  $Ti_{1-x}Al_xN$  films, *Surf. Coat. Technol.* 120–121 (1999) 438–441.
- [70] Y.C. Chim, X.Z. Ding, X.T. Zeng, S. Zhang, Oxidation resistance of TiN, CrN, TiAlN and CrAlN coatings deposited by lateral rotating cathode arc, *Thin Solid Films.* 517 (2009) 4845–4849.
- [71] P.H. Mayrhofer, C. Mitterer, L. Hultman, H. Clemens, Microstructural design of hard coatings, *Prog. Mater. Sci.* 51 (2006) 1032–1114.
- [72] C. Wüstefeld, D. Rafaja, V. Klemm, C. Michotte, M. Kathrein, Effect of the aluminium content and the bias voltage on the microstructure formation in  $Ti_{1-x}Al_xN$  protective coatings grown by cathodic arc evaporation, *Surf. Coat.*

- Technol. 205 (2010) 1345–1349.
- [73] A. Hörling, L. Hultman, M. Odén, J. Sjölen, L. Karlsson, Mechanical properties and machining performance of  $Ti_{1-x}Al_xN$ -coated cutting tools, *Surf. Coat. Technol.* 191 (2005) 384–392.
- [74] I.A. Abrikosov, A. Knutsson, B. Alling, F. Tasnádi, H. Lind, L. Hultman, M. Odén, Phase Stability and Elasticity of  $TiAlN$ , *Materials (Basel)*. 4 (2011) 1599–1618.
- [75] L. Chen, J. Paulitsch, Y. Du, P.H. Mayrhofer, Thermal stability and oxidation resistance of Ti-Al-N coatings, *Surf. Coat. Technol.* 206 (2012) 2954–2960.
- [76] P.H. Mayrhofer, A. Hörling, L. Karlsson, J. Sjölen, T. Larsson, C. Mitterer, L. Hultman, Self-organized nanostructures in the Ti-Al-N system, *Appl. Phys. Lett.* 83 (2003) 2049–2051.
- [77] S. Carvalho, L. Rebouta, A. Cavaleiro, L.A. Rocha, J. Gomes, E. Alves, Microstructure and mechanical properties of nanocomposite (Ti,Si,Al)N coatings, *Thin Solid Films*. 398–399 (2001) 391–396.
- [78] L. Chen, B. Yang, Y. Xu, F. Pei, L. Zhou, Y. Du, Improved thermal stability and oxidation resistance of Al-Ti-N coating by Si addition, *Thin Solid Films*. 556 (2014) 369–375.
- [79] A. Flink, J.M. Andersson, B. Alling, R. Daniel, J. Sjölen, L. Karlsson, L. Hultman, Structure and thermal stability of arc evaporated  $(Ti_{0.33}Al_{0.67})_{1-x}Si_xN$  thin films, *Thin Solid Films*. 517 (2008) 714–721.
- [80] D. Yu, C. Wang, X. Cheng, F. Zhang, Microstructure and properties of  $TiAlSiN$  coatings prepared by hybrid PVD technology, *Thin Solid Films*. 517 (2009) 4950–4955.
- [81] M. Pfeiler, J. Zechner, M. Penoy, C. Michotte, C. Mitterer, M. Kathrein, Improved oxidation resistance of  $TiAlN$  coatings by doping with Si or B, *Surf. Coat. Technol.* 203 (2009) 3104–3110.
- [82] L. Zhu, M. Hu, W. Ni, Y. Liu, High temperature oxidation behavior of  $Ti_{0.5}Al_{0.5}N$

- coating and  $\text{Ti}_{0.5}\text{Al}_{0.4}\text{Si}_{0.1}\text{N}$  coating, *Vaccum*. 86 (2012) 1795–1799.
- [83] I. Krajinovic, W. Daves, M. Tkadletz, T. Tepperneegg, T. Klünsner, N. Schalk, C. Mitterer, C. Tritremmel, W. Ecker, C. Czettl, Finite element study of the influence of hard coatings on hard metal tool loading during milling, *Surf. Coat. Technol.* 304 (2016) 134–141.
- [84] C. Saringer, C. Kickingner, F. Munnik, C. Mitterer, N. Schalk, M. Tkadletz, Thermal expansion of magnetron sputtered  $\text{TiC}_x\text{N}_{1-x}$  coatings studied by high-temperature X-ray diffraction, *Thin Solid Films*. 688 (2019) 137307.
- [85] C. Kainz, C. Saringer, M. Burtscher, M. Tkadletz, A. Stark, N. Schell, M. Pohler, C. Czettl, D. Kiener, N. Schalk, Oxidation resistance of cathodic arc evaporated  $\text{Cr}_{0.74}\text{Ta}_{0.26}\text{N}$  coatings, *Scr. Mater.* 211 (2022) 114492.
- [86] C. Saringer, M. Tkadletz, A. Stark, N. Schell, C. Czettl, N. Schalk, In-situ investigation of the oxidation behavior of metastable CVD- $\text{Ti}_{1-x}\text{Al}_x\text{N}$  using a novel combination of synchrotron radiation XRD and DSC, *Surf. Coatings Technol.* 374 (2019) 617–624.
- [87] H.M. Rietveld, A profile refinement method for nuclear and magnetic structures, *J. Appl. Crystallogr.* 2 (1969) 65–71.
- [88] R.E. Dinnebier, A. Leineweber, J.S.O. Evans, *Rietveld Refinement: Practical Powder Diffraction Pattern Analysis using TOPAS*, De Gruyter, Berlin, Boston, 2019.
- [89] J.F. Moulder, W.F. Stickle, P.E. Sobol, K.D. Bomben, *Handbook of X-ray Photoelectron Spectroscopy: A Reference Book of Standard Spectra for Identification and Interpretation of XPS Data*, Perkin-Elmer Corporation, Eden Prairie, Minnesota, USA, 1992.
- [90] A. Einstein, On a heuristic point of view concerning the production and transformation of light, *Ann. Phys.* 17 (1905) 132–148.
- [91] K. Siegbahn, C. Nordling, A. Fahlman, R. Nordberg, K. Hamrin, J. Hedman, G. Johansson, T. Bergmark, S.-E. Karlsson, I. Lindgren, B. Lindberg, *ESCA; Atomic*,

- Molecular and Solid State Structure Studied by Means of Electron Spectroscopy, Almqvist & Wiksells, Uppsala, Sweden, 1967.
- [92] C.J. Powell, A. Jablonski, Surface sensitivity of X-ray photoelectron spectroscopy, *Nucl. Instruments Methods Phys. Res. Sect. A.* 601 (2009) 54–65.
- [93] T.L. Alford, L.C. Feldman, J.W. Mayer, Fundamentals of nanoscale film analysis, Springer Science & Business Media, Inc., New York, USA, 2007.
- [94] D. Schild, X-ray Photoelectron Spectroscopy, in: A. Léon (Ed.), *Hydrog. Technol.*, Springer Verlag, Berlin, Heidelberg, 2008.
- [95] D.S. Jensen, S.S. Kanyal, N. Madaan, M.A. Vail, A.E. Dadson, M.H. Engelhard, M.R. Linford, Silicon (100)/SiO<sub>2</sub> by XPS, *Surf. Sci. Spectra.* 20 (2013) 36–42.
- [96] R. Gilmore, M.A. Baker, P.N. Gibson, W. Gissler, Comparative investigation of multilayer TiB<sub>2</sub>/C and co-sputtered TiB<sub>2</sub>-C coatings for low-friction applications., *Surf. Coat. Technol.* 116–119 (1999) 1127–1132.
- [97] M.C. Simmonds, A. Savan, H. Van Swygenhoven, E. Pflüger, S. Mikhailov, Structural, morphological, chemical and tribological investigations of sputter deposited MoS<sub>x</sub>/metal multilayer coatings, *Surf. Coat. Technol.* 108–109 (1998) 340–344.
- [98] P. Panjan, B. Navinšek, A. Cvelbar, A. Zalar, I. Milošev, Oxidation of TiN, ZrN, TiZrN, CrN, TiCrN and TiN/CrN multilayer hard coatings reactively sputtered at low temperature, *Thin Solid Films.* 281–282 (1996) 298–301.
- [99] D.R. Baer, K. Artyushkova, C.R. Brundle, J.E. Castle, M.H. Engelhard, K.J. Gaskell, J.T. Grant, R.T. Haasch, M.R. Linford, C.J. Powell, A.G. Shard, P.M.A. Sherwood, V.S. Smentkowski, Practical guides for x-ray photoelectron spectroscopy: First steps in planning, conducting, and reporting XPS measurements., *J. Vac. Sci. Technol. A.* 37 (2019) 031401.
- [100] G. Greczynski, L. Hultman, Towards reliable X-ray photoelectron spectroscopy: Sputter-damage effects in transition metal borides, carbides, nitrides, and oxides,

Appl. Surf. Sci. 542 (2021) 148599.

## 7 Publications

### 7.1 List of included publications

- I. **Microstructure and mechanical properties of arc evaporated Ti(Al,Si)N coatings**  
Yvonne Moritz, Christina Kainz, Michael Tkadletz, Christoph Czettl, Markus Pohler, Nina Schalk  
Surface and Coatings Technology 421 (2021) 127461.
  
- II. **Oxidation behavior of arc evaporated TiSiN coatings investigated by *in-situ* synchrotron X-ray diffraction and HR-STEM**  
Yvonne Moritz, Christian Saringer, Michael Tkadletz, Andreas Stark, Norbert Schell, Ilse Letofsky-Papst, Christoph Czettl, Markus Pohler, Nina Schalk  
Surface and Coatings Technology 404 (2020) 126632.
  
- III. **Oxidation mechanism of sputter deposited model SiN<sub>x</sub>/TiN/SiN<sub>x</sub> coatings**  
Yvonne Moritz, Christina Kainz, Paul Peritsch, Christian Mitterer, Nina Schalk  
Under review in Surface and Coatings Technology (2023).
  
- IV. ***In-situ* X-ray diffraction study of the oxidation behavior of arc evaporated TiAlSiN coatings with low Al contents**  
Yvonne Moritz, Christian Saringer, Michael Tkadletz, Alexander Fian, Christoph Czettl, Markus Pohler, Nina Schalk  
Submitted to Surface and Coatings Technology (2023).

# Publication I

## **Microstructure and mechanical properties of arc evaporated Ti(Al,Si)N coatings**

Yvonne Moritz, Christina Kainz, Michael Tkadletz, Christoph Czettl, Markus Pohler,  
Nina Schalk

**Surface & Coatings Technology 421 (2021) 127461**



## Microstructure and mechanical properties of arc evaporated Ti(Al,Si)N coatings

Yvonne Moritz<sup>a</sup>, Christina Kainz<sup>a</sup>, Michael Tkadletz<sup>b</sup>, Christoph Czettel<sup>c</sup>, Markus Pohler<sup>c</sup>, Nina Schalk<sup>a</sup>

<sup>a</sup> Christian Doppler Laboratory for Advanced Coated Cutting Tools at the Department of Materials Science, Montanuniversität Leoben, Franz–Josef–Strasse 18, 8700 Leoben, Austria

<sup>b</sup> Department of Materials Science, Montanuniversität Leoben, Franz–Josef–Strasse 18, 8700 Leoben, Austria

<sup>c</sup> Ceratizit Austria GmbH, Metallwerk-Plansee-Strasse 71, 6600 Reutte, Austria

### Abstract

Ti(Al)SiN protective hard coatings are promising candidates for the metal cutting industry, due to their favorable properties such as a high hardness and good oxidation resistance. Within the scope of this work, the microstructure of cathodic arc evaporated TiN, Ti<sub>84</sub>Si<sub>16</sub>N, Ti<sub>81</sub>Al<sub>3</sub>Si<sub>16</sub>N and Ti<sub>70</sub>Al<sub>14</sub>Si<sub>16</sub>N was correlated with their mechanical properties. X-ray diffraction (XRD) as well as scanning electron microscopy investigations of the cross-sections revealed a pronounced grain refinement for Ti(Al)SiN compared to TiN. The texture of the coatings was analyzed by XRD pole-figures, showing a change in the preferred orientation in growth direction from (111) for TiN to (200) for Ti(Al)SiN. Hardness values were found to strongly increase from 29 GPa to 40 GPa upon Si addition, but remained constant for further alloying with Al. Micromechanical bending tests allowed to gain a detailed insight into the fracture properties of the investigated coatings and revealed an enhanced fracture stress and fracture toughness ( $K_{IC}$ ) for Ti(Al)SiN

compared to TiN. Hereby, the  $K_{IC}$  value of  $2.4 \pm 0.3 \text{ MPa}\cdot\text{m}^{1/2}$  for TiN could be increased to a maximum of  $3.3 \pm 0.2 \text{ MPa}\cdot\text{m}^{1/2}$  for  $\text{Ti}_{70}\text{Al}_{14}\text{Si}_{16}\text{N}$ . The present findings provide a systematic overview of the microstructure and mechanical properties of arc evaporated Ti(Al,Si)N coatings, thus allowing to select the most suitable coatings for different applications in the cutting industry.

**Keywords:** Ti(Al)SiN, hard coatings, cathodic arc evaporation, fracture mechanics

## 1. Introduction

The ever-increasing industrial demands of cutting tools regarding lifetime and performance have led to intensive research on protective hard coatings with favorable properties such as high hardness and high thermal stability. Among the nitride-based hard coatings, TiN has met the industrial requirements for several decades, however, drawbacks such as a moderate hardness slightly above 20 GPa [1–3] and a low oxidation resistance [4–6] have called for the search of new coating materials with improved properties. One of the most common strategies to obtain these desired properties is the addition of further elements to TiN. In 1986, Münz reported that alloying TiN with Al considerably enhances the cutting performance and increases the oxidation resistance by  $\sim 250 \text{ }^\circ\text{C}$  [7]. Furthermore, TiAlN is known to exhibit significantly higher hardness values of  $\sim 24\text{--}36 \text{ GPa}$  [8–10], depending on the Al content and deposition parameters. In addition, TiAlN has the benefit of exhibiting an age hardening effect when exposed to temperatures between 600 and 1000  $^\circ\text{C}$ , due to the occurring spinodal decomposition into cubic TiN rich and AlN rich domains [11,12]. Besides alloying with Al, also the effects of Si addition to Ti(Al)N have been investigated by several researchers. Si has been described to be either present as a substitution of Ti within the Ti(Al)N solid solution or within an amorphous  $\text{SiN}_x$  (a-SiN<sub>x</sub>) tissue phase surrounding the crystalline Ti(Al)N grains, thus forming a nanocomposite structure [8,13–17]. Exceptionally high hardness values above

40 GPa have been reported for Ti(Al)SiN coatings [16,18,19], which can be attributed to the induced grain refinement upon Si addition as well as to the amorphous tissue phase inhibiting dislocation movement and grain-boundary sliding [20].

In addition to hardness and Young's modulus, also the fracture toughness is a crucial mechanical property influencing the performance of protective hard coatings in machining applications. However, the fracture behavior of Ti(Al)SiN coatings has hardly been investigated in literature. Bartosik et al. examined the fracture toughness of sputtered TiAlN coatings compared to TiN by performing micromechanical bending tests on as-deposited samples and after annealing at temperatures up to 1000 °C [21]. It became apparent that the investigated Ti<sub>40</sub>Al<sub>60</sub>N coating did not only exhibit a higher fracture toughness ( $K_{IC}$ ) of 2.7 MPa×m<sup>1/2</sup> compared to ~2.0 MPa×m<sup>1/2</sup> for TiN at room temperature, but also showed an increased  $K_{IC}$  value by about 11 % upon annealing to 900 °C. This increase in fracture toughness was found to be strongly connected to the spinodal decomposition and the occurrence of fractions of wurtzitic-AlN (w-AlN) [21]. In a follow-up work of Bartosik et al., the fracture toughness of TiSiN coatings deposited by reactive magnetron sputtering with Si contents varying between 0 and 14 at.% within the coatings was illuminated. A maximum fracture toughness of 3.0 MPa×m<sup>1/2</sup> was observed for 8.5 at.% of Si, while pure TiN only yielded a value of 1.9 MPa×m<sup>1/2</sup>. The significantly higher  $K_{IC}$  value of TiSiN was attributed to grain refinement, formation of a dense microstructure and increased cohesive strength of the grain boundaries upon Si addition [22].

While Bartosik et al. have reported on the fracture toughness of magnetron-sputtered TiSiN coatings with varying Si content [22], to the best of our knowledge no data have been published on the fracture stress and toughness of arc evaporated TiSiN coatings. Furthermore, literature is lacking a systematic investigation of the change in mechanical properties upon addition of Al to TiSiN, especially in regards to the fracture behavior of these coatings. Several authors have concentrated their studies on the

influence of Si addition to TiAlN [8,23–26], however publications dealing exclusively with the effect of Al addition to TiSiN are rare and usually focus on TiAlSiN coatings with higher Al contents >30 % of the metallic fraction [27,28]. Thus, in this work the microstructure and mechanical properties of TiN, TiSiN and TiAlSiN with low Al contents of 3 and 14 % (referring to the metallic fraction) were investigated. X-ray diffraction (XRD) of powdered and solid coatings as well as scanning electron microscopy (SEM) of cross-sections gave insight into the microstructure. Additionally, pole-figures recorded by XRD allowed to analyze the texture of the respective coatings. Determination of the hardness and Young's modulus of the Ti(Al,Si)N coatings in combination with micromechanical bending tests provided information about crucial mechanical properties for cutting applications.

## 2. Experimental

The four Ti(Al,Si)N coatings investigated in this study were deposited by cathodic arc evaporation (CAE) using an industrial scale Oerlikon Balzers Innova deposition plant. Powder metallurgically prepared Ti, Ti<sub>80</sub>Si<sub>20</sub>, Ti<sub>76</sub>Al<sub>4</sub>Si<sub>20</sub> and Ti<sub>64</sub>Al<sub>16</sub>Si<sub>20</sub> targets were used for the synthesis of TiN, TiSiN and TiAlSiN coatings with different Al content, respectively. The coatings were deposited on cemented carbide (CC) substrates (92 wt.% WC, 6 wt.% Co and 2 wt.% mixed carbides) in SNUN geometry according to ISO 1832 and on mild steel foils. Prior to the deposition process, substrates were ion-etched in an Ar plasma. All coatings were deposited in pure N<sub>2</sub> atmosphere at a pressure of  $3.5 \times 10^{-2}$  mbar applying a bias voltage of -40 V and 2-fold substrate rotation. The substrate temperature was kept constant at 430 °C for TiN and 480 °C for the Si containing coatings. The cathodes were operated using a DC arc current of 180 A. After the deposition process, the coated steel foils were dissolved in nitric acid in order to obtain a free-standing coating powder for XRD investigations.

The elemental composition of the Ti(Al,Si)N coatings was determined by glow discharge optical emission spectroscopy (GDOES) using a Horiba GD-Profilier 2

spectrometer. To obtain images of the cross-sections of the samples, the coatings were prepared with a Hitachi IM4000+ ion milling system using Ar<sup>+</sup> ions and investigated utilizing a scanning electron microscope (SEM) ZEISS GeminiSEM 450. The microstructure of the solid coatings on CC was investigated applying a Bruker D8 Advance X-ray diffractometer in grazing incidence geometry. Cu-K $\alpha$  radiation ( $\lambda = 1.5406 \text{ \AA}$ ) was collimated by a Göbel mirror and directed at the sample with an incidence angle of 2°. The 2 $\theta$ -scan was recorded with an energy-dispersive Sol-X detector. The measurement time was set to 1.0 s per step and the step size was 0.02°. To gain additional information about the texture of the coatings, pole figures (PFs) were measured on a Bruker D8 Advance DaVinci diffractometer using Cu-K $\alpha$  radiation ( $\lambda = 1.5406 \text{ \AA}$ ) and a position sensitive LynxEye Xe-T detector. The samples were tilted from 0° to 84° and rotated around the surface normal for each tilt angle using a half-circle Eulerian cradle. PFs of the (111), (200) and (220) reflections were recorded for each coating. The MTEX toolbox [29] was utilized for data processing and the calculation of the PFs and inverse pole figures (IPFs). Additionally, analysis of the powdered coatings was conducted on the Bruker D8 Advance DaVinci diffractometer in Bragg-Brentano geometry using a step-size of 0.005° (measuring time 1.0 s per step), in order to generate a diffractogram suitable for a subsequent Pawley-refinement with the Software Topas 6. An XRD pattern of a standard LaB<sub>6</sub> powder sample (NIST 660c) [30] was recorded as a reference and refined to account for the influence of the instrumental parameters.

In order to evaluate the hardness and Young's modulus of the four Ti(Al,Si)N coatings, the surface of the samples was mirror-polished and measured by nanoindentation, using an Ultra Micro Indentation System (UMIS) from Fischer-Cripps Laboratories operating with a diamond Berkovich tip. To eliminate substrate effects during the measurement, plateau tests with 35 indents in a load range of 30 to 12.5 mN with penetration depths below 10 % of the respective coating thickness were carried out. The Oliver and Pharr method was utilized to evaluate the obtained data [31]. To gain

further insight into the mechanical properties of the investigated Ti(Al,Si)N coatings, micromechanical bending tests were conducted. A focused ion beam (FIB) workstation (FEI DualBeam Versa 3D) was used to prepare freestanding micro-cantilevers with dimensions of  $\sim 9 \mu\text{m}$  length and a  $\sim 3 \times 3 \mu\text{m}^2$  cross-section. Particular attention was paid to choosing areas without any microparticles - that would strongly impair the fracture properties - for the preparation of the micro-cantilevers. Unnotched cantilevers were used for the determination of the fracture stress, while cantilevers with a sharp notch served for evaluation of the fracture toughness. The planned position for subsequent indentation of the cantilevers was marked with the FIB by a circle. In order to correctly position the cantilevers, imaging was performed by scanning probe microscopy using a Hysitron TriboIndenter TI950. The cantilevers were then loaded until fracture with a rate of 5 nm/s using the TI950 equipped with a conospherical tip. At least three notched and unnotched cantilevers were fractured for each of the four Ti(Al,Si)N coatings, allowing to obtain statistically valid results. Evaluation of the obtained data was proceeded according to Matoy et al. [32], whereby the cantilever geometry and the determined maximum load at fracture were taken into account. After completing the micromechanical tests, the post-mortem cross-sections of the cantilevers as well as the depth of the notch were analyzed by SEM (FEI DualBeam Versa 3D).

### 3. Results and Discussion

#### 3.1 Microstructure

The elemental analysis of the four arc evaporated coatings investigated in this study revealed that all of them are stoichiometric with a nitrogen content of  $\sim 50$  at.%. The elemental composition was determined to be TiN,  $\text{Ti}_{84}\text{Si}_{16}\text{N}$ ,  $\text{Ti}_{81}\text{Al}_3\text{Si}_{16}\text{N}$  and  $\text{Ti}_{70}\text{Al}_{14}\text{Si}_{16}\text{N}$  via GDOES. The Si content remained constant for all Ti(Al)SiN coatings, allowing a systematic investigation of the influence of Al addition to TiSiN. Furthermore, it is evident that the Al and Si contents within the coatings are slightly lower compared to the composition of the respective targets ( $\text{Ti}_{80}\text{Si}_{20}$ ,  $\text{Ti}_{76}\text{Al}_4\text{Si}_{20}$  and  $\text{Ti}_{64}\text{Al}_{16}\text{Si}_{20}$ ), which was

already observed by other researchers that deposited Ti(Al)SiN coatings using CAE [8,16]. This finding can be attributed to the more pronounced re-sputtering and gas phase scattering of the significantly lighter Al and Si elements compared to Ti [33].

To obtain a first overview of the microstructure of the coatings, SEM micrographs of cross-sections were recorded, which are shown in Fig. 1. While TiN (Fig. 1(a)) exhibits large and columnar grains, a pronounced grain refinement and the formation of a feather-like structure occurs when adding Si (Fig. 1(b)). The results are in accordance with literature, as a decreasing grain size and the occurrence of a feather-like structure was already reported by other researchers for TiSiN coatings [16,34]. When taking a closer look at Fig. 1(c) and (d) it becomes evident that a comparable microstructure is obtained for  $\text{Ti}_{81}\text{Al}_3\text{Si}_{16}\text{N}$  and  $\text{Ti}_{70}\text{Al}_{14}\text{Si}_{16}\text{N}$ . Thus, the influence of the Al addition on the microstructure seems to be minor. Detailed investigations regarding the microstructure of the TiSiN sample at higher magnification were conducted in a previous study using high-resolution scanning transmission electron microscopy [35]. The recorded micrographs showed the presence of nanocrystalline (nc) and amorphous regions, verifying a nanocomposite structure of the TiSiN coating. It can be assumed that also for the addition of small amounts of Al to TiSiN the nanocomposite structure is retained, which was also reported by several authors in literature [8,26,36].

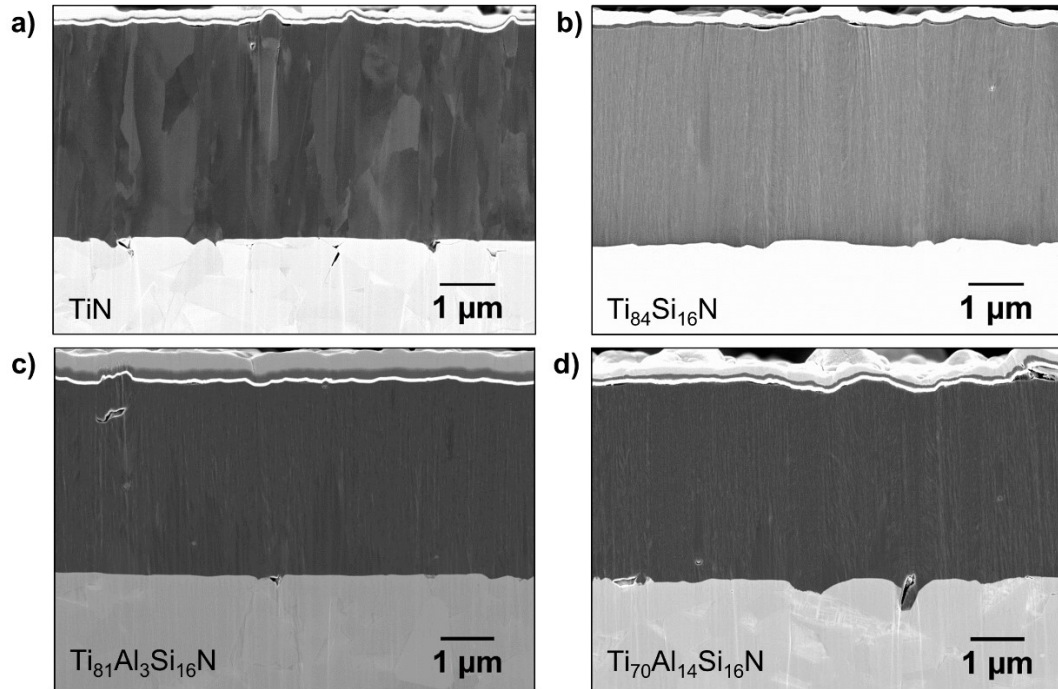


Fig. 1: SEM micrographs showing the cross-sections of TiN (a),  $Ti_{84}Si_{16}N$  (b),  $Ti_{81}Al_3Si_{16}N$  (c) and  $Ti_{70}Al_{14}Si_{16}N$  (d) coatings on CC substrates.

To gain further insight into the microstructure, X-ray diffractograms were recorded of the solid coatings on CC, which are displayed in Fig. 2(a). Standard peak positions of face-centered cubic (fcc) TiN (ICDD 00-038-1420), fcc-AlN (ICDD 00-025-1495) and WC (ICDD 00-051-0939) [37], stemming from the CC substrate, are indicated by dashed lines. All coatings exhibit an fcc-structure. In accordance with literature, no crystalline  $SiN_x$  or  $TiSi_2$  phases are evident for Ti(Al)SiN [1,8,16,17]. Furthermore, no w-AlN phase is present. Pronounced peak broadening can be observed when Si is added to TiN, while Al addition to TiSiN results in no further change of the peak width, which is also evidenced by the full width at half maximum (FWHM) shown in Fig. 2(b). The FWHM were determined from the (200) peak by a Pseudo-Voigt fit. It can be observed that the FWHM for TiN is much lower compared to the Ti(Al)SiN coatings, while for the latter the FWHM only differs slightly. An increasing FWHM is attributed to a smaller size of the coherently diffracting domains and/or increased microstrain, which can be



assumed to correlate with the grain size [38,39]. Thus, the evolution of the FWHM is in accordance with the SEM cross-sections shown in Fig. 1. The X-ray diffractograms of the solid coatings reveal a small peak shift to higher diffraction angles for the  $\text{Ti}_{70}\text{Al}_{14}\text{Si}_{16}\text{N}$  sample that might be attributed to a decreasing lattice parameter. However, as the peak position of the solid coatings is influenced by both, the lattice parameter and the residual stress, powdered coatings – which are free of macroscopic stress – were additionally studied by XRD to determine the respective stress free lattice parameters. The diffractograms are displayed in Fig. 2(c). The refinement of the TiN powder X-ray diffractogram yielded a lattice parameter of  $4.24 \pm 0.01 \text{ \AA}$ , which decreased to  $4.22 \pm 0.01 \text{ \AA}$  upon incorporation of Si, indicating the formation of an  $\text{Ti}(\text{Si})\text{N}$  solid solution that was already observed by other authors [16,17,40]. Due to the fact that also amorphous regions became evident for the  $\text{TiSiN}$  coating in our previous study, Si can be assumed to be present in both, an  $\text{Ti}(\text{Si})\text{N}$  solid solution and an  $\text{a-SiN}_x$  phase. Addition of Al to  $\text{TiSiN}$  yielded a further decrease of the lattice parameter to  $4.21$  or  $4.19 \pm 0.01 \text{ \AA}$ , respectively, which has commonly been observed in literature for the formation of a fcc-TiAlN solid solution [7,41,42].

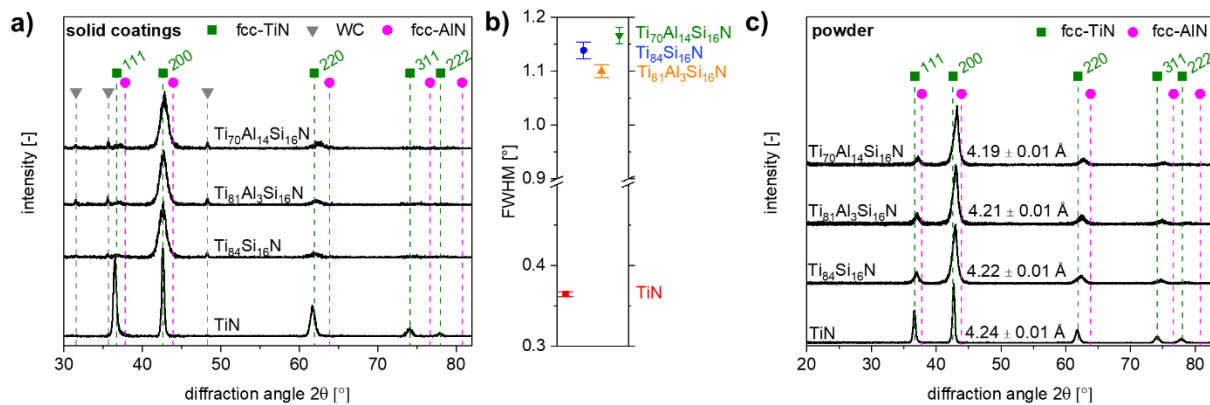


Fig. 2: X-ray diffractograms of solid  $\text{Ti}(\text{Al},\text{Si})\text{N}$  coatings on CC (a), the corresponding FWHM (b) and X-ray diffractograms of powdered  $\text{Ti}(\text{Al},\text{Si})\text{N}$  coatings, including the respective lattice parameters determined by Pawley-refinement (c).

In order to investigate the texture of the coatings, XRD PFs were recorded. Recalculation of the measured data using the MTEX-toolbox [29] allowed to obtain the PFs of the (111), (200) and (220) reflexes as well as the IPFs in growth direction, which are summarized in Fig. 3. It has to be noted that the intensities were normalized for each coating. All of the Ti(Al,Si)N coatings show a fibre texture, which can be deduced from the rotational symmetry of the respective intensities of the PFs. For the TiN coating depicted in Fig. 3(a), a preferred (111) orientation in growth direction was found, however the texture was not pronounced as also contributions from grains in the [001] direction are visible in the IPF. A strong change in texture was observed upon addition of Si to TiN, resulting in a pronounced (200) preferred orientation in growth direction as shown in the IPF in Fig. 3(b). Although several authors have reported a (mixed) (111) preferred orientation for TiN that changes to a (200) orientation for TiSiN coatings [19,43], the origin of this change in texture is usually not discussed. One possible explanation for the texture change upon Si addition could be based on the findings of Abadias et al. in a publication discussing nanolaminated ZrN/SiN<sub>x</sub> coatings [44]. There, the authors observed a change from a (111) preferred orientation for monolayered ZrN to a (200) orientation for nanoscale ZrN/SiN<sub>x</sub> multilayers. They attributed the different texture to the disruption of the columnar growth of ZrN by a-SiN<sub>x</sub>. The SiN<sub>x</sub> layers were proposed to act as seed layers for ZrN renucleation and thus result in the preferential nucleation of [001]-oriented crystallites, corresponding to the plane of lowest surface energy for Na-Cl type structures [44]. As already mentioned before, the TiSiN investigated in the present study exhibits a nanocomposite structure, consisting of nc-Ti(Si)N embedded in an a-SiN<sub>x</sub> tissue phase [35]. Therefore, an identical underlying mechanism - meaning that the a-SiN<sub>x</sub> favors renucleation of TiN - can be assumed for the texture change to a (200) preferred orientation with addition of Si to TiN. Addition of Al to TiSiN does not seem to further affect the texture, as shown by the PFs and IPF in Fig. 3(c) for Ti<sub>70</sub>Al<sub>14</sub>Si<sub>16</sub>N and thus also results in a pronounced (200) preferred orientation in growth direction. As expected, the

same texture was observed for the coating with lower Al content of  $\text{Ti}_{81}\text{Al}_3\text{Si}_{16}\text{N}$ , wherefore these PFs and IPF are not additionally depicted in Fig. 3.

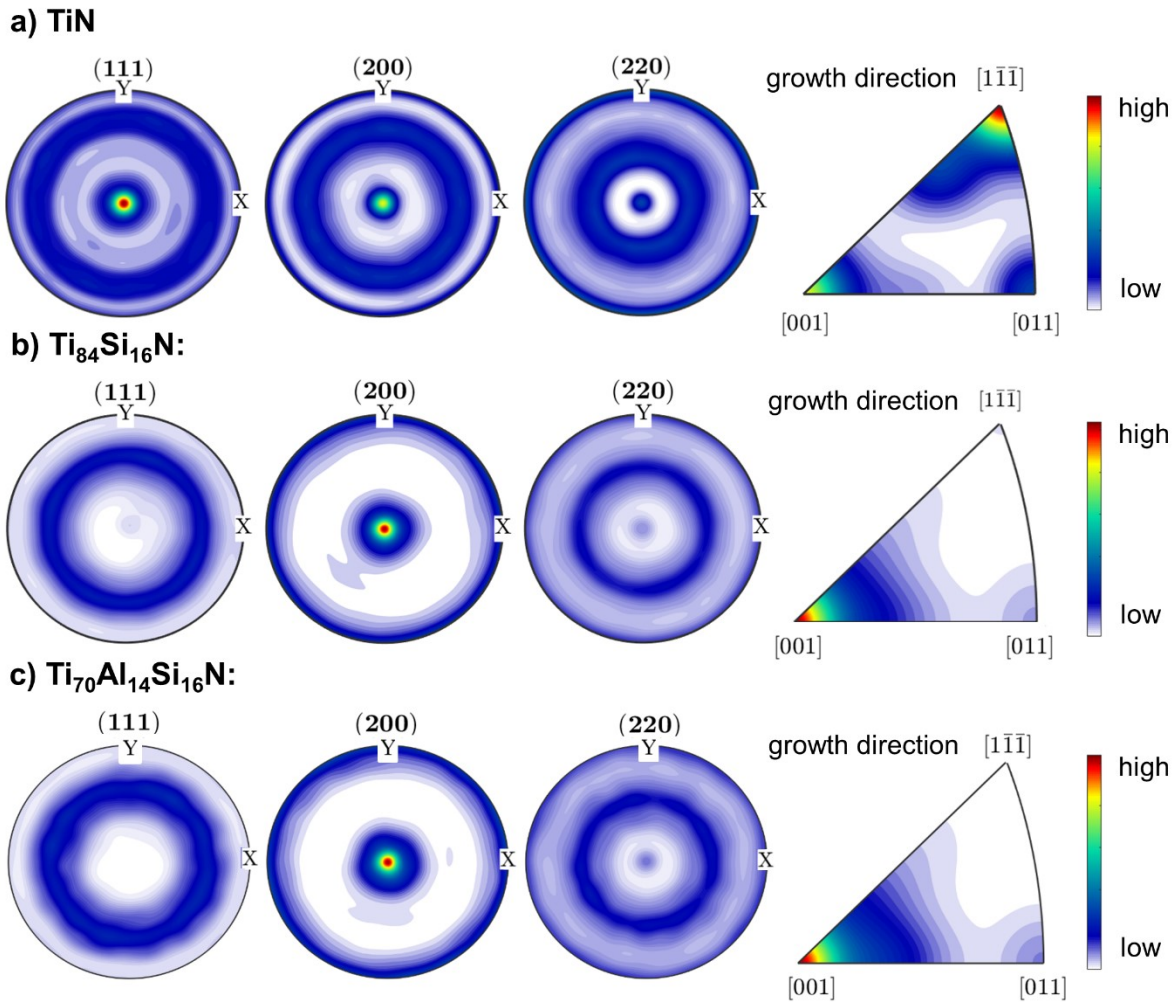


Fig. 3: XRD pole-figures of the (111), (200) and (220) reflexes and inverse pole-figures for TiN (a),  $\text{Ti}_{84}\text{Si}_{16}\text{N}$  (b), and  $\text{Ti}_{70}\text{Al}_{14}\text{Si}_{16}\text{N}$  (c) coatings.

### 3.2 Mechanical properties

To evaluate the mechanical properties of the coatings, the hardness and Young's modulus was determined using nanoindentation; the results are shown in Fig. 4. TiN exhibits a hardness value of  $29 \pm 2$  GPa, which is in the upper range of reported literature values (21-29 GPa) for cathodic arc evaporated TiN [1,2,5,16]. A strong increase in hardness to  $40 \pm 2$  GPa is observed upon Si addition, which can be attributed to the

pronounced grain refinement and the formation of a nanocomposite structure, where the  $\alpha$ -SiN<sub>x</sub> phase inhibits grain boundary sliding [20,45]. The exceptionally high hardness value for TiSiN is in accordance with literature, where, depending on the Si content and deposition parameters, values in the range of ~30-50 GPa have been reported [3,5,16,19,34,45]. Upon further addition of low amounts of Al to TiSiN the hardness values in the present study were found to remain constant at  $40 \pm 2$  GPa. Thus, it can be stated that addition of Si leads to a pronounced increase in hardness of more than 10 GPa compared to TiN, while alloying with low amounts of Al does not further affect the hardness. This can be attributed to the very similar, fine-grained and most likely nanocomposite microstructure for all Ti(Al)SiN coatings. In literature, again hardness values for TiAlSiN widely vary, depending on the respective Al or Si content. Zhu et al. investigated TiAlSiN coatings with rather high Al contents and reported a hardness value of 33 GPa for Ti<sub>55</sub>Al<sub>35</sub>Si<sub>10</sub>N that slightly increased to 35 GPa for an increasing Al content of Ti<sub>50</sub>Al<sub>40</sub>Si<sub>10</sub>N [27]. Yu et al. evaluated the influence of the Si content between 0 and 22 at.% on TiAlSiN coatings with ~10 at.% of Al and found the highest hardness of 35 GPa for Si contents between 4 and 10 at.% that decreased to 15 GPa for high Si contents of 22 at.% [24]. The decreasing hardness for higher Si contents was attributed to exceeding the optimum value of grain separation by the amorphous SiN<sub>x</sub> phase. A significantly higher hardness was found by Chen et al. that observed a value of 40 GPa for addition of 6 at.% Si and low Al contents of 3 at.% [46], which is comparable to the present study.

Besides the hardness, also the Young's modulus is dependent on the change in chemical composition. TiN exhibits the highest Young's modulus among the investigated coatings of  $578 \pm 31$  GPa. Upon addition of Si to TiN, a reduction of the Young's modulus to  $529 \pm 38$  GPa is observed. This tendency can be explained by the nanocomposite structure of the TiSiN: the grain boundaries are known to have a lower Young's modulus compared to the neighbouring crystals, thus leading to a decreasing Young's modulus with smaller grain size [47]. No significant change of the Young's modulus is observed

for alloying with Al for  $\text{Ti}_{81}\text{Al}_3\text{Si}_{16}\text{N}$  that shows a value of  $537 \pm 25$  GPa, increasing the Al content to  $\text{Ti}_{70}\text{Al}_{14}\text{Si}_{16}\text{N}$  leads to a slight decrease to  $494 \pm 23$  GPa. In literature, even lower Young's moduli in the range of 370-400 GPa are reported for arc evaporated TiAlSiN coatings with Al contents >30 % (referring to the metallic fraction), wherefore it can be assumed that the Young's modulus is further decreasing with increasing Al contents [8,27].

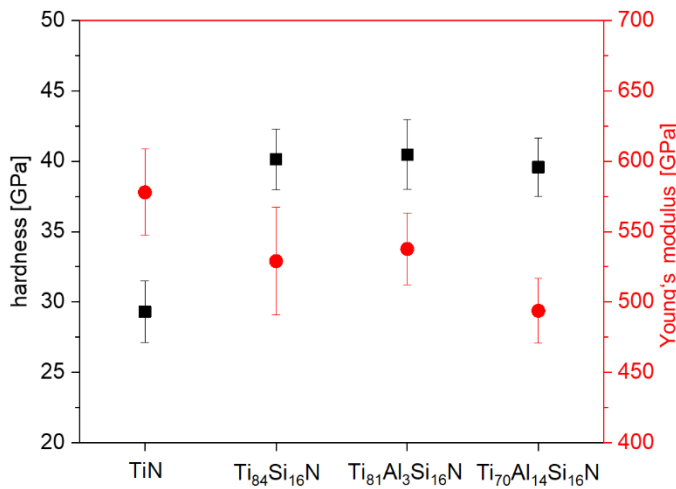


Fig. 4: Hardness and Young's modulus of Ti(Al,Si)N coatings.

In addition to hardness and Young's modulus, also the fracture behaviour plays an important role regarding the performance of protective coatings in cutting applications. However, quantitative values of the fracture stress and toughness of arc evaporated Ti(Al)SiN coatings are barely presented in literature, especially the effect of Al addition to TiSiN on the fracture properties has not been reported so far. Therefore, in this study the fracture stress and fracture toughness of Ti(Al,Si)N coatings were investigated by micro-cantilever bending experiments, which allows to assess the fracture properties without interference of substrate effects or residual stress [48,49]. Notched and unnotched micro-cantilevers were used to determine the fracture toughness and fracture stress, respectively, by evaluating the failure of the cantilevers in the stress-deflection curves. In Fig. 5(a), the stress-deflection curves of the unnotched micro-cantilevers of the

different Ti(Al,Si)N coatings are shown, which all exhibit a linear-elastic behaviour until failure occurs. Therefore, no plastic deformation is assumed to take place, verifying the brittle material behaviour. The stress-deflection curves correlate well with the determined Young's moduli shown in Fig. 4, as TiN exhibits the highest and Ti<sub>70</sub>Al<sub>14</sub>Si<sub>16</sub>N the lowest Young's modulus and TiN exhibits the steepest and Ti<sub>70</sub>Al<sub>14</sub>Si<sub>16</sub>N the flattest slope of all stress-deflection curves in Fig. 5(a). The resulting fracture stress and toughness from the micro-cantilever bending experiments for TiN, Ti<sub>84</sub>Si<sub>16</sub>N, Ti<sub>81</sub>Al<sub>3</sub>Si<sub>16</sub>N and Ti<sub>70</sub>Al<sub>14</sub>Si<sub>16</sub>N coatings are summarized in Fig. 5(b). TiN exhibits a fracture stress of  $2.7 \pm 0.2$  GPa and a  $K_{IC}$  value of  $2.4 \pm 0.3$  MPa $\times$ m<sup>1/2</sup>, which is in good agreement with  $K_{IC}$  values available in literature for sputtered TiN coatings [22,50,51]. Upon addition of Si, the fracture stress and toughness rise to  $3.1 \pm 0.5$  GPa and  $2.7 \pm 0.4$  MPa $\times$ m<sup>1/2</sup>, respectively. The fracture toughness of sputtered TiSiN coatings as a function of the Si content (0-13.8 at.%) was investigated by Bartosik et al. [22]. They found a maximum  $K_{IC}$  value of  $3.0 \pm 0.2$  MPa $\times$ m<sup>1/2</sup> at a Si content of 8.5 at.%, which is similar to the determined value for the arc evaporated TiSiN coating investigated in this work. The decrease in grain size and the resulting fine grained morphology that were identified as factors positively influencing the fracture toughness of TiSiN by Bartosik et al. can also be named as reasons for the enhanced fracture toughness of TiSiN over TiN found in this study. Furthermore, the  $\alpha$ -SiN<sub>x</sub> phase that was observed during HR-STEM investigations of the TiSiN coating in a previous work [35] can be suspected to have a positive effect on hindering crack propagation during fracture. Although the hardness and Young's moduli (Fig. 4) as well as the microstructure observed by XRD (Fig. 2) and SEM (Fig. 1) did not change distinctly upon addition of Al to TiSiN, the fracture properties were found to be strongly affected. While the fracture stress still remained constant at  $3.1 \pm 0.3$  GPa for Ti<sub>81</sub>Al<sub>3</sub>Si<sub>16</sub>N, the  $K_{IC}$  value slightly improved to  $2.9 \pm 0.3$  MPa $\times$ m<sup>1/2</sup>. Increasing the Al content to Ti<sub>70</sub>Al<sub>14</sub>Si<sub>16</sub>N resulted in a pronounced enhancement of the fracture properties, yielding a fracture stress of  $5.3 \pm 0.5$  GPa and a  $K_{IC}$  value of  $3.3 \pm 0.2$  MPa $\times$ m<sup>1/2</sup>. A possible explanation of the strong

improvement of the fracture properties for the higher Al content could be based on the investigations of the fracture dynamics and transformation toughening effect of  $Ti_{1-x}Al_xN$  by Sangiovanni et al. [52]. Based on ab initio molecular dynamics calculations, the authors reported a higher resistance to fracture and greater toughness of  $Ti_{50}Al_{50}N$  and  $Ti_{25}Al_{75}N$  solid solutions compared to  $TiN$  and a  $Ti_{75}Al_{25}N$  solid solution. This finding was attributed to local structural transformations from fcc-AlN to w-AlN beyond the elastic-response regime, which dissipates stress and prevents brittle failure. Although the coating in the present study contains only small amounts of Al ( $Ti_{70}Al_{14}Si_{16}N$ ), which according to Sangiovanni et al. does not undergo the local structural transformation to w-AlN, it has to be taken into account that also a significant amount of Si is present in our TiAlSiN coatings. Several authors have stated that the addition of Si to TiAlN favors the formation of w-AlN-rich domains [8,53,54]. Thus, it could be assumed that the local stress-induced transformations of fcc-AlN to w-AlN also take place in the  $Ti_{70}Al_{14}Si_{16}N$  coating in this study, resulting in a significant increase of fracture stress and  $K_{IC}$ . However, it still remains questionable if local structural transformations can take place beyond the elastic-response regime since the obtained stress-deflection curves shown in Fig. 5(a) indicate a purely elastic behavior until fracture for all investigated coatings. Stress-induced transformation of fcc-AlN to w-AlN has been observed experimentally for  $ZrN/Zr_{63}Al_{37}N$  multilayers on the nanoscale by Yalamanchili et al. [55]. A maximum fracture resistance was obtained for 2 nm thick  $Zr_{63}Al_{37}N$  layers, where fcc-AlN-rich domains undergo transformation to w-AlN when subjected to indentation-induced stress fields.

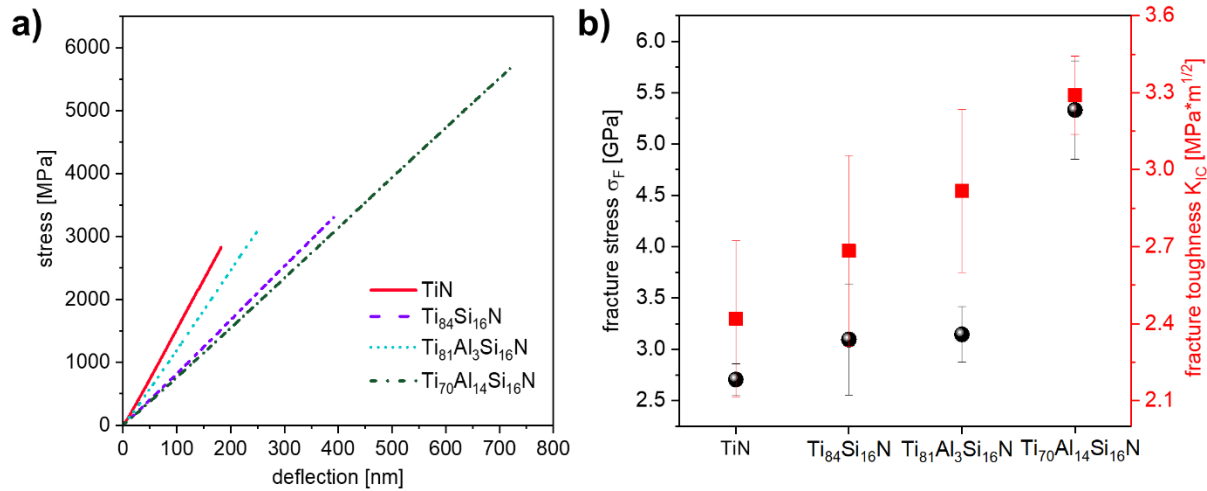


Fig. 5: Stress-deflection curves of micro-cantilevers of Ti(Al,Si)N coatings (a), as well as fracture stress and fracture toughness ( $K_{Ic}$ ) for the Ti(Al,Si)N coatings (b).

The post mortem fracture cross-sections of the notched micro-cantilevers, shown in Fig. 6, correlate well with the SEM micrographs of the Ti(Al,Si)N coatings from Fig. 1 and the FWHM of the coatings shown in Fig. 2(b). Significantly larger grains can be observed for the fractured cross-section of TiN (Fig. 6(a)) compared to the fine-grained structure of the three Ti(Al)SiN coatings. Due to the significantly smaller grain size of the Ti(Al)SiN coatings and thus the presence of more grain boundaries acting as crack deflection sites, a retained crack propagation - leading to stronger resistance to fracture - is obtained [22,56,57].



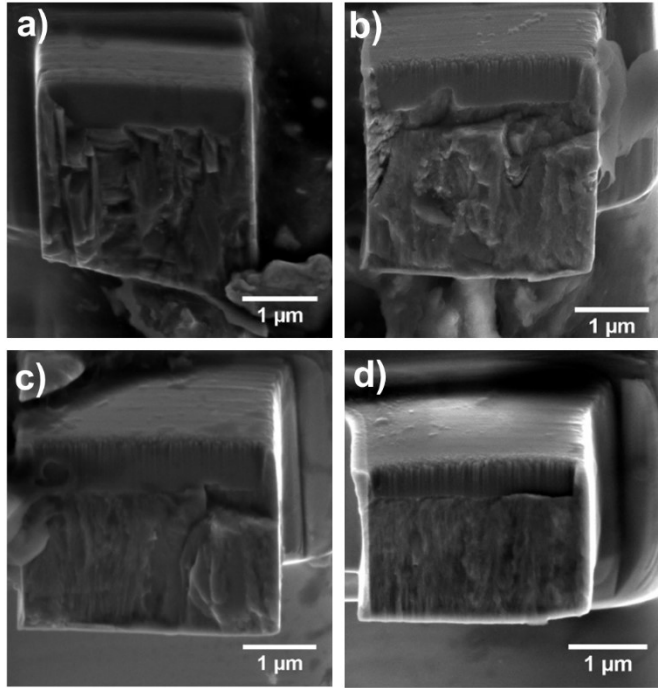


Fig. 6: SEM micrographs of the post mortem fracture cross-sections of notched micro-cantilevers from TiN (a), Ti<sub>84</sub>Si<sub>16</sub>N (b), Ti<sub>81</sub>Al<sub>3</sub>Si<sub>16</sub>N (c) and Ti<sub>70</sub>Al<sub>14</sub>Si<sub>16</sub>N (d).

#### 4. Conclusions

Within the scope of this study, the microstructure and mechanical properties of arc evaporated TiN, Ti<sub>84</sub>Si<sub>16</sub>N, Ti<sub>81</sub>Al<sub>3</sub>Si<sub>16</sub>N and Ti<sub>70</sub>Al<sub>14</sub>Si<sub>16</sub>N were evaluated systematically. As evidenced by X-ray diffraction and scanning electron microscopy, TiN exhibits large and columnar grains, which changes to a fine-grained and feather-like structure for Ti(Al)SiN coatings. Pole-figures and inverse pole-figures revealed a change of texture from a preferred (111) orientation for TiN to a preferred (200) orientation for Ti(Al)SiN in growth direction. This observation can be attributed to renucleation of TiN grains by the amorphous SiN<sub>x</sub> phase. The hardness values significantly increased upon addition of Si from 29 to 40 GPa as a result of grain-refinement and inhibited grain-boundary sliding and remained constant upon further alloying with Al. Micromechanical bending tests of unnotched and notched micro-cantilevers allowed to evaluate the fracture stress and

fracture toughness ( $K_{IC}$ ) of Ti(Al,Si)N coatings. Both, the fracture stress and  $K_{IC}$  value increased upon Si addition to TiN and further improved for alloying of TiSiN with low amounts of Al, resulting in a maximum  $K_{IC}$  of  $3.3 \pm 0.2 \text{ MPa}\cdot\text{m}^{1/2}$  for  $\text{Ti}_{70}\text{Al}_{14}\text{Si}_{16}\text{N}$ . The enhanced fracture properties can be attributed to the fine grained morphology due to Si addition and additionally local stress-induced transformation of fcc-AlN to w-AlN during fracture could be assumed to take place for the highest Al content of  $\text{Ti}_{70}\text{Al}_{14}\text{Si}_{16}\text{N}$ . The findings of this study show the great potential of arc evaporated TiAlSiN coatings with low Al contents such as  $\text{Ti}_{70}\text{Al}_{14}\text{Si}_{16}\text{N}$  for the cutting industry, as the high hardness of 40 GPa found for TiSiN can be sustained, while simultaneously the fracture properties are significantly enhanced.

## 5. Acknowledgments

The authors would like to thank Bernhard Sartory (Materials Center Leoben Forschung GmbH) for the SEM investigations of the cross-sections and Marianne Penoy, MSc. (CERATIZIT Luxembourg s.à.r.l.) for the GDOES measurements. The financial support by the Austrian Federal Ministry for Digital and Economic Affairs and the National Foundation for Research, Technology and Development is gratefully acknowledged.

## 6. References

- [1] C.L. Chang, C.T. Lin, P.C. Tsai, W.Y. Ho, W.J. Liu, D.Y. Wang, Mechanical and corrosion properties of (Ti,Si)N coating synthesized by cathodic arc plasma evaporation, *Surf. Coatings Technol.* 202 (2008) 5516–5520.
- [2] L. Chen, Y. Du, S.Q. Wang, A.J. Wang, H.H. Xu, Mechanical properties and microstructural evolution of TiN coatings alloyed with Al and Si, *Mater. Sci. Eng. A.* 502 (2009) 139–143.
- [3] A. Mège-Revil, P. Steyer, G. Thollet, R. Chiriach, C. Sigala, J.C. Sánchez-López, C. Esnouf, Thermogravimetric and in situ SEM characterisation of the oxidation

- phenomena of protective nanocomposite nitride films deposited on steel, *Surf. Coatings Technol.* 204 (2009) 893–901.
- [4] Y.C. Chim, X.Z. Ding, X.T. Zeng, S. Zhang, Oxidation resistance of TiN, CrN, TiAlN and CrAlN coatings deposited by lateral rotating cathode arc, *Thin Solid Films.* 517 (2009) 4845–4849.
- [5] P. Steyer, D. Pilloud, J.F. Pierson, J.P. Millet, M. Charnay, B. Stauder, P. Jacquot, Oxidation resistance improvement of arc-evaporated TiN hard coatings by silicon addition, *Surf. Coatings Technol.* 201 (2006) 4158–4162.
- [6] F. Vaz, L. Rebouta, M. Andritschky, M.F. da Silva, J.C. Soares, The effect of the addition of Al and Si on the physical and mechanical properties of titanium nitride, *J. Mater. Process. Technol.* 92–93 (1999) 169–176.
- [7] W. Münz, Titanium aluminum nitride films: A new alternative to TiN coatings, *J. Vac. Sci. Technol. A Vacuum, Surfaces, Film.* 4 (1986) 2717–2725.
- [8] F. Pei, H.J. Liu, L. Chen, Y.X. Xu, Y. Du, Improved properties of TiAlN coating by combined Si-addition and multilayer architecture, *J. Alloys Compd.* 790 (2019) 909–916.
- [9] M. Ahlgren, H. Blomqvist, Influence of bias variation on residual stress and texture in TiAlN PVD coatings, *Surf. Coat. Technol.* 200 (2005) 157–160.
- [10] B. Grossmann, N. Schalk, C. Czettel, M. Pohler, C. Mitterer, Phase composition and thermal stability of arc evaporated  $Ti_{1-x}Al_xN$  hard coatings with  $0.4 \leq x \leq 0.67$ , *Surf. Coat. Technol.* 309 (2017) 687–693.
- [11] L. Chen, J. Paulitsch, Y. Du, P.H. Mayrhofer, Thermal stability and oxidation resistance of Ti-Al-N coatings, *Surf. Coat. Technol.* 206 (2012) 2954–2960.
- [12] P.H. Mayrhofer, A. Hörling, L. Karlsson, J. Sjöln, T. Larsson, C. Mitterer, L. Hultman, Self-organized nanostructures in the Ti-Al-N system, *Appl. Phys. Lett.* 83 (2003) 2049–2051.
- [13] S. Carvalho, L. Rebouta, A. Cavaleiro, L.A. Rocha, J. Gomes, E. Alves,

- Microstructure and mechanical properties of nanocomposite (Ti,Si,Al) N coatings, *Thin Solid Films*. 398–399 (2001) 391–396.
- [14] A. Miletić, P. Panjan, B. Škorić, M. Čekada, G. Dražič, J. Kovač, Microstructure and mechanical properties of nanostructured Ti–Al–Si–N coatings deposited by magnetron sputtering, *Surf. Coat. Technol.* 241 (2014) 105–111.
- [15] S. Veprek, R.F. Zhang, M.G.J. Veprek-Heijman, S.H. Sheng, A.S. Argon, Superhard nanocomposites: Origin of hardness enhancement, properties and applications, *Surf. Coat. Technol.* 204 (2010) 1898–1906.
- [16] F. Pei, Y.X. Xu, L. Chen, Y. Du, H.K. Zou, Structure, mechanical properties and thermal stability of  $Ti_{1-x}Si_xN$  coatings, *Ceram. Int.* 44 (2018) 15503–15508.
- [17] M. Sperr, Z.L. Zhang, Y.P. Ivanov, P.H. Mayrhofer, M. Bartosik, Correlating elemental distribution with mechanical properties of  $TiN/SiN_x$  nanocomposite coatings, *Scr. Mater.* 170 (2019) 20–23.
- [18] S.K. Kim, P.V. Vinh, J.H. Kim, T. Ngoc, Deposition of superhard TiAlSiN thin films by cathodic arc plasma deposition, *Surf. Coat. Technol.* 200 (2005) 1391–1394.
- [19] D. Pilloud, J.F. Pierson, M.C. Marco de Lucas, A. Cavaleiro, Study of the structural changes induced by air oxidation in Ti-Si-N hard coatings, *Surf. Coatings Technol.* 202 (2008) 2413–2417.
- [20] S. Vepřek, Conventional and new approaches towards the design of novel superhard materials, *Surf. Coatings Technol.* 97 (1997) 15–22.
- [21] M. Bartosik, C. Rumeau, R. Hahn, Z.L. Zhang, P.H. Mayrhofer, Fracture toughness and structural evolution in the TiAlN system upon annealing, *Sci. Rep.* 7 (2017) 16476.
- [22] M. Bartosik, R. Hahn, Z.L. Zhang, I. Ivanov, M. Arndt, P. Polcik, P.H. Mayrhofer, Fracture toughness of Ti-Si-N thin films, *Int. J. Refract. Met. Hard Mater.* 72 (2018) 78–82.
- [23] M. Pfeiler, J. Zechner, M. Penoy, C. Michotte, C. Mitterer, M. Kathrein, Improved

- oxidation resistance of TiAlN coatings by doping with Si or B, *Surf. Coat. Technol.* 203 (2009) 3104–3110.
- [24] D. Yu, C. Wang, X. Cheng, F. Zhang, Microstructure and properties of TiAlSiN coatings prepared by hybrid PVD technology, *Thin Solid Films.* 517 (2009) 4950–4955.
- [25] W. Tillmann, M. Dildrop, Influence of Si content on mechanical and tribological properties of TiAlSiN PVD coatings at elevated temperatures, *Surf. Coat. Technol.* 321 (2017) 448–454.
- [26] G.S. Kim, B.S. Kim, S.Y. Lee, J.H. Hahn, Effect of Si content on the properties of TiAl–Si–N films deposited by closed field unbalanced magnetron sputtering with vertical magnetron sources, *Thin Solid Films.* 506–507 (2006) 128–132.
- [27] L. Zhu, C. Song, W. Ni, Y. Liu, Effect of 10 % Si addition on cathodic arc evaporated TiAlSiN coatings, *Trans. Nonferrous Met. Soc. China.* 26 (2016) 1638–1646.
- [28] Y. Wang, H. Zhang, C. Luo, X. Ran, Z. Ren, S. Duo, Influence of Al Content on Micro-Properties of TiAlSiN Coatings Deposited by Plasma Enhanced Magnetron Sputtering, *Mater. Sci. Eng.* 678 (2019) 012164.
- [29] F. Bachmann, R. Hielscher, H. Schaeben, Texture Analysis with MTEX – Free and Open Source Software Toolbox, *Solid State Phenom.* 160 (2010) 63–68.
- [30] The certification of standard reference material 660C for powder diffraction | NIST, (n.d.). <https://www.nist.gov/publications/certification-standard-reference-material-660c-powder-diffraction> (accessed June 25, 2020).
- [31] W.C. Oliver, G.M. Pharr, An improved technique for determining hardness and elastic modulus using load and displacement sensing indentation experiments, *J. Mater. Res.* 7 (1992) 1564–1583.
- [32] K. Matoy, H. Schönherr, T. Detzel, T. Schöberl, R. Pippan, C. Motz, G. Dehm, A comparative micro-cantilever study of the mechanical behavior of silicon based passivation films, *Thin Solid Films.* 518 (2009) 247–256.

- [33] A.O. Eriksson, J.Q. Zhu, N. Ghafoor, M.P. Johansson, J. Sjölen, J. Jensen, M. Odén, L. Hultman, J. Rosén, Layer formation by resputtering in Ti–Si–C hard coatings during large scale cathodic arc deposition, *Surf. Coat. Technol.* 205 (2011) 3923–3930.
- [34] A. Flink, T. Larsson, J. Sjölen, L. Karlsson, L. Hultman, Influence of Si on the microstructure of arc evaporated (Ti,Si)N thin films; evidence for cubic solid solutions and their thermal stability, *Surf. Coatings Technol.* 200 (2005) 1535–1542.
- [35] Y. Moritz, C. Saringer, M. Tkadletz, A. Stark, N. Schell, I. Letofsky-Papst, C. Czettl, M. Pohler, N. Schalk, Oxidation behavior of arc evaporated TiSiN coatings investigated by in-situ synchrotron X-ray diffraction and HR-STEM, *Surf. Coat. Technol.* 404 (2020) 126632.
- [36] D. Rafaja, A. Poklad, V. Klemm, G. Schreiber, D. Heger, M. Šíma, M. Dopita, Some consequences of the partial crystallographic coherence between nanocrystalline domains in Ti–Al–N and Ti–Al–Si–N coatings, *Thin Solid Films.* 514 (2006) 240–249.
- [37] S.D. Gates-Rector, T.N. Blanton, The Powder Diffraction File: A Quality Materials Characterization Database, *Powder Diffr.* 34 (2019) 352–360.
- [38] W. Cao, C.A. Randall, Grain size and domain size relations in bulk ceramic ferroelectric materials, *J. Phys. Chem Solids.* 57 (1996) 1499–1505.
- [39] Y. Kim, Y. Cho, S. Hong, S. Bühlmann, H. Park, D.-K. Min, S.-H. Kim, K. No, Correlation between grain size and domain size distributions in ferroelectric media for probe storage applications, *Appl. Phys. Lett.* 89 (2006) 162907.
- [40] F. Vaz, L. Rebouta, P. Goudeau, J. Pacaud, H. Garem, J. Rivière, A. Cavaleiro, E. Alves, Characterisation of  $Ti_{1-x}Si_xN_y$  nanocomposite films, *Surf. Coatings Technol.* 133–134 (2000) 307–313.
- [41] A. Kimura, H. Hasegawa, K. Yamada, T. Suzuki, Effects of Al content on hardness, lattice parameter and microstructure of  $Ti_{1-x}Al_xN$  films, *Surf. Coat. Technol.* 120–121 (1999) 438–441.

- [42] I.A. Abrikosov, A. Knutsson, B. Alling, F. Tasnádi, H. Lind, L. Hultman, M. Odén, Phase Stability and Elasticity of TiAlN, *Materials (Basel)*. 4 (2011) 1599–1618.
- [43] A. Flink, M. Beckers, J. Sjölen, T. Larsson, S. Braun, L. Karlsson, L. Hultman, The location and effects of Si in  $(\text{Ti}_{1-x}\text{Si}_x)\text{N}_y$  thin films, *J. Mater. Res.* 24 (2009) 2483–2498.
- [44] G. Abadias, V.V. Uglov, I.A. Saladukhin, S.V. Zlotski, G. Tolmachova, S.N. Dub, A. Janse van Vuuren, Growth, structural and mechanical properties of magnetron-sputtered ZrN/SiN<sub>x</sub> nanolaminated coatings, *Surf. Coat. Technol.* 308 (2016) 158–167.
- [45] M. Diserens, J. Patscheider, F. Lévy, Mechanical properties and oxidation resistance of nanocomposite TiN-SiN<sub>x</sub> physical-vapor-deposited thin films, *Surf. Coatings Technol.* 120–121 (1999) 158–165.
- [46] T. Chen, Z. Xie, F. Gong, Z. Luo, Z. Yang, Correlation between microstructure evolution and high temperature properties of TiAlSiN hard coatings with different Si and Al content, *Appl. Surf. Sci.* 314 (2014) 735–745.
- [47] P.H. Mayrhofer, C. Mitterer, Structure/property relations in PVD hard coatings, in: S. Pandalai (Ed.), *Recent Res. Devel. Vac. Sci. Tech.*, Transworld research network, Trivandrum, 2003: pp. 71–97.
- [48] G. Dehm, B.N. Jaya, R. Raghavan, C. Kirchlechner, Overview on micro- and nanomechanical testing: New insights in interface plasticity and fracture at small length scales, *Acta Mater.* 142 (2018) 248–282.
- [49] J. Ast, M. Ghidelli, K. Durst, M. Göken, M. Sebastiani, A.M. Korsunsky, A review of experimental approaches to fracture toughness evaluation at the micro-scale, *Mater. Des.* 173 (2019) 107762.
- [50] S. Massl, W. Thomma, J. Keckes, R. Pippan, Investigation of fracture properties of magnetron-sputtered TiN films by means of a FIB-based cantilever bending technique, *Acta Mater.* 57 (2009) 1768–1776.
- [51] S. Kataria, S.K. Srivastava, P. Kumar, G. Srinivas, Siju, J. Khan, D. V Sridhar Rao,

- H.C. Barshilia, Nanocrystalline TiN coatings with improved toughness deposited by pulsing the nitrogen flow rate, *Surf. Coat. Technol.* 206 (2012) 4279–4286.
- [52] D.G. Sangiovanni, F. Tasnádi, L.J.S. Johnson, M. Odén, I.A. Abrikosov, Strength, transformation toughening, and fracture dynamics of rocksalt-structure  $\text{Ti}_{1-x}\text{Al}_x\text{N}$  ( $0 \leq x \leq 0.75$ ) alloys, *Phys. Rev. Mater.* 4 (2020) 033605.
- [53] L. Chen, B. Yang, Y. Xu, F. Pei, L. Zhou, Y. Du, Improved thermal stability and oxidation resistance of Al–Ti–N coating by Si addition, *Thin Solid Films.* 556 (2014) 369–375.
- [54] A. Flink, J.M. Andersson, B. Alling, R. Daniel, J. Sjöln, L. Karlsson, L. Hultman, Structure and thermal stability of arc evaporated  $(\text{Ti}_{0.33}\text{Al}_{0.67})_{1-x}\text{Si}_x\text{N}$  thin films, *Thin Solid Films.* 517 (2008) 714–721.
- [55] K. Yalamanchili, I.C. Schramm, E. Jiménez-Piqué, L. Rogström, F. Mücklich, M. Odén, N. Ghafoor, Tuning hardness and fracture resistance of  $\text{ZrN}/\text{Zr}_{0.63}\text{Al}_{0.37}\text{N}$  nanoscale multilayers by stress-induced transformation toughening, *Acta Mater.* 89 (2015) 22–31.
- [56] C. Kainz, M. Pohler, G.C. Gruber, M. Tkadletz, A.S. Ebner, C. Czettl, N. Schalk, Influence of bias voltage on microstructure, mechanical properties and thermal stability of arc evaporated  $\text{Cr}_{0.74}\text{Ta}_{0.26}\text{N}$  coatings, *Surf. Coat. Technol.* 417 (2021) 127212.
- [57] C. Kainz, N. Schalk, M. Tkadletz, C. Mitterer, C. Czettl, Microstructure and mechanical properties of CVD TiN/TiBN multilayer coatings, *Surf. Coat. Technol.* 370 (2019) 311–319.



# Publication II

## Oxidation behavior of arc evaporated TiSiN coatings investigated by *in-situ* synchrotron X-ray diffraction and HR-STEM

Yvonne Moritz, Christian Saringer, Michael Tkadletz, Andreas Stark, Norbert Schell, Ilse  
Letofsky-Papst, Christoph Czettel, Markus Pohler, Nina Schalk

Surface & Coatings Technology 404 (2020) 126632

## Oxidation behavior of arc evaporated TiSiN coatings investigated by *in-situ* synchrotron X-ray diffraction and HR-STEM

Yvonne Moritz<sup>a</sup>, Christian Saringer<sup>a</sup>, Michael Tkadletz<sup>b</sup>, Andreas Stark<sup>c</sup>, Norbert Schell<sup>c</sup>, Ilse Letofsky-Papst<sup>d</sup>, Christoph Czettl<sup>e</sup>, Markus Pohler<sup>e</sup>, Nina Schalk<sup>a</sup>

<sup>a</sup> Christian Doppler Laboratory for Advanced Coated Cutting Tools at the Department of Materials Science, Montanuniversität Leoben, Franz-Josef-Strasse 18, 8700 Leoben, Austria

<sup>b</sup> Department of Materials Science, Montanuniversität Leoben, Franz-Josef-Strasse 18, 8700 Leoben, Austria

<sup>c</sup> Institute of Materials Research, Helmholtz-Zentrum Geesthacht, Max-Planck-Strasse 1, 21502 Geesthacht, Germany

<sup>d</sup> Institute for Electron Microscopy and Nanoanalysis and Center for Electron Microscopy, Graz University of Technology, NAWI Graz, Steyrergasse 17, 8010 Graz, Austria

<sup>e</sup> Ceratizit Austria GmbH, Metallwerk-Plansee-Strasse 71, 6600 Reutte, Austria

### Abstract

Owing to its excellent mechanical and thermal properties and outstanding oxidation resistance, TiSiN is used for protective hard coatings for cutting applications. While several reports confirm the oxidation stability of TiSiN up to temperatures above 800 °C, literature is currently lacking a thorough investigation of the oxidation sequence of this coating system. Thus, in this study the oxidation mechanism of TiSiN was monitored via *in-situ* synchrotron X-ray diffraction (XRD) and complemented by a detailed analysis of the microstructure and elemental composition of oxidized coatings.

A TiSiN coating was deposited by cathodic-arc evaporation in an industrial scale deposition plant. *In-situ* synchrotron XRD experiments of the powdered coating showed an oxidation stability up to ~830 °C, followed by the formation of both, rutile and anatase TiO<sub>2</sub> with increasing temperature. The formation of anatase during oxidation was confirmed by Raman and XRD investigations on a solid coating. High-resolution scanning transmission electron microscopy investigations revealed the oxidation of only several hundred nm of the coating surface after oxidation at 930 °C for 5 minutes, while increasing the temperature to 1130 °C resulted in full oxidation of the Ti(Si)N nanocrystals, accompanied by high porosity and significant grain coarsening. Furthermore, elemental analysis showed the presence of TiO<sub>2</sub> grains surrounded by an amorphous Si-O-N phase as well as the formation of a TiO<sub>2</sub> top layer due to diffusion of Ti to the surface. The obtained results provide detailed and novel insight into the oxidation mechanism of TiSiN as well as on the microstructure of oxidized TiSiN coatings.

**Keywords:** hard coatings, PVD, oxidation, Sequential Rietveld refinement, STEM

## 1. Introduction

For several decades, physical vapour deposited (PVD) TiN hard coatings have been investigated and widely used to enhance the performance and lifetime of cutting tools [1–4]. Although this system exhibits decent mechanical properties such as a reasonable hardness and wear resistance [5,6], TiN coatings suffer from the drawback of severe oxidation above 550 °C [7]. Alloying with Si has shown to drastically enhance the mechanical properties as well as the oxidation stability of TiN coatings by more than 200 °C [8,9].

Many favorable properties of PVD TiSiN coatings have been attributed to the presence of a nanocomposite structure consisting of Ti(Si)N nanocrystallites embedded in an amorphous SiN<sub>x</sub> phase [10,11]. Exceptionally high hardness values in the range of

37 to 45 GPa were reported for this coating system by several authors [12–20], which are a result of the grain refinement induced by silicon addition and the formation of an amorphous tissue phase, inhibiting grain-boundary sliding [8,21,22]. Moreover, annealing experiments under vacuum conditions showed an excellent thermal stability of TiSiN powdered samples up to 1300 °C due to retarded grain coarsening of the TiN nanocrystallites when surrounded by an amorphous SiN<sub>x</sub> tissue phase. At annealing temperatures between 1450 and 1550 °C, decomposition into fcc-TiN, β-Si<sub>3</sub>N<sub>4</sub>, TiSi<sub>2</sub> and diamond cubic Si takes place [12].

The addition of Si to TiN does not only influence the mechanical properties and thermal stability, but also considerably enhances the oxidation resistance. This improvement is attributed to the amorphous SiN<sub>x</sub> phase acting as an oxygen diffusion barrier at the grain boundaries [8]. In kinetic studies, the partly inhibited oxygen diffusion was shown to result in a five times lower oxidation rate at 800 °C for TiSiN compared to TiN [9]. Pilloud et al. found that already small amounts of Si in the range of 1-2 at.% significantly slow down the oxidation process, resulting in a decreased thickness of the formed oxide scale at a defined temperature and oxidation time [23]. Furthermore, analogously to Steyer et al. [9], they detected small amounts of anatase TiO<sub>2</sub> besides the predominantly present rutile TiO<sub>2</sub> in X-ray diffractograms and Raman spectra of oxidized TiSiN coatings. The authors attributed this finding to the fact that anatase is stabilized at low grain sizes up to ~11 nm. Grain coarsening during oxidation is prevented to a certain degree by the amorphous SiN<sub>x</sub> phase surrounding the nanocrystalline grains, thus, contrary to pure TiN coatings, anatase can occur during oxidation of TiSiN [23]. So far, no studies on the detailed oxidation mechanism of PVD TiSiN considering the temperature-dependent phase evolution of rutile and anatase TiO<sub>2</sub> have been published. In addition, literature is lacking a thorough microstructural investigation of oxidized TiSiN coatings using high-resolution methods.

Thus, in this work the oxidation sequence of a powdered TiSiN coating was investigated by *in-situ* synchrotron X-ray diffraction (XRD) at the P07 beamline at PETRA III in Hamburg. The powdered coating was annealed in air up to 1200 °C and 2D X-ray patterns were recorded continuously. Sequential Rietveld refinement allowed to monitor the temperature-dependent phase composition as well as the thermal expansion of Ti(Si)N. Differential scanning calorimetry (DSC) and thermogravimetric analysis (TGA) of the powder complemented the *in-situ* synchrotron XRD experiment. Furthermore, the solid TiSiN coating deposited on sapphire substrates was oxidized at two different temperatures, in order to investigate the microstructure and chemical bonding state of the coating after the oxidation process via X-ray photoelectron spectroscopy (XPS), Raman spectroscopy and high-resolution scanning transmission electron microscopy (HR-STEM).

## 2. Experimental

The TiSiN coating with a thickness of ~4 µm, investigated in this study, was deposited by cathodic arc evaporation in an industrial scale Oerlikon Balzers Innova deposition plant. The targets used in the deposition process were produced powder metallurgically from Ti and TiSi<sub>2</sub> with an elemental composition of Ti<sub>80</sub>Si<sub>20</sub>. The coating was synthesized in pure N<sub>2</sub> atmosphere at a pressure of 3.5 × 10<sup>-2</sup> mbar, a bias voltage of -35 V and a substrate temperature of 480 °C for 220 minutes, using a combined radiative and plasma heating procedure, with temperature measurement by thermocouples placed near the substrate. The cathodes were operated at an DC arc current of 180 A. Prior to deposition, the substrates were ion-etched in a pure argon plasma. Cemented carbide (92 wt.% WC, 6 wt.% Co and 2 wt.% mixed carbides) in SNUN geometry according to ISO 1832, single crystalline sapphire with (001) orientation and mild steel foil served as substrates. After the deposition process, the coated steel foil was dissolved in diluted nitric acid in order to obtain a TiSiN powder sample for *in-situ* synchrotron powder XRD and DSC investigations.

The elemental composition of the as-deposited TiSiN coating on cemented carbide was evaluated by glow discharge optical emission spectroscopy (GDOES) using a Jobin-Yvon Horiba JY10000 spectroscope and was determined to be  $\text{Ti}_{42}\text{Si}_8\text{N}_{50}$ . No oxygen could be confirmed within the coating as the content was below the GDOES detection limit. Furthermore, the microstructure of the coating was analyzed by a Bruker D8 Advance X-ray diffractometer in grazing incidence geometry. A Göbel mirror was utilized for collimation of the  $\text{Cu-K}\alpha$  radiation, which was directed at the sample with an incidence angle of  $2^\circ$ . The  $2\theta$ -scan was recorded using an energy-dispersive Sol-X detector, where the step-size was set to  $0.02^\circ$  with a measurement time of 1.0 s per step.

The TiSiN powder was investigated by *in-situ* synchrotron powder XRD at the high energy materials science beamline P07 of the Helmholtz-Zentrum Geesthacht at PETRA III in Hamburg [24]. The powder was placed in a Pt crucible within an inductively heated high temperature set-up (according to ref. [25]) and heated in air from 100 to 1200 °C with a heating rate of 20 K/min. The energy of the X-ray beam was 104 keV, corresponding to a wavelength of 0.11965 Å. 2D X-ray diffractograms in Debye-Scherrer geometry were recorded every ~4 K during the heating cycle with a digital X-ray detector Perkin Elmer XRD 1621, leading to a total of 272 frames. The exposure time for each frame was 5 s. In order to evaluate the recorded 2D patterns, calibration and azimuthal integration to 1D diffractograms was proceeded using the program Dawn2 [26,27]. The subsequent Rietveld refinement was carried out using the software Topas 6 by Bruker. The influence of instrumental parameters on the XRD patterns was corrected by refining the recorded diffractogram of a standard LaB6 powder sample (NIST 660c [28]). Hereby, the instrument function was determined and applied for refining the recorded TiSiN powder patterns. Evaluation of the 272 recorded diffractograms at different temperatures was carried out using a sequential Rietveld refinement approach as published by Saringer et al. [25], where the output parameters (e.g. lattice parameter) of refinement  $n$  are automatically used as input parameters for the subsequent refinement  $n+1$ .

Crystallographic information files (cifs) allowed modelling of the occurring phases and were taken from the Crystallography Open Database (COD) [29]. The COD files of TiN (COD-code: 1011099), rutile TiO<sub>2</sub> (COD-code: 1534781) and anatase TiO<sub>2</sub> (COD-code: 1526931) were utilized to generate reasonable input parameters. Two main criteria were applied to identify a satisfying Rietveld refinement of the collected data. A change of  $\chi^2 < 0.001$ , which indicates the difference between observed and calculated powder patterns within one iteration step, was required to fulfill the convergence criterion and the displayed difference curve between the measured and the modelled pattern was considered a further measure for the goodness of fit. Examples of several measured and modelled patterns including the respective difference curves are available as supplementary material online.

Complementary to the *in-situ* synchrotron powder XRD investigations, DSC and TGA measurements of the TiSiN powder were carried out in synthetic air using a Setaram Setsys Evo 2400 DSC system. Approximately 20 mg of the powder were filled into an Al<sub>2</sub>O<sub>3</sub> crucible and heated up to 1200 °C with a heating rate of 20 K/min, analogously to the heating rate applied in the *in-situ* synchrotron XRD experiments. In addition, two TiSiN samples deposited on sapphire-substrates were oxidized in a Nabertherm N11/HR furnace in ambient air up to 930 °C and 1130 °C, respectively. The respective maximum temperature was held constant for 5 minutes. Analogously to the as-deposited coating on cemented carbide, the microstructure of the oxidized coatings was analyzed using the laboratory Bruker D8 Advance X-ray diffractometer in grazing incidence geometry. Information about the chemical bonding structure after oxidation was obtained by XPS, utilizing an Omicron Multiprobe surface analysis system, equipped with a DAR 400 X-ray source, an XM 500 quartz crystal monochromator and an EA 125 hemispherical electron analyzer with a 5 channel pulse counting channeltron. The X-ray excitation energy used for the XPS analysis was 1486.7 eV (Al-K $\alpha_1$ ). The pass energy was set to 20 eV, yielding an energy resolution of 0.5 eV. Calibration and correction of the binding energy

of the recorded spectra were proceeded by consideration of the C-C bond of the C1s peak at 284.6 eV, which is present in all samples due to hydrocarbon surface contamination. The obtained XPS spectra were subjected to peak fitting using a convolution of Lorentzian and Gaussian shape functions, utilizing the Unifit 2017 software.

To gain further insight into the phase composition of the oxidized coatings, complementary Raman spectroscopy was conducted using a LabRam HR800 spectrometer from Jobin Yvon. The spectrometer was equipped with a frequency-doubled Nd-YAG laser (wavelength = 532 nm) and Raman spectra were recorded between 100 and 1500  $\text{cm}^{-1}$ . In order to develop a deeper understanding of the microstructure as well as of the phase and elemental composition of the as-deposited and oxidized TiSiN coatings on the nanoscale, high-resolution scanning transmission electron microscopy (HR-STEM) investigations were conducted. The STEM samples were prepared by focused ion beam (FEI Nova200) milling. High resolution STEM investigations were performed on a probe corrected FEI Titan 3 G2 60–300 (S/TEM) microscope with an X-FEG Schottky field-emission electron source operated at 300 kV (current of 150 pA, beam diameter of 1 Å). The spectrum images were acquired with an FEI Super-X detector (Chemi-STEM technology), consisting of four separate silicon drift detectors. STEM data were evaluated using the Gatan Digital Micrograph Software. Fast Fourier transformations (FFT) of grains observed in the HR-STEM images allowed to determine the d-spacing and subsequently enabled a phase-assignment of individual grains.

### 3. Results and Discussion

X-ray diffractograms of the TiSiN coating deposited on cemented carbide as well as of the powdered TiSiN coating were recorded at room temperature using a laboratory X-ray source and a synchrotron radiation source, respectively. The comparison of these two diffractograms is shown in Fig. 1(a), where the d-spacing was chosen for labelling the x-axis, as the energy used at the synchrotron radiation facility is different to the one used for the laboratory X-ray source, resulting in different  $2\theta$  angles. It can be seen that the



powder production has no influence on the crystalline phase of the TiSiN coating, as both X-ray diffractograms only show reflections of the face-centered cubic (fcc) TiN phase. Other peaks present stem from the Pt-crucible used for the synchrotron measurement in case of the powdered coating and from the cemented carbide (CC) in case of the solid coating. In accordance with other publications, no crystalline SiN<sub>x</sub> or titanium silicide peaks can be observed in either of the X-ray diffractograms, indicating that the Si is present within a solid solution, substituting for Ti atoms in the lattice and/or within an X-ray amorphous SiN<sub>x</sub> phase [12,16,17,30–33]. Fig. 1(a) further reveals a shift to lower d-spacing (higher diffraction angle) for the powdered TiSiN coating compared to the coating on CC. This can be related to the fact that the powdered coating is – on the contrary to the solid coating on CC – free of macroscopic stress. However, the peaks of the powdered coating appear to shift also to a lower d-spacing compared to the indicated standard peak positions for TiN (ICDD pdf-Nr. 00-038-1420). Rietveld refinement of the respective X-ray diffractogram yields a lower lattice parameter for the TiSiN powder sample of  $4.21 \text{ \AA} \pm 0.01$  compared to the literature value of  $4.24 \text{ \AA}$  for pure TiN. The decrease in lattice parameter was already reported in other publications and indicates the presence of a solid solution, where Ti atoms are substituted by Si atoms in the lattice [16,22,33]. To further clarify if an amorphous SiN<sub>x</sub> phase is present besides the Ti(Si)N solid solution, HR-STEM investigations were conducted which are displayed in Fig. 1(b). The annular dark-field (ADF) image of the coating exhibits a feather-like structure. At higher magnification (blue framed insert), clearly crystalline and amorphous regions are visible that can be differentiated even better in the shown Inverse Fast Fourier Transformation (IFFT) image. Diffuse appearance of the IFFT on the left-hand side of the dashed line indicates overlapping amorphous and crystalline regions within the lamella. Thus, the XRD and HR-STEM investigations lead to the conclusion that the as-deposited structure of the TiSiN coating consists of a nanocrystalline Ti(Si)N solid solution surrounded by an amorphous SiN<sub>x</sub> tissue phase.

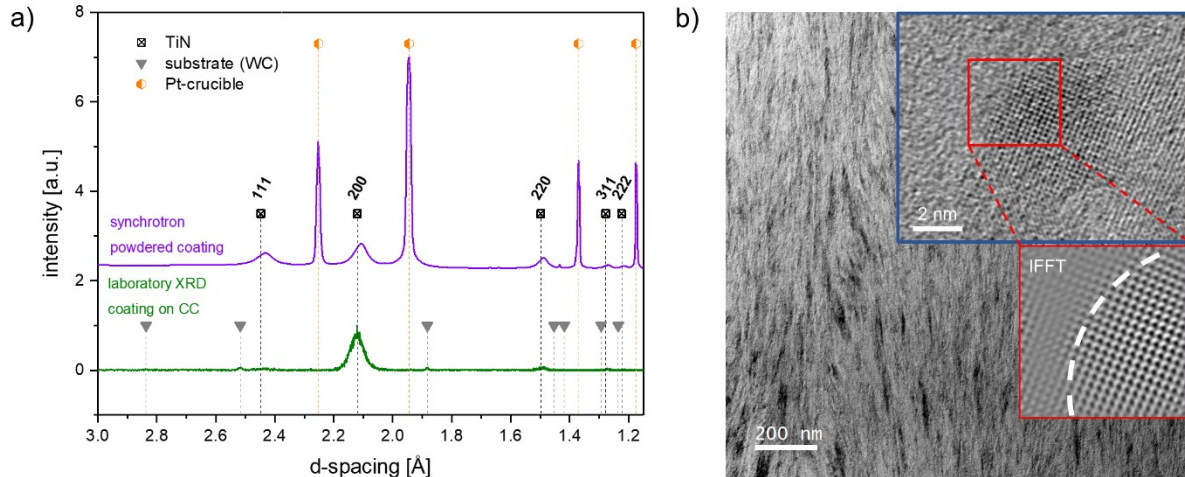


Fig. 1: Room-temperature X-ray diffractograms of the powdered TiSiN coating recorded at the synchrotron radiation facility and of the TiSiN coating deposited on cemented carbide measured in grazing incidence geometry using a laboratory X-ray source (a). ADF image of the as-deposited coating deposited on cemented carbide and insert at higher magnification (blue frame) revealing crystalline and amorphous regions that can be seen in more detail in the IFFT image (b).

### 3.1 Oxidation of Powdered Coating

To gain insight into the temperature-dependent phase composition of TiSiN during the oxidation process, 2D X-ray patterns of the powdered sample were collected *in-situ* at the P07 Beamline at DESY during annealing in ambient atmosphere up to 1200 °C. The recorded Debye-Scherrer rings were azimuthally integrated over an angular range from 0 to 360 °C in order to convert the 2D diffraction data to 1D diffractograms. Sequential Rietveld refinement of the 272 1D patterns using the Topas 6 software allowed to generate the phase evolution of the refined patterns with increasing oxidation temperature shown in Fig. 2(a). Peaks, resulting from the Pt-crucible, were eliminated in the calculated patterns by excluding these contributions during Rietveld refinement. The position of Bragg reflections of the TiN (ICDD pdf-Nr. 00-038-1420), anatase TiO<sub>2</sub> (ICDD pdf-Nr. 01-075-2544) and rutile TiO<sub>2</sub> (ICDD pdf-Nr. 01-079-5860) phase at room temperature are indicated by symbols and dashed lines within the phase-plot. It can be observed that all

peaks exhibit a shift to lower diffraction angles with increasing temperature as a result of the thermal expansion of the lattices. When taking a closer look at the phase transformations during oxidation of TiSiN, the XRD phase-plot can be divided into four different zones, separated by horizontal white dashed lines in Fig. 2(a). In zone (I), up to a temperature of  $\sim 830$  °C, only reflections related to fcc-TiN are visible, confirming the excellent oxidation resistance of TiSiN that was already reported by several authors [8,9,23]. When increasing the temperature above 830 °C zone (II) is reached, where rutile TiO<sub>2</sub> is formed. The observed onset temperature for the phase transformation corresponds well to the DSC measurement shown in Fig. 2(b), where the oxidation onset found by XRD is indicated. A third phase, namely anatase TiO<sub>2</sub>, appears in the phase plot at the beginning of zone (III) at  $\sim 920$  °C, which is supported by a shoulder of the exothermic peak in the DSC signal. While the oxidation of pure TiN usually only yields the formation of rutile TiO<sub>2</sub>, some authors have reported the additional occurrence of anatase TiO<sub>2</sub> for TiSiN coatings [9,23], which agrees well with the results of this *in-situ* XRD measurement. Above 1130 °C, full oxidation of the crystalline Ti(Si)N phase is obtained. Thus, in zone (IV) primarily rutile TiO<sub>2</sub> and small amounts of anatase TiO<sub>2</sub> are present. The DSC signal shows a maximum of the TiO<sub>2</sub>-related exothermic peak at  $\sim 1040$  °C, which is followed by another exothermic peak at  $\sim 1150$  °C. The latter most probably stems from the oxidation of the amorphous SiN<sub>x</sub> phase into Si-O-N, which would not be observable in the XRD phase-plot due to the X-ray amorphous structure of both phases. This would be in agreement with the TGA signal, which continues to increase after the oxidation to TiO<sub>2</sub> has taken place, leading to the assumption that the exothermic peak observed at  $\sim 1150$  °C is the result of a further oxidation process.

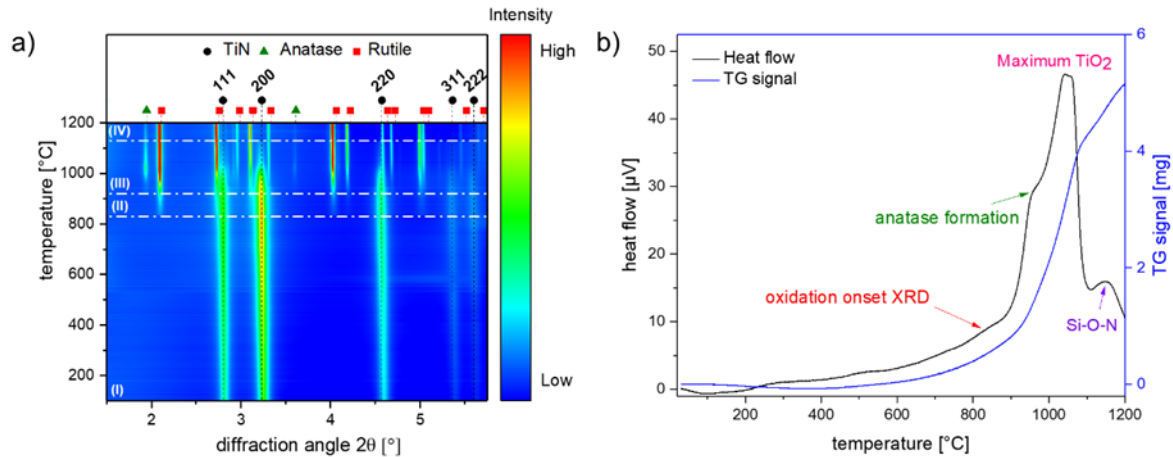


Fig. 2: Phase-plot of the azimuthally integrated and modelled 2D XRD data obtained by in-situ powder diffraction at the synchrotron radiation facility as a function of the oxidation temperature (a). Heat flow and thermogravimetric signal as a function of the oxidation temperature of the powdered TiSiN sample with indicated phase transformations (b).

By applying a sequential Rietveld approach for the analysis of a large number of XRD patterns it is possible to continuously monitor parameters such as the phase composition of the sample or the evolution of the lattice parameters over the whole investigated temperature range. In Fig. 3(a) the quantitative phase composition after the oxidation onset of TiSiN at  $\sim 830$  °C is shown. A threshold of  $> 4$  wt.% of the rutile phase was assumed to determine the onset temperature. Below this value an unambiguous quantification of the rutile fraction seemed inappropriate. Starting at 830 °C a continuous increase in the weight percent of rutile TiO<sub>2</sub> can be observed, while the amount of the TiSiN phase decreases. At  $\sim 920$  °C the formation of the metastable anatase TiO<sub>2</sub> becomes apparent, reaching a maximum quantity of  $10.7 \pm 0.8$  wt.% at  $\sim 1020$  °C. When further increasing the temperature, anatase is continuously transformed into the stable rutile modification. It can be assumed that the anatase phase is to a very small extent ( $< 1.5$  wt.%) already present at temperatures below 920 °C, which cannot unambiguously be identified in the XRDs or fitted using the sequential Rietveld Refinement. While some authors have

observed the occurrence of anatase during the oxidation of TiSiN coatings [9,23], to the best of our knowledge no detailed description of the quantitative phase composition as shown here has yet been published. However, attempts to explain the formation of anatase TiO<sub>2</sub> during oxidation of TiSiN have been made. The anatase phase has been reported to be stabilized at low temperatures when the grain size is below ~11 nm [23,34]. As proposed by Pilloud et al., grain coarsening during the oxidation of TiSiN is significantly reduced by the presence of the amorphous SiN<sub>x</sub> tissue phase surrounding the Ti(Si)N nanocrystallites. Thus, anatase can be observed upon the oxidation of TiSiN, but not for pure TiN coatings, where only rutile is formed [23]. The proposed explanations correlate well with the results of this work, where it is possible to observe the increase of the anatase phase fraction during the oxidation of TiSiN up to a temperature of ~1020 °C, where the critical grain size seems to be encountered, resulting in a continuous transformation of anatase into the stable rutile modification. Mège-Revil et al. monitored the grain size of TiSiN coatings during oxidation from room temperature to 1200 °C and reported a drastic increase in grain size from 6 to 30 nm between 900 and 1150 °C [35]. This correlates well with the decrease of the anatase phase fraction and transformation into the rutile phase above ~1020 °C observed in this study.

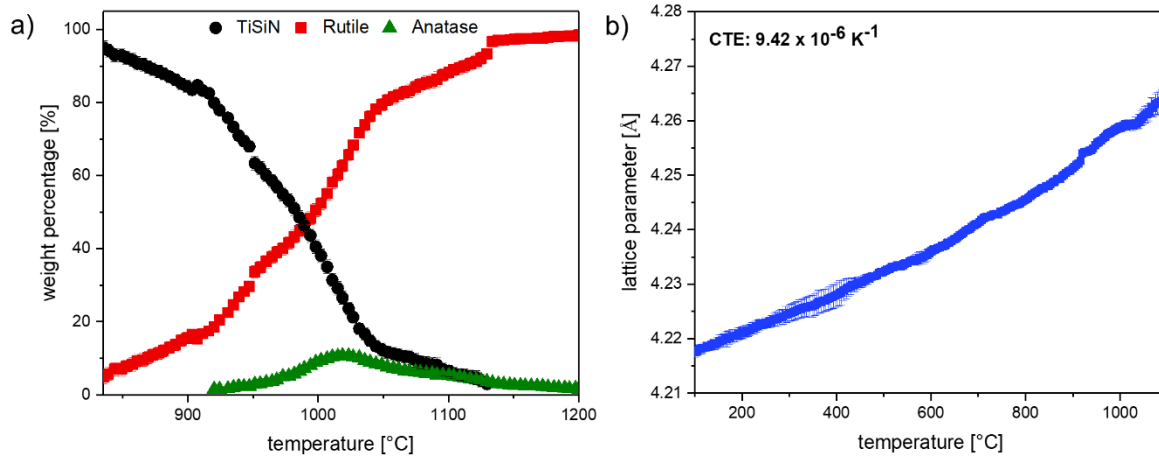


Fig. 3: Quantitative phase composition during the oxidation of powdered TiSiN in the temperature range between 830 and 1200 °C, obtained by sequential Rietveld refinement (a). Evolution of the lattice parameter of TiSiN during oxidation between 100 and 1100 °C, obtained by sequential Rietveld refinement. The coefficient of thermal expansion (CTE) was determined by a linear fit in a range of 100 to 800 °C (b).

A linear increase of the TiSiN lattice parameter before the onset of oxidation as a result of the thermal expansion is shown in Fig. 3(b). Slight deviations of the linear behavior above ~850 °C can be attributed to the formation of the rutile phase. As already observed in Fig. 1(a) at room temperature, the lattice parameter of ~4.22 Å at the starting temperature of 100 °C in Fig. 3(b) is still below the literature value of 4.24 Å for TiN, due to the reason that the silicon is also present in a solid solution besides the amorphous phase. Sperr et al. reported similarly decreased lattice parameters of 4.22 Å and 4.23 Å for TiSiN coatings at room temperature [16]. In order to determine the coefficient of thermal expansion (CTE) of the TiSiN powder, a linear fit of the lattice parameter evolution in a temperature range before the oxidation onset (between 100 and 800 °C) was made. The calculated value of  $9.42 \pm 0.05 \times 10^{-6} \text{ K}^{-1}$  is in excellent agreement with the literature CTE of  $9.41 \times 10^{-6} \text{ K}^{-1}$  that was determined for pure TiN between 100 and 800 °C using the formula presented by Saringer et al. [36].

As a final remark concerning the investigations of the powdered TiSiN coating via *in-situ* synchrotron XRD it should be noted that the kinetics during the oxidation process might slightly differ for the powder compared to a solid TiSiN coating, as the surface to volume ratio is higher for the powder sample. However, as the onset temperatures and phase evolution during oxidation mainly depend on the elemental composition and microstructure of the coating - which are not substantially altered during powder production - valid results can be presented in these regards for a powdered coating. Furthermore, in order to validate the results obtained for the powdered material for the equivalent solid coatings, coated single crystalline sapphire substrates were additionally oxidized within the scope of this study.

### 3.2 Oxidation of Solid Coating

Besides the detailed investigation of the temperature-dependent phase evolution during oxidation of a powdered TiSiN coating, the microstructural changes on a solid coating during oxidation were studied within this work. Thus, two TiSiN samples deposited on sapphire substrates were oxidized in ambient air at 930 and 1130 °C for 5 minutes, respectively. X-ray diffractograms of the oxidized coatings and the as-deposited coating on sapphire substrates are depicted in Fig. 4(a). At 930 °C, several small rutile peaks clearly show the ongoing oxidation of the TiSiN coating, however the most prominent peak in this diffractogram can still be assigned to TiN, meaning that the coating is not fully oxidized at this temperature. Furthermore, a small reflection of anatase at a d-spacing of 3.5 Å is visible, indicating the beginning formation of this metastable TiO<sub>2</sub> phase. These findings are in good agreement with the combined *in-situ* XRD and DSC investigations of the powdered TiSiN coating, where the anatase phase became apparent at ~920 °C in the phase-plot and a shoulder of the TiO<sub>2</sub> peak was visible in the DSC signal that can be related to the formation of anatase. Full oxidation of the crystalline Ti(Si)N phase can be observed after oxidation at 1130 °C, where a small anatase peak is

still visible besides the predominantly present rutile  $\text{TiO}_2$  phase. Again, these findings are consistent with the investigation of the powdered coating, where nearly full oxidation of  $\text{Ti}(\text{Si})\text{N}$  and the presence of small amounts of anatase at a temperature of  $1130\text{ }^\circ\text{C}$  were confirmed. Due to the excellent differentiation possible between the anatase and rutile  $\text{TiO}_2$  phase by Raman spectroscopy, additionally Raman spectra of the oxidized coatings were recorded which are shown in Fig. 4(b). A spectrum of the as-deposited  $\text{TiSiN}$  coating on cemented carbide is also added for comparison. Standard peak positions of  $\text{TiN}$ , anatase and rutile are indicated by symbols and vertical lines according to ref. [37,38]. As previously reported by other authors, anatase bands occur besides the rutile bands after oxidation of the  $\text{TiSiN}$  coatings at both temperatures [23,39]. While  $\text{TiN}$  bands can still be detected at  $930\text{ }^\circ\text{C}$ , full oxidation to rutile and anatase is observed in the Raman spectrum at  $1130\text{ }^\circ\text{C}$ , correlating well with XRD results. Consequently, it could be confirmed that the anatase phase occurs for both solid and powdered coatings.

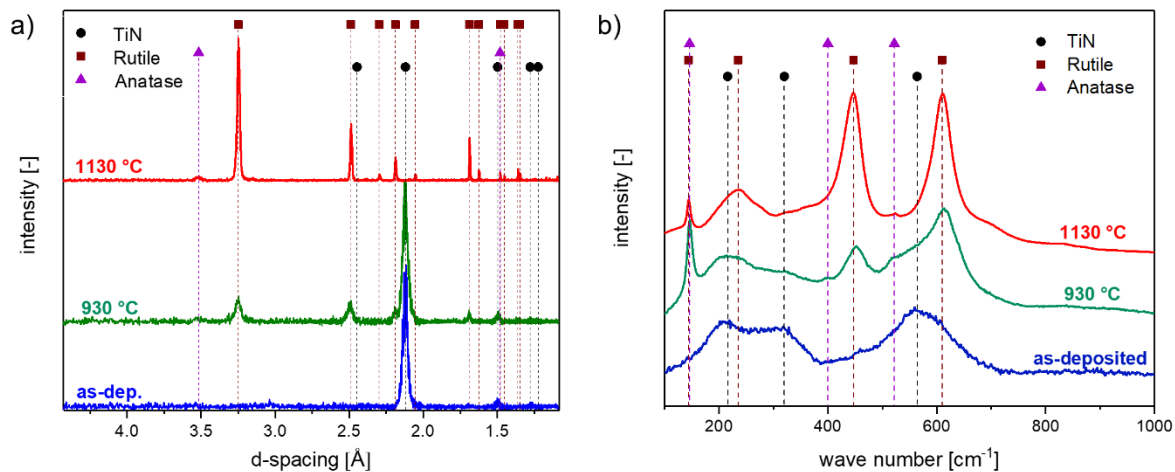


Fig. 4: X-ray diffractograms of the oxidized and the as-deposited  $\text{TiSiN}$  coatings on sapphire substrates (a). Raman spectra of the as-deposited  $\text{TiSiN}$  sample on cemented carbide and the oxidized  $\text{TiSiN}$  samples on sapphire substrates at  $930$  and  $1130\text{ }^\circ\text{C}$  (b).



As the oxidation of the  $\text{SiN}_x$  tissue phase cannot be monitored via XRD due to its amorphous structure, XPS measurements of the oxidized samples were conducted. The  $\text{Si}2p$  spectra for the TiSiN samples oxidized at 930 and 1130 °C are shown in Fig. 5(a) and (b), respectively. Binding energies according to literature [40–44] are indicated for amorphous  $\text{SiN}_x$ , Si-O-N and  $\text{SiO}_2$  by dashed lines. It can be observed that the position of the  $\text{Si}2p$  peaks after oxidation at both temperatures is close to the literature value of Si-O-N at 102.4 eV [42], meaning that the amorphous phase is not fully oxidized. Stoichiometric  $\text{SiO}_2$  would be expected to be found at higher binding energies than Si-O-N in a range of ~103.5 to 103.9 eV [42–44]. Furthermore, it is noticeable that no Ti-Si or Si-Si bonds are present within the sample, which would occur at ~98.6 eV [19]. The high-resolution XPS spectrum of  $\text{Ti}2p$  (not shown) for oxidation at 930 and 1130 °C exhibits peaks located at 464.2 eV ( $\text{Ti}2p_{1/2}$ ) and 458.5 eV ( $\text{Ti}2p_{3/2}$ ) that can be attributed to  $\text{TiO}_2$ ; no additional Ti-N bonding could be detected, indicating full oxidation of the TiN phase. However, it needs to be kept in mind that the information obtained from the XPS measurement is limited to the top ~10 nm of the sample. Observation of a Si-O-N phase but no stoichiometric  $\text{SiO}_2$  proves the enhanced oxidation resistance of the amorphous  $\text{SiN}_x$  phase compared to the TiN nanocrystals, which were already fully oxidized at 1130 °C, as evidenced by XRD and Raman investigations. Thus, the XPS results are in excellent agreement with the DSC measurements of the TiSiN powder, where the exothermic peak of the  $\text{TiO}_2$  formation was found at 1040 °C, while the peak most likely stemming from the Si-O-N formation could only be detected at higher temperatures of 1150 °C. This oxidation sequence was already reported by several other authors for  $\text{Si}_3\text{N}_4$ -TiN composite materials; they observed oxidation of the TiN phase between 600 and 1000 °C, followed by the oxidation of both phases – TiN and  $\text{Si}_3\text{N}_4$  – simultaneously at higher temperatures [45–47].

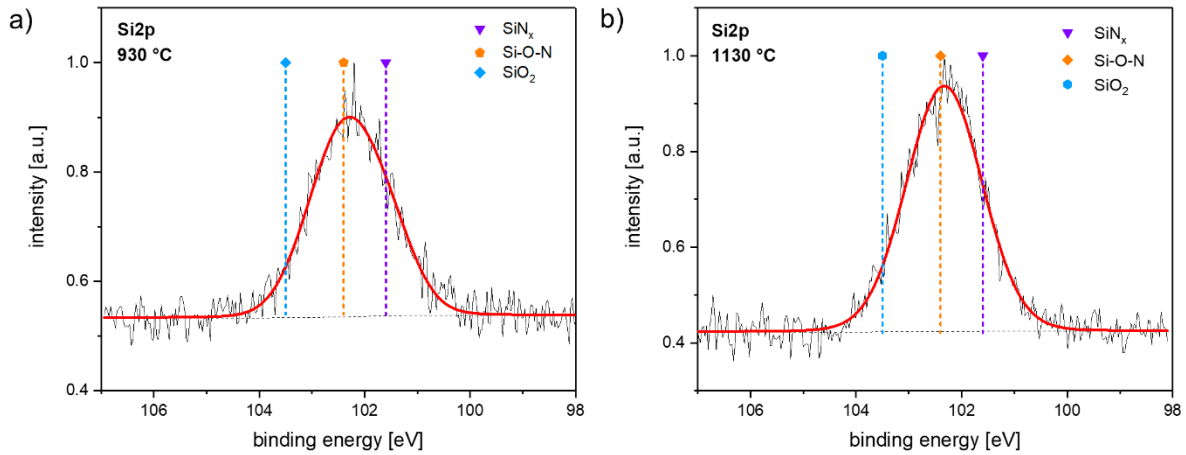


Fig. 5: X-ray photoelectron spectroscopy of the Si2p-orbital from the TiSiN coatings oxidized at 930 (a) and 1130 °C (b).

In order to gain further insight into the microstructure, phase and elemental composition of the oxidized coatings, HR-STEM investigations of the cross-sections were conducted. Images of the TiSiN coating oxidized at 930 °C are shown in Fig. 6. Fig. 6(a) reveals an oxidized layer of ~300 nm at the top region of the coating, meaning that at a temperature of 930 °C only a small part of the coating is oxidized, while the rest of the sample remains unaffected. This observation is in agreement with Raman and XRD measurements and further complies with kinetic studies of Mège-Revil et al. that reported a slow proceeding oxidation up to a temperature of ~900 °C, due to the amorphous SiN<sub>x</sub> phase reducing the oxygen diffusion within the coating [35]. The non-oxidized region in the TEM image shows a dense and feather-like structure that was already observed for the as-deposited TiSiN coating in Fig. 1(b). In Fig. 6(b) the oxidized area as well as the interface to the non-oxidized region are depicted including images of the elemental composition of this section. O is homogeneously distributed over the whole oxidized region. The increasing N intensity marks the beginning of the non-oxidized coating area. When taking a closer look at the Ti elemental map it becomes obvious that the top few nm of the sample surface are enriched in Ti, whereas this region is depleted in Si. It seems

that Ti diffuses to the surface during the oxidation process, which was already reported by Deschaux-Beaume et al., who observed the formation of a continuous  $\text{TiO}_2$  layer at the outer surface of their investigated  $\text{TiN-Si}_3\text{N}_4$  composite material during oxidation [48]. Furthermore, the elemental maps reveal irregularities in the distribution of Ti and Si within the rest of the oxidized region. This is even better visible in Fig. 6(c), showing the interface region between the oxidized and non-oxidized area, whereby the latter appears brighter in the HAADF (high-angle annular dark field). The elemental map clearly reveals Si-rich (green) and Ti-rich (blue) regions, which appear columnar. On the contrary to the oxidized region, the non-oxidized coating area exhibits a homogeneous distribution of Ti and Si. To further investigate the phase composition, the HR-STEM image of the oxidized area shown in Fig. 6(d) was taken. Similarly, to the as-deposited sample shown in Fig. 1(b), the coating still exhibits a partly crystalline and partly amorphous structure, meaning that either crystalline anatase or rutile  $\text{TiO}_2$  grains are surrounded by an amorphous Si-O-N phase.

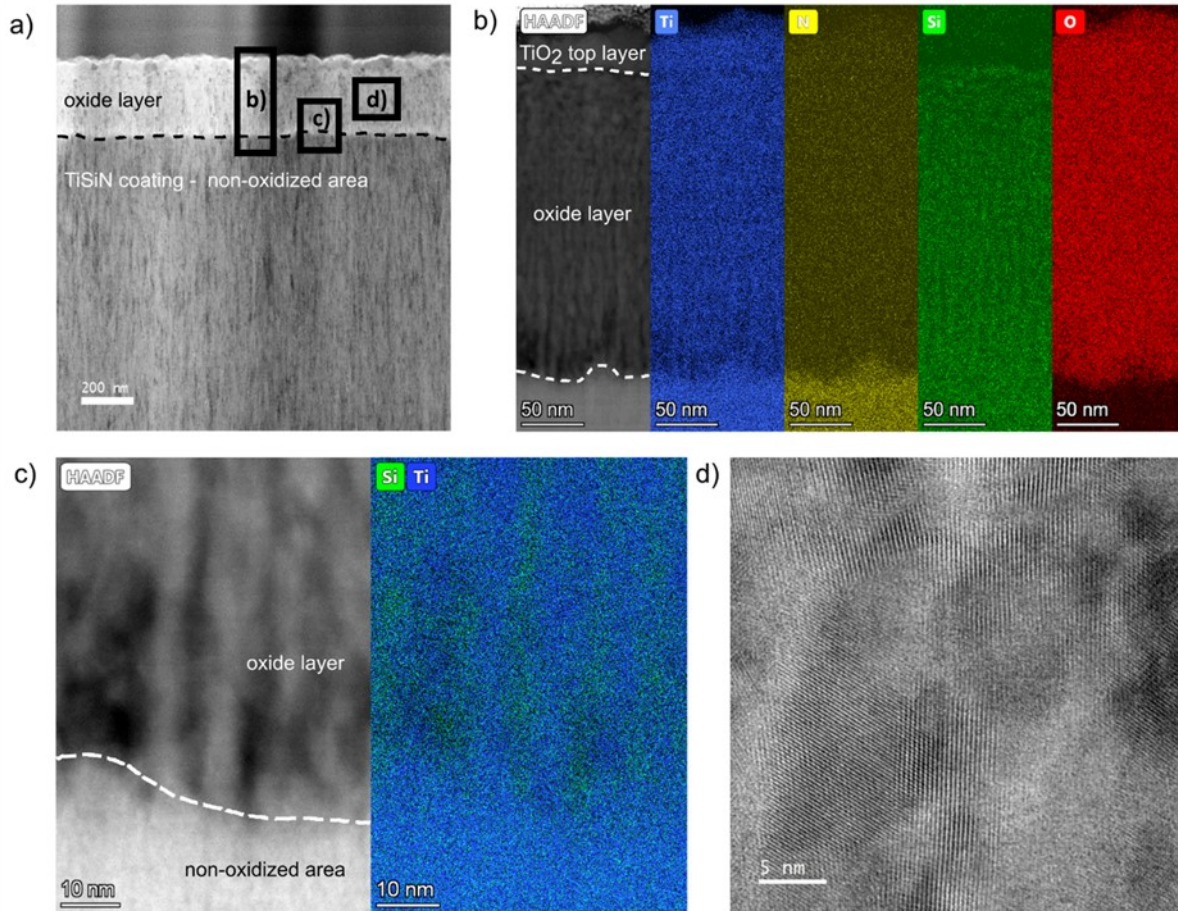


Fig. 6: ADF image showing the 300 nm thick oxide layer after oxidation of the TiSiN coating at 930 °C for 5 minutes. Regions, where the detailed images b), c) and d) are taken from are indicated (a). Elemental composition of the oxidized region including the interface to the non-oxidized area of the lamella (b). HAADF image and corresponding Ti and Si distribution of the oxidized region close to the interface to the non-oxidized region (c) and ADF image of the oxidized area showing amorphous and crystalline regions (d).

When oxidizing the coating at a temperature of 1130 °C for only five minutes a completely different microstructure can be found compared to oxidation at 930 °C. The HAADF image in Fig 7(a) shows that the entire coating is oxidized and significant grain coarsening has taken place, accompanied by a high porosity. This is again in agreement with the observations of Mège-Revil et al., who report an accelerated oxidation process for TiSiN at temperatures above ~900 °C as well as a significant increase in grain size from

6 to 30 nm between 900 and 1150 °C [35]. Fig. 7(a) further shows a TiO<sub>2</sub> top layer where barely any Si is present, which was also observed for the coating oxidized at 930 °C, due to diffusion of Ti to the surface. However, the coating oxidized at 1130 °C clearly shows a gradient in the Ti content, where the Ti content increases from the substrate/coating interface towards the coating surface. In the surface near region below the TiO<sub>2</sub> top layer as well as close to the substrate interface high porosity of the coating can be observed. On the contrary, there are hardly any larger pores visible in the mid-region of the lamella, where coarsened TiO<sub>2</sub> grains are surrounded by amorphous Si-O-N. In order to take a closer look at the phase composition of the coating oxidized at 1130 °C the HR-STEM image shown in Fig. 7(b) was taken. Similarly, to the as-deposited coating and the coating oxidized at 930 °C, amorphous and crystalline regions can be observed. In order to assign the crystalline grains to rutile or anatase TiO<sub>2</sub>, the d-spacing was determined via FFT (shown exemplarily in Fig. 7(c) for the rutile grain and one anatase grain) and IFFT and compared to literature values for both TiO<sub>2</sub> modifications [49]. The highest difference in the d-spacing can be found for the (101) reflection of anatase and the (110) reflection of rutile, which show a d-spacing according to literature of 3.52 or 3.25 Å, respectively [49]. The (110) reflection of the grain assigned to rutile depicted in Fig. 7(b) exhibited a d-spacing of 3.32 Å, while the (101) reflection of the two anatase grains showed a d-spacing of 3.54 Å or 3.57 Å, close to respective literature values. Thus, it could be shown that the anatase phase can not only be observed in the Raman and XRD investigations, but even individual anatase grains can be assigned using HR-STEM.

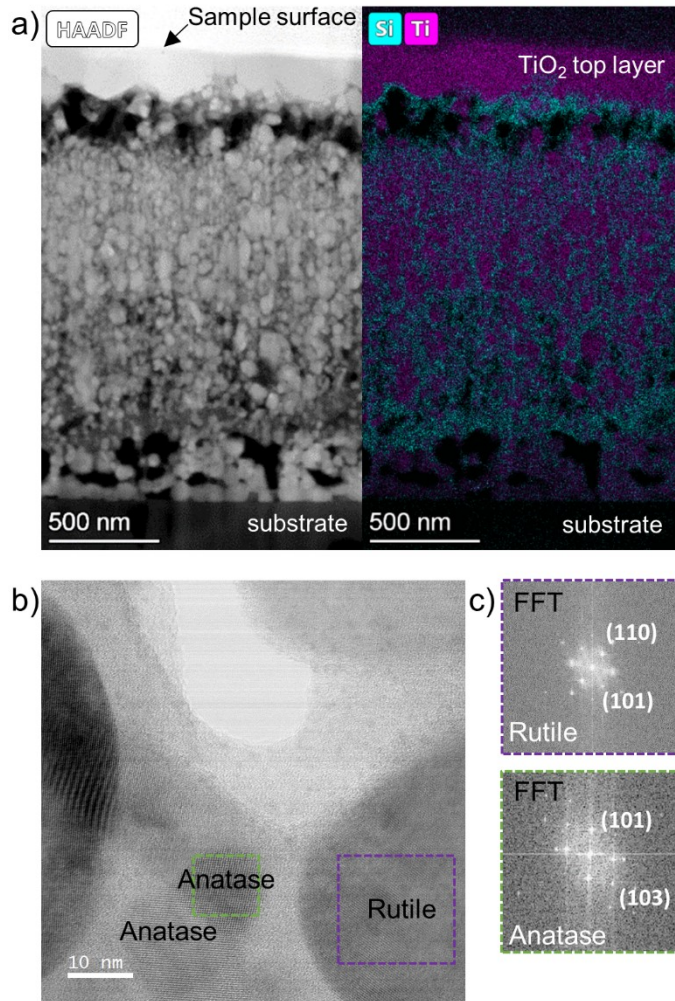


Fig. 7: HAADF image and elemental composition of the TiSiN coating oxidized at 1130 °C for 5 minutes (a). ADF image showing grains assigned to anatase and rutile TiO<sub>2</sub> surrounded by an amorphous Si-O-N phase (b). FFT images of the rutile and one anatase grain shown in image b) (purple and green highlighted areas) (c).

#### 4. Conclusion

Within this work, the temperature-dependent phase composition of a powdered TiSiN coating during oxidation as well as the microstructure and elemental composition of the corresponding solid oxidized TiSiN coating were investigated in detail. *In-situ* synchrotron X-ray diffraction experiments revealed a high oxidation stability of the TiSiN powder up to ~830 °C, followed by the formation of both anatase and rutile TiO<sub>2</sub>. The

quantity of the metastable anatase phase was shown to reach a maximum at a temperature of  $\sim 1020$  °C above which it continuously transformed into the stable rutile modification, as a result of the grain coarsening and increasing temperature. X-ray diffractograms and Raman spectra of solid TiSiN coatings oxidized at two different temperatures (930 and 1130 °C) for 5 minutes confirmed the presence of anatase TiO<sub>2</sub> besides the predominantly present rutile phase. Differential scanning calorimetry measurements of the powdered sample as well as XPS investigations of the solid coatings further provided information on the X-ray amorphous SiN<sub>x</sub> phase, revealing the retarded oxidation of this phase compared to the nanocrystalline Ti(Si)N grains. HR-STEM investigations additionally allowed to study the microstructure and elemental composition of the coatings after oxidation at 930 and 1130 °C. While only a thin oxide layer of  $\sim 300$  nm was formed at 930 °C, full oxidation of the crystalline Ti(Si)N phase to TiO<sub>2</sub> took place at 1130 °C, accompanied by high porosity and significant grain coarsening. Oxidation at both temperatures led to formation of a TiO<sub>2</sub> top-layer due to diffusion of Ti to the surface-near region. Furthermore, a phase structure consisting of crystalline TiO<sub>2</sub> surrounded by an amorphous Si-O-N phase was observed upon oxidation of TiSiN coatings. The present work not only confirms the outstanding oxidation resistance of TiSiN coatings, but also establishes a profound understanding of the oxidation sequence and microstructure of this coating system.

## 5. Acknowledgments

The authors want to thank DI Alexander Fian (Materials - Joanneum Research) for XPS investigations. We acknowledge DESY (Hamburg, Germany), a member of the Helmholtz Association HGF, for the provision of experimental facilities. Parts of this research were carried out at PETRA III using the high energy materials science beamline P07 (proposal no.: I-20180959 EC). The research leading to this result has been supported by the project CALIPSOplus under the Grant Agreement 730872 from the EU Framework Programme for Research and Innovation HORIZON 2020. The financial support by the

Austrian Federal Ministry for Digital and Economic Affairs and the National Foundation for Research, Technology and Development is gratefully acknowledged.

## 6. References

- [1] P. Hedenqvist, M. Olsson, P. Wallén, Å. Kassman, S. Hogmark, S. Jacobson, How TiN coatings improve the performance of high speed steel cutting tools, *Surf. Coatings Technol.* 41 (1990) 243–256.
- [2] A. Matthews, Titanium nitride PVD coating technology, *Surf. Eng.* 1 (1985) 93–104.
- [3] M. V. Kowstubhan, P.K. Philip, On the tool-life equation of TiN-coated high speed steel tools, *Wear.* 143 (1991) 267–275.
- [4] G. Spur, G. Byrne, B. Bienia, The performance of high speed steel indexable inserts coated by physical vapour deposition in the milling of ductile materials, *Surf. Coatings Technol.* 43–44 (1990) 1074–1085.
- [5] K.R. Wu, R.G. Bayer, P.A. Engel, D.C. Sun, Wear of physical vapor deposition TiN coatings sliding against Cr-steel and WC counterbodies, *J. Tribol.* 120 (1998) 482–488.
- [6] J.E. Sundgren, Structure and properties of TiN coatings, *Thin Solid Films.* 128 (1985) 21–44.
- [7] W. Münz, Titanium aluminum nitride films: A new alternative to TiN coatings, *J. Vac. Sci. Technol. A Vacuum, Surfaces, Film.* 4 (1986) 2717–2725.
- [8] M. Diserens, J. Patscheider, F. Lévy, Mechanical properties and oxidation resistance of nanocomposite TiN-SiN<sub>x</sub> physical-vapor-deposited thin films, *Surf. Coatings Technol.* 120–121 (1999) 158–165.
- [9] P. Steyer, D. Pilloud, J.F. Pierson, J.P. Millet, M. Charnay, B. Stauder, P. Jacquot, Oxidation resistance improvement of arc-evaporated TiN hard coatings by silicon addition, *Surf. Coatings Technol.* 201 (2006) 4158–4162.
- [10] S. Vepřek, S. Reiprich, A concept for the design of novel superhard coatings, *Thin Solid Films.* 268 (1995) 64–71.



- [11] S. Vepřek, The search for novel, superhard materials, *J. Vac. Sci. Technol. A Vacuum, Surfaces, Film.* 17 (1999) 2401–2420.
- [12] F. Pei, Y.X. Xu, L. Chen, Y. Du, H.K. Zou, Structure, mechanical properties and thermal stability of  $Ti_{1-x}Si_xN$  coatings, *Ceram. Int.* 44 (2018) 15503–15508.
- [13] M. Nose, Y. Deguchi, T. Mae, E. Honbo, T. Nagae, K. Nogi, Influence of sputtering conditions on the structure and properties of Ti-Si-N thin films prepared by r.f.-reactive sputtering, *Surf. Coatings Technol.* 174–175 (2003) 261–265.
- [14] L. Rebouta, C.J. Tavares, R. Aimo, Z. Wang, K. Pischow, E. Alves, T.C. Rojas, J.A. Odriozola, Hard nanocomposite Ti-Si-N coatings prepared by DC reactive magnetron sputtering, *Surf. Coatings Technol.* 133–134 (2000) 234–239.
- [15] P. Zhang, Z. Cai, W. Xiong, Influence of Si content and growth condition on the microstructure and mechanical properties of Ti-Si-N nanocomposite films, *Surf. Coatings Technol.* 201 (2007) 6819–6823.
- [16] M. Sperr, Z.L. Zhang, Y.P. Ivanov, P.H. Mayrhofer, M. Bartosik, Correlating elemental distribution with mechanical properties of  $TiN/SiN_x$  nanocomposite coatings, *Scr. Mater.* 170 (2019) 20–23.
- [17] C.L. Chang, C. Te Lin, P.C. Tsai, W.Y. Ho, W.J. Liu, D.Y. Wang, Mechanical and corrosion properties of (Ti,Si)N coating synthesized by cathodic arc plasma evaporation, *Surf. Coatings Technol.* 202 (2008) 5516–5520.
- [18] G. Greczynski, J. Patscheider, J. Lu, B. Alling, A. Ektarawong, J. Jensen, I. Petrov, J.E. Greene, L. Hultman, Control of  $Ti_{1-x}Si_xN$  nanostructure via tunable metal-ion momentum transfer during HIPIMS/DCMS co-deposition, *Surf. Coatings Technol.* 280 (2015) 174–184.
- [19] J.Q. Zhu, M.P. Johansson-Jöesaar, P. Polcik, J. Jensen, G. Greczynski, L. Hultman, M. Odén, Influence of Ti-Si cathode grain size on the cathodic arc process and resulting Ti-Si-N coatings, *Surf. Coatings Technol.* 235 (2013) 637–647.
- [20] C.L. Chang, C. Te Lin, P.C. Tsai, W.Y. Ho, D.Y. Wang, Influence of bias voltages on

- the structure and wear properties of TiSiN coating synthesized by cathodic arc plasma evaporation, *Thin Solid Films*. 516 (2008) 5324–5329.
- [21] S. Vepřek, Conventional and new approaches towards the design of novel superhard materials, *Surf. Coatings Technol.* 97 (1997) 15–22.
- [22] F. Vaz, L. Rebouta, P. Goudeau, J. Pacaud, H. Garem, J.. Rivière, A. Cavaleiro, E. Alves, Characterisation of  $Ti_{1-x}Si_xN_y$  nanocomposite films, *Surf. Coatings Technol.* 133–134 (2000) 307–313.
- [23] D. Pilloud, J.F. Pierson, M.C. Marco de Lucas, A. Cavaleiro, Study of the structural changes induced by air oxidation in Ti-Si-N hard coatings, *Surf. Coatings Technol.* 202 (2008) 2413–2417.
- [24] N. Schell, A. King, F. Beckmann, T. Fischer, M. Müller, A. Schreyer, The high energy materials science beamline (HEMS) at PETRA III, *Mater. Sci. Forum*. 772 (2014) 57–61.
- [25] C. Saringer, M. Tkadletz, A. Stark, N. Schell, C. Czettl, N. Schalk, In-situ investigation of the oxidation behavior of metastable CVD- $Ti_{1-x}Al_xN$  using a novel combination of synchrotron radiation XRD and DSC, *Surf. Coatings Technol.* 374 (2019) 617–624.
- [26] M. Basham, J. Filik, M.T. Wharmby, P.C.Y. Chang, B. El Kassaby, M. Gerring, J. Aishima, K. Levik, B.C.A. Pulford, I. Sikharulidze, D. Sneddon, M. Webber, S.S. Dhesi, F. Maccherozzi, O. Svensson, S. Brockhauser, G. Náray, A.W. Ashton, Data Analysis Workbench (DAWN), *J. Synchrotron Radiat.* 22 (2015) 853–858.
- [27] J. Filik, A.W. Ashton, P.C.Y. Chang, P.A. Chater, S.J. Day, M. Drakopoulos, M.W. Gerring, M.L. Hart, O. V. Magdysyuk, S. Michalik, A. Smith, C.C. Tang, N.J. Terrill, M.T. Wharmby, H. Wilhelm, Processing two-dimensional X-ray diffraction and small-angle scattering data in DAWN 2, *J. Appl. Crystallogr.* 50 (2017) 959–966.
- [28] THE CERTIFICATION OF STANDARD REFERENCE MATERIAL 660C FOR POWDER DIFFRACTION | NIST, (n.d.).

- <https://www.nist.gov/publications/certification-standard-reference-material-660c-powder-diffraction> (accessed June 25, 2020).
- [29] Crystallography Open Database, (n.d.). <http://www.crystallography.net/cod/> (accessed April 8, 2020).
- [30] A. Flink, M. Beckers, J. Sjölen, T. Larsson, S. Braun, L. Karlsson, L. Hultman, The location and effects of Si in  $(\text{Ti}_{1-x}\text{Si}_x)\text{N}_y$  thin films, *J. Mater. Res.* 24 (2009) 2483–2498.
- [31] A. Flink, T. Larsson, J. Sjölen, L. Karlsson, L. Hultman, Influence of Si on the microstructure of arc evaporated  $(\text{Ti,Si})\text{N}$  thin films; evidence for cubic solid solutions and their thermal stability, *Surf. Coatings Technol.* 200 (2005) 1535–1542.
- [32] M.S. Ahmed, X. Zhao, Z. Zhou, P. Munroe, N. Chen-Tan, L. Kwok, Y. Li, Z. Xie, Effect of thermal annealing upon residual stress and mechanical properties of nanostructured TiSiN coatings on steel substrates, *J. Am. Ceram. Soc.* 94 (2011) 1546–1551.
- [33] A.O. Eriksson, O. Tengstrand, J. Lu, J. Jensen, P. Eklund, J. Rosén, I. Petrov, J.E. Greene, L. Hultman, Si incorporation in  $\text{Ti}_{1-x}\text{Si}_x\text{N}$  films grown on TiN (001) and (001)-faceted TiN (111) columns, *Surf. Coatings Technol.* 257 (2014) 121–128.
- [34] Y. Hu, H.L. Tsai, C.L. Huang, Effect of brookite phase on the anatase-rutile transition in titania nanoparticles, *J. Eur. Ceram. Soc.* 23 (2003) 691–696.
- [35] A. Mège-Revil, P. Steyer, G. Thollet, R. Chiriack, C. Sigala, J.C. Sánchez-López, C. Esnouf, Thermogravimetric and in situ SEM characterisation of the oxidation phenomena of protective nanocomposite nitride films deposited on steel, *Surf. Coatings Technol.* 204 (2009) 893–901.
- [36] C. Saringer, C. Kicking, F. Munnik, C. Mitterer, N. Schalk, M. Tkadletz, Thermal expansion of magnetron sputtered  $\text{TiC}_x\text{N}_{1-x}$  coatings studied by high-temperature X-ray diffraction, *Thin Solid Films.* 688 (2019) 137307.
- [37] L. Kernazhitsky, V. Shymanovska, T. Gavrilko, V. Naumov, L. Fedorenko, V. Kshnyakin, J. Baran, Laser-excited excitonic luminescence of nanocrystalline  $\text{TiO}_2$

- powder, *Ukr. J. Phys.* 59 (2014) 246–253.
- [38] N. Saoula, S. Djerourou, K. Yahiaoui, K. Henda, R. Kesri, R.M. Erasmus, J.D. Comins, Study of the deposition of Ti/TiN multilayers by magnetron sputtering, *Surf. Interface Anal.* 42 (2010) 1176–1179.
- [39] B. Deng, Y. Tao, X. Zhu, H. Qin, The oxidation behavior and tribological properties of Si-implanted TiN coating, *Vacuum.* 99 (2014) 216–224.
- [40] I. Bertóti, Characterization of nitride coatings by XPS, *Surf. Coatings Technol.* 151–152 (2002) 194–203.
- [41] J. Procházka, P. Karvánková, M.G.J. Vepřek-Heijman, S. Vepřek, Conditions required for achieving superhardness of  $\geq 45$  GPa in nc-TiN/a-Si<sub>3</sub>N<sub>4</sub> nanocomposites, *Mater. Sci. Eng. A.* 384 (2004) 102–116.
- [42] J. Finster, E.D. Klinkenberg, J. Heeg, W. Braun, ESCA and SEXAFS investigations of insulating materials for ULSI microelectronics, *Vacuum.* 41 (1990) 1586–1589.
- [43] N. Jehanathan, Y. Liu, B. Walmsley, J. Dell, M. Saunders, Effect of oxidation on the chemical bonding structure of PECVD SiN<sub>x</sub> thin films, *J. Appl. Phys.* 100 (2006) 123516.
- [44] A. Chainani, S.K. Nema, P. Kikani, P.I. John, Electronic structure of carbon-free silicon oxynitride films grown using an organic precursor hexamethyl-disilazane, *J. Phys. D. Appl. Phys.* 35 (2002) L44–L47.
- [45] A. Bellosi, A. Tampieri, Y. Liu, Oxidation behaviour of electroconductive Si<sub>3</sub>N<sub>4</sub>-TiN composites, *Mater. Sci. Eng. A.* 127 (1990) 115–122.
- [46] Y.G. Gogotsi, F. Porz, The oxidation of particulate-reinforced Si<sub>3</sub>N<sub>4</sub>-TiN composites, *Corros. Sci.* 33 (1992) 627–640.
- [47] Y.G. Gogotsi, F. Porz, G. Dransfield, Oxidation behavior of monolithic TiN and TiN dispersed in ceramic matrices, *Oxid. Met.* 39 (1993) 69–91.
- [48] F. Deschaux-Beaume, T. Cutard, N. Frèty, C. Levailant, Oxidation of a silicon nitride–titanium nitride composite: microstructural investigations and

phenomenological modeling, *J. Am. Ceram. Soc.* 85 (2002) 1860–1866.

- [49] D. Pathinettam Padiyan, D. Henry Raja, Synthesis of various generations titania nanotube arrays by electrochemical anodization for H<sub>2</sub> production, *Energy Procedia*. 22 (2012) 88–100.

# Publication III

**Oxidation mechanism of sputter deposited model SiN<sub>x</sub>/TiN/SiN<sub>x</sub> coatings**

Yvonne Moritz, Christina Kainz, Paul Peritsch, Christian Mitterer, Nina Schalk

**Under review in Surface & Coatings Technology (2023)**

## Oxidation mechanism of sputter deposited model $\text{SiN}_x/\text{TiN}/\text{SiN}_x$ coatings

Yvonne Moritz<sup>a</sup>, Christina Kainz<sup>a</sup>, Paul Peritsch<sup>a</sup>, Christian Mitterer<sup>b</sup>, Nina Schalk<sup>a</sup>

<sup>a</sup> Christian Doppler Laboratory for Advanced Coated Cutting Tools at the Department of Materials Science, Montanuniversität Leoben, Franz–Josef–Strasse 18, 8700 Leoben, Austria

<sup>b</sup> Department of Materials Science, Montanuniversität Leoben, Franz–Josef–Strasse 18, 8700 Leoben, Austria

### Abstract

TiSiN coatings are of high interest for the cutting industry, since they not only offer excellent mechanical properties, but also exhibit exceptional oxidation resistance. Although up to date several studies have been conducted on evaluating the oxidation resistance of TiSiN coatings, the exact oxidation sequence of nanocomposite coatings consisting of crystalline TiN grains embedded within an amorphous  $\text{SiN}_x$  phase remains unclear. Therefore, the aim of this work is to provide a detailed insight into the oxidation of such nanocomposites using a three-layer  $\text{SiN}_x/\text{TiN}/\text{SiN}_x$  model system. Three different  $\text{SiN}_x$  layer thicknesses of 150, 300 and 800 nm were investigated, while the TiN layer thickness was with 900 nm identical for all coatings. The results revealed that the amorphous  $\text{SiN}_x$  efficiently shields TiN against oxidation up to temperatures exceeding 800 °C, whereby the exact oxidation onset temperature increased with increasing  $\text{SiN}_x$  layer thickness. After reaching a critical temperature, both the TiN and amorphous  $\text{SiN}_x$  phase were found to exhibit a porous structure, leading to oxidation of the TiN layer and growth of coarsened  $\text{TiO}_2$  grains, which eventually break the  $\text{SiN}_x$  top layer. Furthermore,

amorphous SiN<sub>x</sub> was shown to be significantly more resistant to oxidation compared to crystalline TiN, being still mainly non-oxidized after oxidation at 1200 °C for 30 min. The present study allows to gain insight into the underlying mechanisms of the shielding effect of amorphous SiN<sub>x</sub> on TiN, thus providing a deeper understanding of the oxidation behavior of TiSiN nanocomposite coatings.

**Keywords:** TiSiN, nanocomposite, oxidation stability, sputter deposition

## 1. Introduction

Throughout the last decades, considerable effort has been devoted to developing new protective coating materials for cutting tools with enhanced mechanical properties and thermal stability in order to meet the increasing demands in the cutting industry. Starting with the commonly used binary TiN coating system, the need for coatings with hardness values above ~20 GPa and an oxidation stability higher than ~550 °C have soon led to the development of ternary TiAlN hard coatings [1]. Addition of Al to TiN has shown to improve the hardness significantly, which – depending on the Al content and deposition conditions – can reach up to ~35 GPa [2,3]. Furthermore, TiAlN was found to outperform the oxidation resistance of TiN coatings by ~100-250 °C [1,4]. In the following years, the impact of additional elements such as C, Si or B on the properties of TiN has been evaluated [5–9]. Among these, especially TiSiN hard coatings have proven to exhibit favorable properties for the cutting industry.

The microstructure of TiSiN coatings is frequently described as nanocomposite, consisting of nanocrystalline TiN (nc-TiN) grains embedded in an amorphous SiN<sub>x</sub> tissue phase. Since the amorphous SiN<sub>x</sub> phase hinders grain growth and grain boundary sliding, exceptionally high hardness values of more than 40 GPa can be achieved [9–11]. Furthermore, the presence of the amorphous SiN<sub>x</sub> tissue phase has been found to significantly improve the thermal stability of TiSiN coatings up to ~1300 °C due to



retarded grain coarsening [11]. Additionally, the oxidation resistance of TiSiN is considerably enhanced compared to binary TiN coatings, since the amorphous SiN<sub>x</sub> phase prevents oxygen diffusion at the grain boundaries [12–14]. The oxidation mechanism of TiSiN coatings has been studied by several researchers. Steyer et al. discovered the occurrence of anatase TiO<sub>2</sub> (a-TiO<sub>2</sub>) besides the stable rutile TiO<sub>2</sub> (r-TiO<sub>2</sub>) modification when oxidizing arc evaporated TiSiN hard coatings [13]. This phenomenon was suggested to occur due to the presence of the amorphous SiN<sub>x</sub> phase, which leads to retarded grain coarsening during oxidation. Thus, the occurrence of a-TiO<sub>2</sub> is fostered, which is known to be stabilized at grain sizes below 11 nm [13,14]. Furthermore, investigations on the temperature-dependent phase composition of arc evaporated TiSiN upon oxidation revealed the simultaneous formation of both, r-TiO<sub>2</sub> and a-TiO<sub>2</sub>, however, only up to a temperature of approximately 1020 °C. As the temperature further increases, a-TiO<sub>2</sub> transforms into the r-TiO<sub>2</sub> modification due to reaching the critical grain size [15].

Other researchers concentrated their investigations on the influence of the respective Si content on the oxidation stability of TiSiN hard coatings. Here, Arab Pour Yazdi et al. and Pilloud et al. reported on an increasing oxidation stability with Si content increasing from 0 to 9 at.%. The authors attributed this finding to a potentially more effective shielding of the nc-TiN grains by amorphous SiN<sub>x</sub> with a higher Si content [14,16]. Wu et al., however, evaluated the oxidation resistance of TiAlSiN coatings and only found an increase of the oxidation stability up to a Si content of 8 at.% and a deterioration above this value. This observation was attributed to potential agglomeration of the SiN<sub>x</sub> phase, meaning the formation of SiN<sub>x</sub> clusters and thus no more efficient shielding of the individual Ti(Al,Si)N grains, as the Si content becomes too high [17].

Since the favorable fraction of the amorphous SiN<sub>x</sub> phase within Ti(Al)SiN coatings for an optimized oxidation resistance is controversially discussed in literature, the aim of this work was to establish a fundamental understanding of the shielding effect of the SiN<sub>x</sub> phase upon oxidation with a model system using SiN<sub>x</sub> and TiN. Therefore, several three-

layer coatings with the architecture  $\text{SiN}_x/\text{TiN}/\text{SiN}_x$  were deposited by unbalanced magnetron sputtering, where the thickness of the  $\text{SiN}_x$  layers was varied between 150, 300 and 800 nm, while the TiN layer thickness was kept constant at 900 nm for all coatings. The influence of the  $\text{SiN}_x$  layer thickness on the oxidation stability of the TiN layer as well as the oxidation sequence was studied by oxidizing the three-layer coatings in a furnace at varying temperatures. Subsequently, the oxidized coatings were analyzed using a combination of several characterization techniques such as X-ray diffraction (XRD), Raman spectroscopy and scanning electron microscopy (SEM).

## 2. Experimental Methods

The three-layer  $\text{SiN}_x/\text{TiN}/\text{SiN}_x$  coatings investigated in this work were deposited by unbalanced magnetron sputtering on a lab-scale magnetron sputter device. Powder metallurgically prepared Ti and Si targets with diameters of 51 mm purchased from Lesker with a purity no less than 99.7 % were used. (0001) oriented sapphire with a geometry of  $10 \times 10 \times 0.5 \text{ mm}^3$  served as substrates, which were ultrasonically cleaned in ethanol prior to the deposition process and subsequently mounted on a rotating substrate holder. Then, the vacuum chamber was heated to  $700 \text{ }^\circ\text{C}$  and evacuated to a base pressure of  $9.6 \times 10^{-2} \text{ mbar}$ . The substrates were again cleaned by  $\text{Ar}^+$  ion bombardment for  $\sim 10 \text{ min}$  in order to remove surface impurities by applying an Ar flow of 200 sccm at a total pressure of 0.1 mbar, a target current of 0.1 A and a bias voltage of -500 V. Three coatings were synthesized, each in a three-layer  $\text{SiN}_x/\text{TiN}/\text{SiN}_x$  structure. All  $\text{SiN}_x$  and TiN layers were deposited at  $700 \text{ }^\circ\text{C}$ , using gas flows of 30 sccm and 5 sccm for  $\text{N}_2$  and Ar, respectively, resulting in a total pressure of  $3 \times 10^{-3} \text{ mbar}$ . A target current of 0.15 A but no bias voltage (i.e. floating potential) was applied for the deposition of the  $\text{SiN}_x$  layers, while a higher current of 0.35 A and a bias voltage of -100 V was used for the TiN layers. The deposition time of the TiN layer was kept constant at 80 min for all three coatings resulting in a layer thickness of  $\sim 900 \text{ nm}$ , while the deposition time for the  $\text{SiN}_x$  layers was varied between 25, 50 and 125 min to obtain different layer thicknesses. The coatings were

oxidized in a Nabertherm N11/HR furnace in air at varying temperatures between 800 and 1500 °C for 30 min and allowed to cool down to room temperature outside the furnace.

In order to characterize the microstructure of the as-deposited and the oxidized coatings, XRD measurements were carried out on a Bruker D8 Advance X-ray diffractometer with an energy dispersive Sol-X detector using Cu-K $\alpha$  radiation ( $\lambda = 1.5406 \text{ \AA}$ ). Measurements were conducted in grazing incidence geometry, applying an incidence angle of 2°. The  $2\theta$ -scans were recorded with a step size of 0.02° and a measurement time of 1 s per step. Furthermore, SEM investigations were carried out and images of the cross-sections were acquired using a Zeiss EVO MA25 microscope. For more detailed insights into the microstructure and elemental composition, the coating with a SiN $_x$  layer thickness of 300 nm was additionally investigated in the as-deposited state and after oxidation at 1200 °C by SEM using a ZEISS Gemini SEM450. Prior to the SEM analysis, the cross-sections were prepared utilizing a Hitachi IM4000+ ion milling system with Ar $^+$  ions. The surface of the oxidized samples was further analyzed using a light optical microscope by Reichert-Jung Polyvar Met.

Raman spectroscopy measurements of coatings in the as-deposited state were performed with a LabRam HR800 device from Jobin Yvon employing a frequency-doubled Nd-YAG laser with a wavelength of 532 nm. Raman spectra of the oxidized coatings were acquired using a WiTec alpha300R confocal Raman microscope, which is equipped with a diode pumped solid state laser exhibiting also a wavelength of 532 nm. The power of the laser at the sample surface was set at 10 mW. The Raman spectra of both the as-deposited and oxidized coatings were recorded between 100 and 1500 cm $^{-1}$ .

### 3. Results and Discussion

The cross-sections of the three SiN<sub>x</sub>/TiN/SiN<sub>x</sub> coatings deposited with deposition times of 25, 50 and 125 min for the SiN<sub>x</sub> layers were analyzed by SEM and the respective micrographs are shown in Fig. 1. It can be observed that the layer thickness of the SiN<sub>x</sub> layers – as intended – gradually increased with increasing deposition time. While the thickness of the TiN layer was found to be approximately constant at 900 nm for all three coatings, the thickness of the SiN<sub>x</sub> layers varied between ~150 nm (Fig. 1a), ~300 nm (Fig. 1b) and ~800 nm (Fig. 1c). Regardless of the SiN<sub>x</sub> layer thickness, the TiN layer exhibits small columnar grains, while the SiN<sub>x</sub> layers appear to be featureless, indicating their amorphous nature. Söderberg et al. attempted to reach an epitaxial stabilization of cubic-SiN<sub>x</sub> in TiN/SiN<sub>x</sub> multilayers using reactive dual magnetron sputtering. The authors observed a transition from epitaxially stabilized crystalline SiN<sub>x</sub> to an amorphous structure once the layer thickness was increased from 0.3 to 0.8 nm [18]. Thus, the amorphous structure of the SiN<sub>x</sub> layers found in our study is in accordance with Söderberg's observations, since the layer thicknesses are significantly higher.

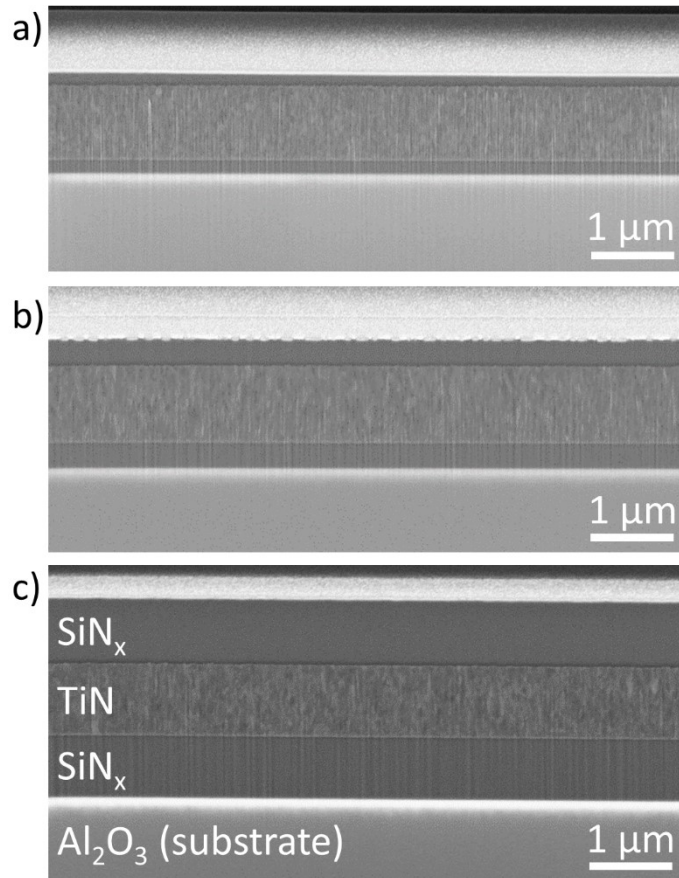


Fig. 1: Secondary electron SEM cross-section micrographs revealing the three-layer  $\text{SiN}_x/\text{TiN}/\text{SiN}_x$  architecture for varying  $\text{SiN}_x$  layer thicknesses of a) 150 nm, b) 300 nm and c) 800 nm.

In order to take a closer look at the elemental distribution in the coatings, elemental maps of Ti, Si and N were recorded and are depicted exemplarily for the coating with a  $\text{SiN}_x$  layer thickness of 300 nm in Fig. 2a. EDX maps of Ti and Si reveal a sharp interface between the individual  $\text{SiN}_x/\text{TiN}/\text{SiN}_x$  layers, where Si is exclusively present in the  $\text{SiN}_x$  layers and no diffusion into the TiN layer has taken place. N is present in all layers, however, the N intensity appears to be significantly stronger in the TiN layer compared to the  $\text{SiN}_x$  layers. In order to quantify the respective elemental composition, an additional EDX line scan starting from the substrate to the coating surface was performed, which is depicted in Fig. 2b. At a scanning distance of  $\sim 1.8 - 2.4 \mu\text{m}$ , the chemical composition of

the TiN layer is visible. The elemental composition of this layer was found to amount to 51 at.% Ti, 46 at.% N and 3 at.% O, indicating a slightly understoichiometric composition with respect to N. However, it needs to be kept in mind that the precise differentiation between N and Ti by EDX measurements is limited due to peak overlaps of N with the orbital lines of Ti [19]. Oxygen impurities of 3 at.% are in accordance with literature values ranging between 1 and 5 at.% of oxygen for sputter-deposited nitride hard coatings [20,21]. Regarding the elemental composition of the two SiN<sub>x</sub> layers, the EDX line scan reveals the presence of a significantly higher amount of Si as compared to N. The stoichiometry of the amorphous SiN<sub>x</sub> phase in TiSiN coatings is frequently described to be Si<sub>3</sub>N<sub>4</sub>, which can be attributed to the tendency of Si atoms to be tetrahedrally coordinated [9,22–24]. In the present work, however, the ratio of Si:N was found to be ~2:1. This significantly higher ratio as compared to the 3:4 ratio in Si<sub>3</sub>N<sub>4</sub> might be a result of the chosen deposition conditions. Haug et al. deposited TiN/SiN<sub>x</sub> nanocomposites by an arc evaporation/magnetron sputtering hybrid process and found that the stoichiometry of the SiN<sub>x</sub> phase was dependent on the state of the Si sputter target, being either elemental or nitrated by controlled target poisoning. While samples deposited using a primarily elemental target surface predominantly contained elemental Si, samples sputtered from nitrated targets predominantly contained SiN<sub>x</sub> [25].

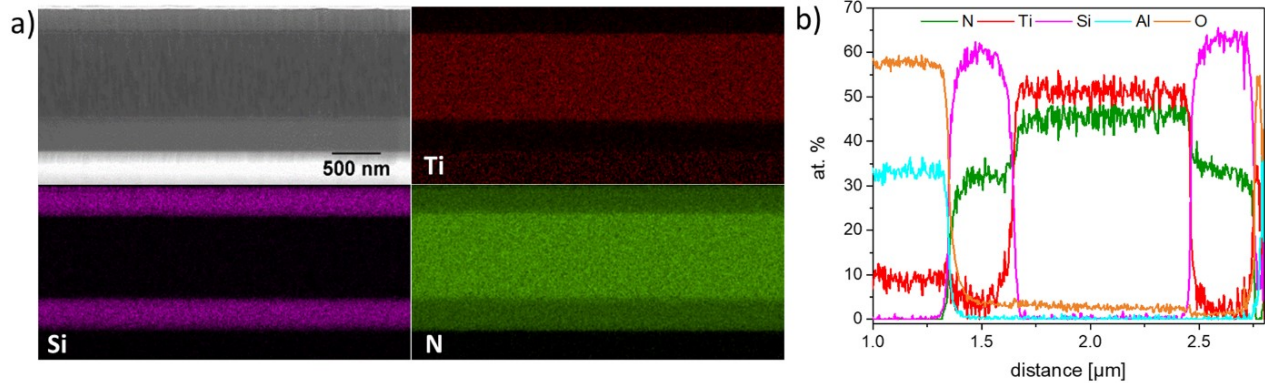


Fig. 2: a) Cross-sectional secondary electron SEM micrograph and corresponding EDX maps of Ti, Si and N recorded on an as-deposited  $\text{SiN}_x/\text{TiN}/\text{SiN}_x$  coating with 300 nm  $\text{SiN}_x$  layer thickness. b) EDX line scan showing the elemental distribution of N, Ti, Si, Al and O from the substrate to the coating surface.

Since the coatings within the present study were deposited using elemental Si targets, it should be evaluated whether the high ratio of Si:N is due to elemental Si being present within the  $\text{SiN}_x$  layers. Thus, X-ray diffractograms as well as Raman spectra of the three coatings in the as-deposited state were recorded (Fig. 3), to illuminate an eventual presence of elemental crystalline Si. The X-ray diffractograms of all  $\text{SiN}_x/\text{TiN}/\text{SiN}_x$  coatings (Fig. 3a) only contain reflections that can be assigned to face centered cubic (fcc) TiN (ICDD 00-038-1420) [26]. No peaks stemming from crystalline  $\text{TiSi}_x$  or  $\text{SiN}_x$  phases can be observed, proving the X-ray amorphous structure of the  $\text{SiN}_x$  layers. The two most intense Raman bands observed in the Raman spectra (Fig. 3b) of all three coatings positioned at  $\sim 160 \text{ cm}^{-1}$  and  $\sim 480 \text{ cm}^{-1}$  can be assigned to the first order transversal acoustic (TA) and transversal optical (TO) modes of amorphous Si, respectively. A second order TO band of amorphous Si is also visible at  $\sim 930 \text{ cm}^{-1}$  [27]. The band at  $\sim 800 \text{ cm}^{-1}$  can be assigned to amorphous  $\text{SiN}_x$  [27,28]. A weak shoulder positioned at  $\sim 465 \text{ cm}^{-1}$ , superimposed by the amorphous Si peak at  $\sim 480 \text{ cm}^{-1}$ , might indicate another  $\text{SiN}_x$  peak [28]. In contrast to the XRD investigations, the fcc-TiN phase cannot clearly be identified, however, the shoulder positioned at  $310 \text{ cm}^{-1}$  might be related to the TiN layer. Since

Raman spectroscopy measurements are conducted at relatively low measurement depth and all  $\text{SiN}_x/\text{TiN}/\text{SiN}_x$  coatings contain a  $\text{SiN}_x$  toplayer with thickness of at least 150 nm, it is likely that the typically weak intensity bands of fcc-TiN cannot be observed in the Raman spectra. Both X-ray diffractograms and Raman spectra do not reveal the presence of elemental crystalline Si. However, due to the simultaneous observation of amorphous Si and  $\text{SiN}_x$  in the Raman spectra, the existence of nanosized Si-rich regions in the amorphous  $\text{SiN}_x$  layers cannot be excluded. Therefore, the high ratio of Si:N of 2:1 found for the investigated coatings – compared to the theoretically expected stoichiometry of  $\text{Si}_3\text{N}_4$  [9,22–24] – may be attributed to the presence of small contents of amorphous Si.

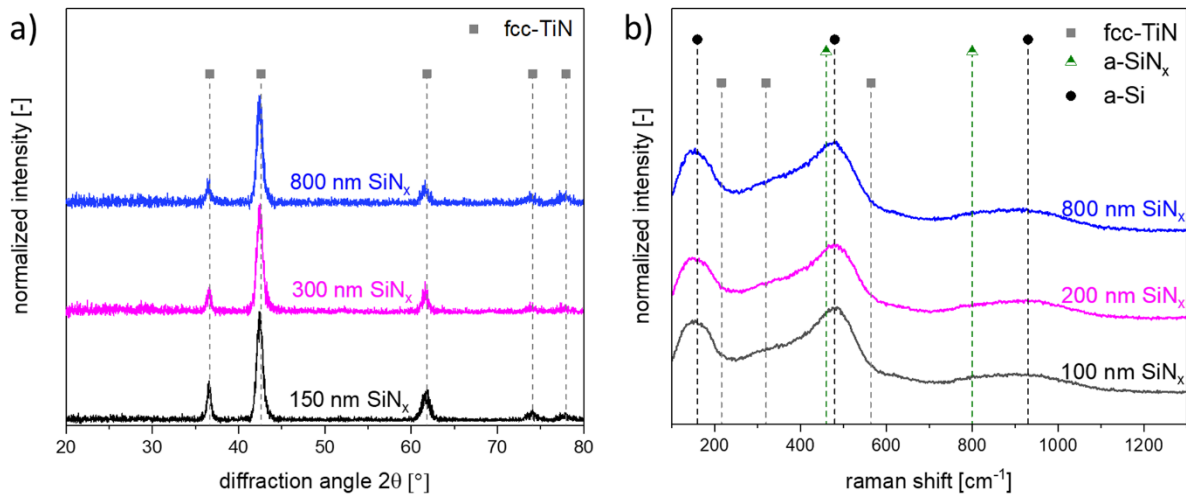


Fig. 3: a) X-ray diffractograms and b) Raman spectra of  $\text{SiN}_x/\text{TiN}/\text{SiN}_x$  coatings with varying  $\text{SiN}_x$  layer thickness in the as-deposited state.

In order to investigate the oxidation resistance of the  $\text{SiN}_x/\text{TiN}/\text{SiN}_x$  coatings in dependence of the  $\text{SiN}_x$  layer thickness, the coatings were oxidized at  $T \geq 800$  °C for 30 min and subsequently X-ray diffractograms (Fig. 4) were recorded. In Fig. 4a, diffractograms of the  $\text{SiN}_x/\text{TiN}/\text{SiN}_x$  coating with 150 nm  $\text{SiN}_x$  layer thickness in the as-deposited state and after oxidation for 30 min at 800, 1000 and 1200 °C, respectively, are depicted. After oxidation at 800 °C, the TiN layer remains non-oxidized and r- $\text{TiO}_2$  peaks (ICDD 01-079-5860) only start to emerge at a temperature of 1000 °C [26]. Increasing the temperature to



1200 °C results in the complete oxidation of the TiN layer, since only r-TiO<sub>2</sub> peaks are evident in the diffractogram. From the diffractograms of the coating with higher SiN<sub>x</sub> layer thickness of 300 nm in Fig. 4b it can be seen that hardly any oxidation of the TiN layer has taken place at 1000 °C. Furthermore – in contrast to 150 nm SiN<sub>x</sub> – still a significant fraction of non-oxidized fcc-TiN can be found at 1200 °C. Full oxidation of the TiN layer could only be achieved when further increasing the temperature to 1400 °C. Additional peaks at this temperature could be assigned to mullite (ICDD 01-074-4145) [26]. Mullite is known as a silicate with a stoichiometry of 3Al<sub>2</sub>O<sub>3</sub>-2SiO<sub>2</sub> and represents a stable intermediate phase in the Al-Si system under atmospheric pressure [29,30]. The formation of this phase can be attributed to diffusion of Al from the Al<sub>2</sub>O<sub>3</sub> substrate towards the coating surface, while bonding with O and Si available throughout the coating. The tendency of requiring higher temperatures for thicker SiN<sub>x</sub> layers to oxidize the TiN layer continues for the coating with 800 nm SiN<sub>x</sub> layer thickness (Fig. 4c). r-TiO<sub>2</sub> reflections with only low intensity can be observed at 1200 and 1400 °C and full oxidation is not even obtained after subjecting the coating to 1500 °C. Two additional phases are found to be formed during oxidation of this coating, namely crystalline Si (ICDD 00-027-1402) and crystalline β-Si<sub>3</sub>N<sub>4</sub> (ICDD 00-033-1160) [26]. While the crystalline Si phase appears at 1200 °C and vanishes again at higher temperatures, the β-Si<sub>3</sub>N<sub>4</sub> becomes clearly visible at 1500 °C. Since these phases appear to be present to a very small extent, they might only be detectable for the thickest SiN<sub>x</sub> layers of 800 nm. Overall, the XRD measurements clearly confirm the excellent shielding effect of the amorphous SiN<sub>x</sub> against oxidation of the TiN layer. While in literature TiN single-layer coatings are frequently reported to oxidize at ~500–550 °C [1,4,13], the onset of oxidation could be delayed significantly for the three-layer SiN<sub>x</sub>/TiN/SiN<sub>x</sub> coatings. Here, the oxidation resistance increased with increasing SiN<sub>x</sub> layer thickness, leading to a retarded oxidation onset of 1000, 1200 and 1400 °C, for the coatings with 150, 300 and 800 nm SiN<sub>x</sub> layer thickness, respectively. Analogously to the superior oxidation resistance of TiSiN

---

coatings, the phenomenon of an enhanced oxidation stability of the three-layer  $\text{SiN}_x/\text{TiN}/\text{SiN}_x$  coatings can be attributed to the shielding effect of the amorphous  $\text{SiN}_x$  layers by limiting diffusion of oxygen throughout the coating [12–14]. This barrier effect remains intact up to a certain threshold temperature depending on the  $\text{SiN}_x$  layer thickness, above which diffusion of oxygen through the  $\text{SiN}_x$  layers cannot be prevented anymore and oxidation of the TiN layer proceeds. In order to gain an understanding on why the barrier effect is not valid anymore above this onset temperature, additional investigations including optical light microscopy, Raman spectroscopy and SEM were conducted.

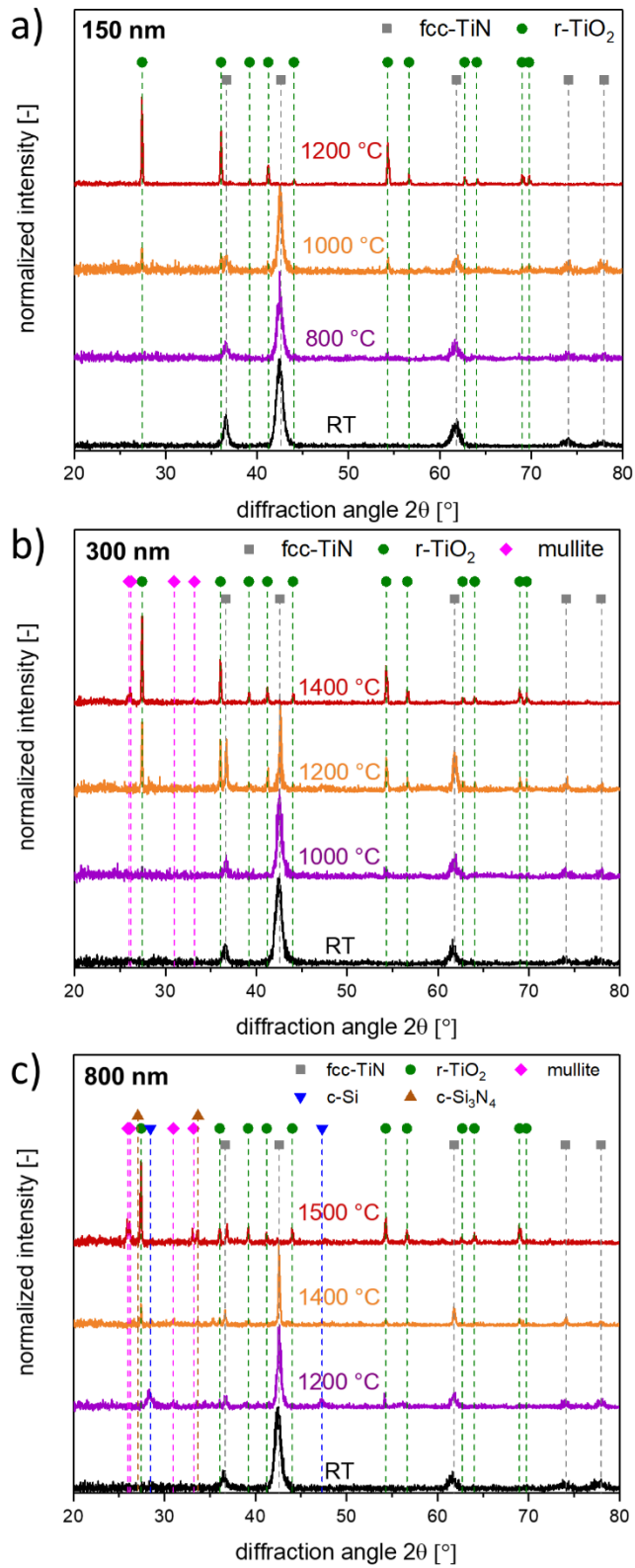


Fig. 4: X-ray diffractograms of SiN<sub>x</sub>/TiN/SiN<sub>x</sub> coatings oxidized at different temperatures for varying SiN<sub>x</sub> layer thicknesses of a) 150 nm b) 300 nm and c) 800 nm.

To get insight into the surface topography of the oxidized coatings, light optical microscopy images were recorded. Fig. 5 shows the micrographs of the three coatings exemplarily after oxidation at 1200 °C. When comparing the surface images for 150 (Fig. 5a), 300 (Fig. 5b) and 800 nm SiN<sub>x</sub> thickness (Fig. 5c), significant deviations become apparent. While the surface of the 150 nm coating appears to be fully covered by dark circular “spots”, the abundance of these spots strongly decreases with increasing SiN<sub>x</sub> layer thickness. To analyze the origin of these surface features, Raman spectroscopy measurements were taken specifically within these spots and are shown in Fig. 6.

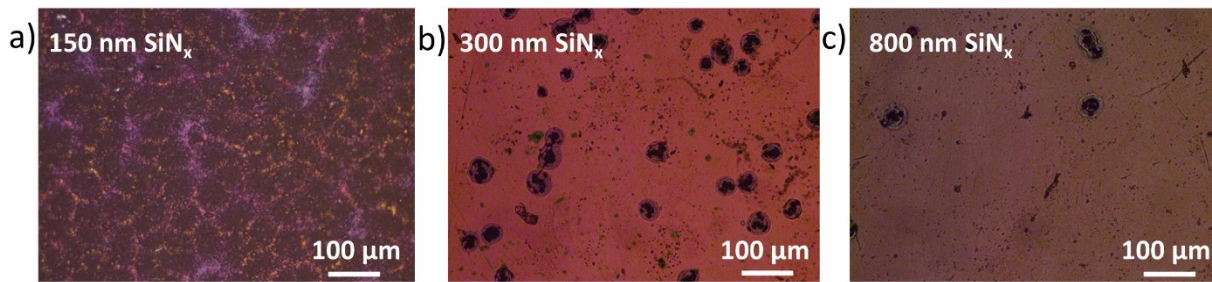


Fig. 5: Light optical microscopy images showing the surface of SiN<sub>x</sub>/TiN/SiN<sub>x</sub> coatings oxidized at 1200 °C for different SiN<sub>x</sub> layer thicknesses of a) 150 nm, b) 300 nm and c) 800 nm.

The Raman spectrum of the coating with 150 nm SiN<sub>x</sub> thickness exclusively exhibits bands assigned to r-TiO<sub>2</sub>. Thus, the dark and circular surface features observed in Fig. 5 can be attributed to r-TiO<sub>2</sub> grains that have grown through the SiN<sub>x</sub> top layer. The occurrence of r-TiO<sub>2</sub> correlates with the XRD measurements, where in this coating TiN was found to be entirely oxidized to r-TiO<sub>2</sub> after oxidation at 1200 °C. Furthermore, light optical micrographs (Fig. 5a) of this coating revealed the coverage of the entire surface area with dark surface features, now identified as r-TiO<sub>2</sub> grains. In the coating with 300 nm SiN<sub>x</sub> thickness a phase additionally to r-TiO<sub>2</sub> emerges, which was assigned to crystalline Si. Komarov et al. reported similar results in a study investigating the high temperature behavior of SiN<sub>0.46</sub> and SiN<sub>1.0</sub> coatings, where in both coatings crystalline Si nanoclusters formed after annealing at 1200 °C [31]. The detection of crystalline Si for the

300 nm  $\text{SiN}_x$  thickness sample by Raman spectroscopy is contradictory to the results found by XRD, where no crystalline Si could be detected. However, it should be considered that essentially small nanocrystals might not have been detected by XRD or were presumably present to such small extent that no corresponding peaks could unambiguously be identified in the X-ray diffractograms. Additionally, the Raman intensity of crystalline Si is extensively high, wherefore even small amounts of this phase can easily be detected by Raman spectroscopy. In contrast to the other two three-layer samples, the 800 nm  $\text{SiN}_x$  thickness coating barely exhibits any visible r- $\text{TiO}_2$  bands. Instead, the peak assigned to crystalline Si appears even more pronounced than for the 300 nm  $\text{SiN}_x$  coating. This observation can be attributed to the significantly thicker 800 nm  $\text{SiN}_x$  layers, where potentially more crystalline Si is formed, which was also confirmed by the XRD measurements for this coating.

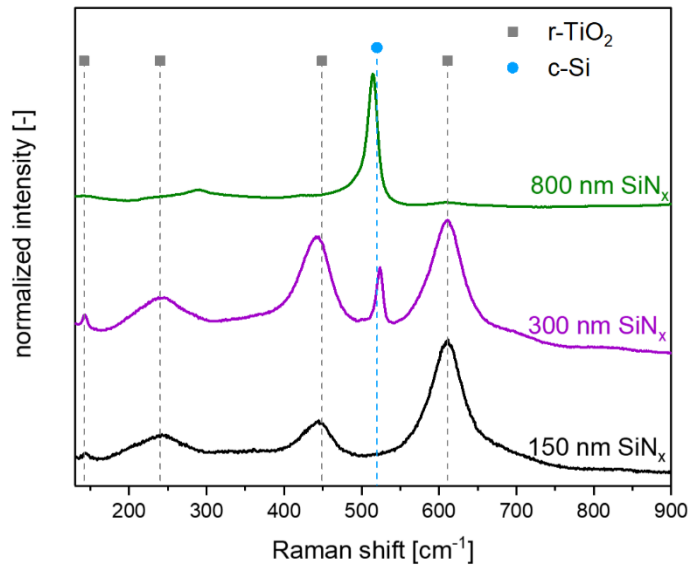


Fig. 6: Raman spectra recorded locally on surface features of  $\text{SiN}_x/\text{TiN}/\text{SiN}_x$  coatings with varying  $\text{SiN}_x$  layer thickness of 150 nm, 300 nm and 800 nm after oxidation at 1200 °C.

In order to obtain additional information about the microstructural changes within the coatings induced by oxidation, SEM images of the surface and cross-section as well as EDX maps of the cross-section of the coating with 300 nm  $\text{SiN}_x$  thickness were recorded

exemplarily and are shown in Fig. 7. The surface of the oxidized coating is depicted in two different magnifications in Fig. 7a and b. As already shown in the light optical micrograph (Fig. 5b), surface features emerge throughout the coating, which were identified to be  $r\text{-TiO}_2$  grains breaking through the  $\text{SiN}_x$  top layer. The cross-section and corresponding EDX maps in a region with no visible surface oxidation are shown in Fig. 7c. It is evident that the coating exhibits a more pronounced degree of porosity as compared to the as-deposited state in Fig. 1b. While pores appear to be present in all three layers of the coating, the degree of porosity seems to be increased in the upper  $\text{SiN}_x$  layer as well as on the upper interface to the TiN layer. Both the  $\text{SiN}_x$  layers and TiN layer are still intact and non-oxidized according to EDX maps. The formation of pores within the TiN layer can be explained analogously to the findings of Mayrhofer et al., who reported on the development of pores when oxidizing CrN coatings. The authors observed the formation of pores at the oxide/coating interface, resulting from the accumulation of vacancies. Additionally, nitrogen released by the oxidation of  $\text{Cr}_2\text{N}$  and CrN to  $\text{Cr}_2\text{O}_3$  was proposed to be accumulated at the coating/oxide interface, due to the nitrogen barrier function of  $\text{Cr}_2\text{O}_3$ , leading to the formation of pores and cavities [32]. In literature, also models describing the pore formation during oxidation of  $\text{Si}_3\text{N}_4$  ceramics have been proposed. Here, the formation of a porous layer containing pores filled with nitrogen at the interface of the oxide scale and  $\text{Si}_3\text{N}_4$  is reported and attributed to a non-equilibrium nitrogen concentration at the oxide/nitride interface as well as to an insufficient rate of nitrogen diffusion throughout the formed oxide scale to the surface [33]. This model describing the formation of pores filled with nitrogen might also explain the degree of porosity found for the amorphous  $\text{SiN}_x$  top layer in the three-layer coatings after oxidation at  $1200\text{ }^\circ\text{C}$ . The coating area where surface features were found to emerge (Fig. 7d) exhibits significant differences in its morphology as compared to the as-deposited state. Here, the  $r\text{-TiO}_2$  grains identified by XRD and Raman spectroscopy coarsened and break through the  $\text{SiN}_x$  top layer, while most of the  $\text{SiN}_x$  layer still appears to be non-oxidized. Taking a

close look at the respective EDX maps reveals areas of increased O intensity overlapping with areas rich in Si, indicating oxidation of a minor portion of the  $\text{SiN}_x$  layer to  $\text{SiO}_x$ .

Summarizing, the findings obtained in this study allow to describe the oxidation mechanism of the three-layer  $\text{SiN}_x/\text{TiN}/\text{SiN}_x$  coatings as follows:  $\text{SiN}_x$  shields TiN from oxidation up to temperatures  $> 800\text{ }^\circ\text{C}$ , whereby the exact onset temperature of oxidation depends on the thickness of the  $\text{SiN}_x$  layer. Here, thicker  $\text{SiN}_x$  layers have shown to be even more effective in prohibiting oxidation of the TiN layer at elevated temperatures. Once a critical temperature is reached, both the TiN and amorphous  $\text{SiN}_x$  layers have been found to become porous, thus leading to oxygen diffusion and eventually to the oxidation of TiN to r- $\text{TiO}_2$ . The r- $\text{TiO}_2$  grains show significant grain coarsening and eventually break through the  $\text{SiN}_x$  top layer.

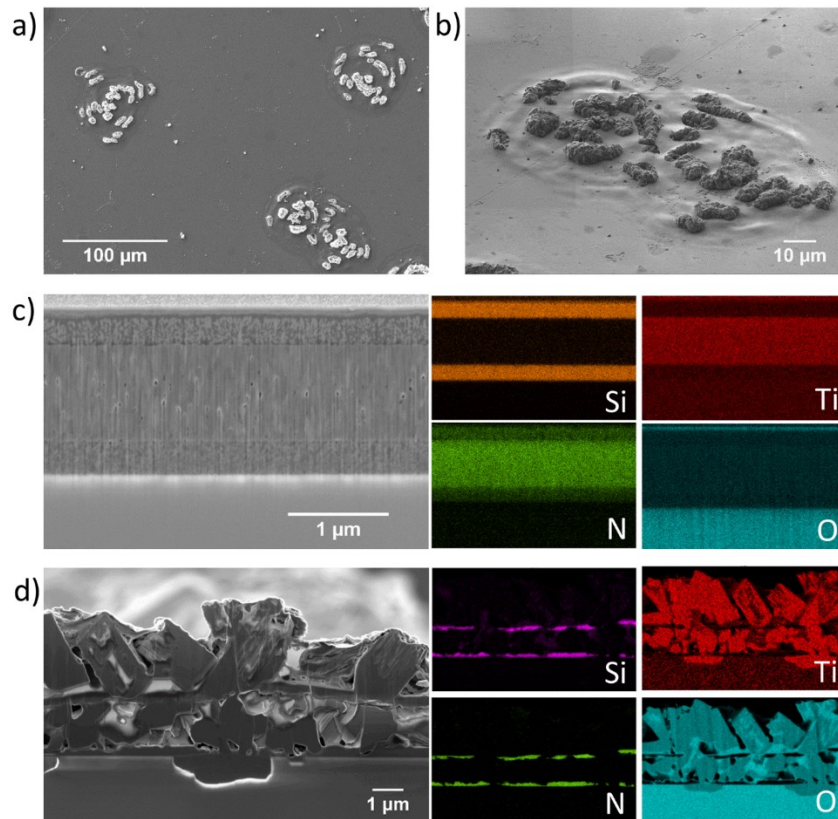


Fig. 7: Secondary electron SEM surface micrographs of the  $\text{SiN}_x/\text{TiN}/\text{SiN}_x$  coating with 300 nm  $\text{SiN}_x$  layer thickness subjected to  $1200\text{ }^\circ\text{C}$  in a) low and b) high magnification. Cross-sectional image and corresponding EDX maps of a c) non-oxidized and d) oxidized region.

#### 4. Conclusions

Within the scope of this study, the shielding effect of amorphous  $\text{SiN}_x$  onto crystalline TiN grains was investigated by depositing a model system based on three-layer  $\text{SiN}_x/\text{TiN}/\text{SiN}_x$  coatings with varying  $\text{SiN}_x$  layer thickness of 150, 300 and 800 nm. SEM and XRD investigations of the coatings in the as-deposited state revealed a crystalline structure for the TiN layer and an amorphous appearance for the  $\text{SiN}_x$  layers regardless of the layer thickness. XRD confirmed an excellent shielding effect of amorphous  $\text{SiN}_x$  against oxidation of the fcc-TiN phase, resulting in a significantly delayed oxidation onset temperature of the TiN layer. Increasing  $\text{SiN}_x$  layer thicknesses were hereby found to correlate with an even more enhanced resistance to oxidation for the TiN phase. A combination of SEM, EDX, Raman spectroscopy and optical light microscopy allowed to understand the microstructural changes induced by oxidation after annealing in air at 1200 °C. It was observed that the  $\text{SiN}_x$  layer becomes porous at elevated temperatures, thus enabling oxygen diffusion towards the likewise porous TiN layer, where r-TiO<sub>2</sub> grains are formed. These r-TiO<sub>2</sub> grains coarsen until they eventually break through the amorphous  $\text{SiN}_x$  top layer. Nonetheless, the amorphous  $\text{SiN}_x$  layers still remained mainly non-oxidized at 1200 °C, proving their significantly enhanced oxidation resistance compared to the crystalline fcc-TiN phase. The current study, using a model system of  $\text{SiN}_x/\text{TiN}/\text{SiN}_x$ , allows to understand the basic mechanisms occurring during oxidation of the TiSiN system, where nc-TiN grains are also shielded by the surrounding amorphous  $\text{SiN}_x$  phase from oxidation.

#### 5. Acknowledgments

The authors would like to thank Velislava Terziyska (Department of Materials Science) for the assistance during coating synthesis as well as Bernhard Sartory (Materials Center Leoben Forschung GmbH) for SEM investigations. The financial support by the



Austrian Federal Ministry for Digital and Economic Affairs and the National Foundation for Research, Technology and Development is gratefully acknowledged.

## 6. References

- [1] W. Münz, Titanium aluminum nitride films: A new alternative to TiN coatings, *J. Vac. Sci. Technol. A Vacuum, Surfaces, Film.* 4 (1986) 2717–2725.
- [2] B. Grossmann, N. Schalk, C. Czettl, M. Pohler, C. Mitterer, Phase composition and thermal stability of arc evaporated  $Ti_{1-x}Al_xN$  hard coatings with  $0.4 \leq x \leq 0.67$ , *Surf. Coat. Technol.* 309 (2017) 687–693.
- [3] C. Wüstefeld, D. Rafaja, V. Klemm, C. Michotte, M. Kathrein, Effect of the aluminium content and the bias voltage on the microstructure formation in  $Ti_{1-x}Al_xN$  protective coatings grown by cathodic arc evaporation, *Surf. Coat. Technol.* 205 (2010) 1345–1349.
- [4] Y.C. Chim, X.Z. Ding, X.T. Zeng, S. Zhang, Oxidation resistance of TiN, CrN, TiAlN and CrAlN coatings deposited by lateral rotating cathode arc, *Thin Solid Films.* 517 (2009) 4845–4849.
- [5] C. Kainz, N. Schalk, M. Tkadletz, C. Mitterer, C. Czettl, The effect of B and C addition on microstructure and mechanical properties of TiN hard coatings grown by chemical vapor deposition, *Thin Solid Films.* 688 (2019) 137283.
- [6] P.C. Jindal, A.T. Santhanam, U. Schleinkofer, A.F. Shuster, Performance of PVD TiN, TiCN, and TiAlN coated cemented carbide tools in turning, *Int. J. Refract. Met. Hard Mater.* 17 (1999) 163–170.
- [7] H.G. Prengel, W.R. Pfouts, A.T. Santhanam, State of the art in hard coatings for carbide cutting tools, *Surf. Coat. Technol.* 102 (1998) 183–190.
- [8] C. Rebholz, A. Leyland, P. Larour, C. Charitidis, S. Logothetidis, A. Matthews, The effect of boron additions on the tribological behaviour of TiN coatings produced by electron-beam evaporative PVD, *Surf. Coat. Technol.* 116–119 (1999) 648–653.
- [9] S. Vepřek, Conventional and new approaches towards the design of novel

- superhard materials, *Surf. Coatings Technol.* 97 (1997) 15–22.
- [10] M. Diserens, J. Patscheider, F. Lévy, Mechanical properties and oxidation resistance of nanocomposite TiN-SiN<sub>x</sub> physical-vapor-deposited thin films, *Surf. Coatings Technol.* 120–121 (1999) 158–165.
- [11] F. Pei, Y.X. Xu, L. Chen, Y. Du, H.K. Zou, Structure, mechanical properties and thermal stability of Ti<sub>1-x</sub>Si<sub>x</sub>N coatings, *Ceram. Int.* 44 (2018) 15503–15508.
- [12] A. Mège-Revil, P. Steyer, G. Thollet, R. Chiriac, C. Sigala, J.C. Sánchez-Lopéz, C. Esnouf, Thermogravimetric and in situ SEM characterisation of the oxidation phenomena of protective nanocomposite nitride films deposited on steel, *Surf. Coatings Technol.* 204 (2009) 893–901.
- [13] P. Steyer, D. Pilloud, J.F. Pierson, J.P. Millet, M. Charnay, B. Stauder, P. Jacquot, Oxidation resistance improvement of arc-evaporated TiN hard coatings by silicon addition, *Surf. Coatings Technol.* 201 (2006) 4158–4162.
- [14] D. Pilloud, J.F. Pierson, M.C. Marco de Lucas, A. Cavaleiro, Study of the structural changes induced by air oxidation in Ti-Si-N hard coatings, *Surf. Coatings Technol.* 202 (2008) 2413–2417.
- [15] Y. Moritz, C. Saringer, M. Tkadletz, A. Stark, N. Schell, I. Letofsky-Papst, C. Czettl, M. Pohler, N. Schalk, Oxidation behavior of arc evaporated TiSiN coatings investigated by in-situ synchrotron X-ray diffraction and HR-STEM, *Surf. Coat. Technol.* 404 (2020) 126632.
- [16] M. Arab Pour Yazdi, F. Lomello, J. Wang, F. Sanchette, Z. Dong, T. White, Y. Wouters, F. Schuster, A. Billard, Properties of TiSiN coatings deposited by hybrid HiPIMS and pulsed-DC magnetron co-sputtering, *Vacuum.* 109 (2014) 43–51.
- [17] J. Wu, N. He, H. Li, X. Liu, L. Ji, X. Huang, J. Chen, Deposition and characterization of TiAlSiN coatings prepared by hybrid PVD coating system, *Surf. Interface Anal.* 47 (2014) 184–191.
- [18] H. Söderberg, M. Odén, T. Larsson, L. Hultman, J.M. Molina-Aldareguia, Epitaxial

- stabilization of cubic-SiN<sub>x</sub> in TiN/SiN<sub>x</sub> multilayers, *Appl. Phys. Lett.* 88 (2006) 191902.
- [19] J. Xu, C.D. Lane, J. Ou, S.L. Cockcroft, D.M. Maijer, A. Akhtar, Y. Marciano, Diffusion of nitrogen in solid titanium at elevated temperature and the influence on the microstructure, *J. Mater. Res. Technol.* 12 (2021) 125–137.
- [20] H. Riedl, C.M. Koller, F. Munnik, H. Hutter, F. Mendez Martin, R. Rachbauer, S. Kolozsvári, M. Bartosik, P.H. Mayrhofer, Influence of oxygen impurities on growth morphology, structure and mechanical properties of Ti-Al-N thin films, *Thin Solid Films.* 603 (2016) 39–49.
- [21] P. Hones, R. Sanjinés, F. Lévy, Sputter deposited chromium nitride based ternary compounds for hard coatings, *Thin Solid Films.* 332 (1998) 240–246.
- [22] P. Zhang, Z. Cai, W. Xiong, Influence of Si content and growth condition on the microstructure and mechanical properties of Ti-Si-N nanocomposite films, *Surf. Coatings Technol.* 201 (2007) 6819–6823.
- [23] C.L. Chang, C.T. Lin, P.C. Tsai, W.Y. Ho, D.Y. Wang, Influence of bias voltages on the structure and wear properties of TiSiN coating synthesized by cathodic arc plasma evaporation, *Thin Solid Films.* 516 (2008) 5324–5329.
- [24] S. Vepřek, S. Reiprich, A concept for the design of novel superhard coatings, *Thin Solid Films.* 268 (1995) 64–71.
- [25] F.-J. Haug, P. Schwaller, J. Wloka, J. Patscheider, A. Karimi, M. Tobler, Stoichiometry dependence of hardness, elastic properties, and oxidation resistance in TiN/SiN<sub>x</sub> nanocomposites deposited by a hybrid process., *J. Vac. Sci. Technol. A.* 22 (2004) 1229.
- [26] S. Gates-Rector, T. Blanton, The Powder Diffraction File: a quality materials characterization database, *Powder Diffr.* 34 (2019) 352–360.
- [27] C.J. Oliphant, C.J. Arendse, T.F.G. Muller, D. Knoesen, Characterization of silicon nitride thin films deposited by hot-wire CVD at low gas flow rates, *Appl. Surf. Sci.*

- 285 (2013) 440–449.
- [28] L. V Mercaldo, E.M. Esposito, P.D. Veneri, G. Fameli, S. Mirabella, G. Nicotra, First and second-order Raman scattering in Si nanostructures within silicon nitride, *Appl. Phys. Lett.* 97 (2010) 153112.
- [29] D.J. Duval, S.H. Risbud, J.F. Shackelford, Mullite, in: J.F. Shackelford, R.H. Doremus (Eds.), *Ceram. Glas. Mater. Struct. Prop. Process.*, Springer, New York, 2008: pp. 27–39.
- [30] A. Cascales, N. Tabares, J.F. Bartolomé, A. Cerpa, A. Smirnov, R. Moreno, M.I. Nieto, Processing and mechanical properties of mullite and mullite-alumina composites reinforced with carbon nanofibers, *J. Eur. Ceram. Soc.* 35 (2015) 3613–3621.
- [31] F. Komarov, L. Vlasukova, I. Parkhomenko, O. Milchanin, A. Mudryi, A. Togambaeva, O. Korolik, Raman study of light-emitting SiN<sub>x</sub> films grown on Si by low-pressure chemical vapor deposition, *Thin Solid Films.* 579 (2015) 110–115.
- [32] P.H. Mayrhofer, H. Willmann, C. Mitterer, Oxidation kinetics of sputtered Cr-N hard coatings, *Surf. Coat. Technol.* 146–147 (2001) 222–228.
- [33] B.A. Galanov, S.M. Ivanov, E.V. Kartuzov, V.V. Kartuzov, K.G. Nickel, Y.G. Gogotsi, Model of oxide scale growth on Si<sub>3</sub>N<sub>4</sub> ceramics: nitrogen diffusion through oxide scale and pore formation, *Comput. Mater. Sci.* 21 (2001) 79–85.

# Publication IV

***In-situ* X-ray diffraction study of the oxidation behavior of arc  
evaporated TiAlSiN coatings with low Al contents**

Yvonne Moritz, Christian Saringer, Michael Tkadletz, Alexander Fian, Christoph Czettl,  
Markus Pohler, Nina Schalk

**Submitted to Surface & Coatings Technology (2023)**

# ***In-situ* X-ray diffraction study of the oxidation behavior of arc evaporated TiAlSiN coatings with low Al contents**

Yvonne Moritz<sup>a</sup>, Christian Saringer<sup>a</sup>, Michael Tkadletz<sup>b</sup>, Alexander Fian<sup>c</sup>,  
Christoph Czettel<sup>d</sup>, Markus Pohler<sup>d</sup>, Nina Schalk<sup>a</sup>

<sup>a</sup> Christian Doppler Laboratory for Advanced Coated Cutting Tools at the Department of Materials Science, Montanuniversität Leoben, Franz-Josef-Strasse 18, 8700 Leoben, Austria

<sup>b</sup> Department of Materials Science, Montanuniversität Leoben, Franz-Josef-Strasse 18, 8700 Leoben, Austria

<sup>c</sup> Institute for Surface Technologies and Photonics, JOANNEUM RESEARCH Forschungsgesellschaft, Franz-Pichler-Straße 30, 8160 Weiz, Austria

<sup>d</sup> CERATIZIT Austria GmbH, Metallwerk-Plansee-Strasse 71, 6600 Reutte, Austria

## **Abstract**

TiAlSiN hard coatings are commonly known to exhibit a high oxidation resistance, however, the influence of a varying Al content on the oxidation mechanism has not yet been examined in detail. Thus, in this work, the temperature dependent phase composition of two powdered TiAlSiN coatings with low Al contents ( $\text{Ti}_{37}\text{Al}_2\text{Si}_7\text{N}_{54}$  and  $\text{Ti}_{33}\text{Al}_6\text{Si}_7\text{N}_{54}$ ) was evaluated by *in-situ* X-ray diffraction (XRD) in ambient air up to 1200 °C and subsequent Rietveld refinement complemented by differential scanning calorimetry measurements. The *in-situ* XRD experiments revealed the formation of metastable anatase  $\text{TiO}_2$  during oxidation for both TiAlSiN coatings, however, the maximum wt.% of this phase was found to be doubled for the coating with higher Al content from 9 to 21 wt.% at ~1025 °C. Furthermore, the microstructure of the compact  $\text{Ti}_{33}\text{Al}_6\text{Si}_7\text{N}_{54}$  coating oxidized

at 950 and 1100 °C was investigated comprehensively by means of XRD, Raman spectroscopy, X-ray photoelectron spectroscopy and scanning electron microscopy. These microstructural investigations revealed the formation of a thin protective Al<sub>2</sub>O<sub>3</sub> layer, which was broken by the growth of TiO<sub>2</sub> grains after oxidizing at 950 °C, leading to fully enclosed Al<sub>2</sub>O<sub>3</sub> grains within coarsened TiO<sub>2</sub> grains at 1100 °C. The present work allows to close the literature gap concerning the changes in oxidation mechanism of TiAlSiN coatings when exclusively varying the Al content and further illuminates the microstructure of an oxidized TiAlSiN coating with low Al content in detail.

**Keywords:** PVD, TiAlSiN hard coatings, oxidation, *in-situ* XRD, Rietveld

## 1. Introduction

Physical vapor deposited (PVD) protective hard coatings are of high importance for the cutting industry, as they allow to enhance the service lifetime and performance of cutting tools. Among these protective coatings Ti<sub>1-x</sub>Al<sub>x</sub>N is widely applied, owing to its advantageous thermal and mechanical properties compared to the binary TiN coatings [1–5]. Besides the mechanical properties and thermal stability under inert conditions, also the oxidation resistance of protective hard coatings plays a key role during cutting applications [5]. Ti<sub>1-x</sub>Al<sub>x</sub>N coatings have shown to resist oxidation up to temperatures of approximately 800 °C, due to the formation of a protective Al<sub>2</sub>O<sub>3</sub> top layer that hinders diffusion of oxygen into the coatings [1]. Further increase of the oxidation stability has been attempted by the formation of quaternary coatings, adding elements such as Si, Ta or B to Ti<sub>1-x</sub>Al<sub>x</sub>N [6–9]. Among these elements, especially Si is known to significantly improve the mechanical properties as well as the thermal stability and oxidation resistance of Ti<sub>1-x</sub>Al<sub>x</sub>N. The structure of TiAlSiN coatings is frequently described as nanocomposite, meaning that nanocrystalline (nc) TiAlN grains are embedded in an amorphous SiN<sub>x</sub> matrix phase [7,10,11]. Several authors have studied the oxidation

resistance of TiAlSiN coatings with varying Si contents [7,9], or the Si and Al content have been simultaneously varied [8,12–18]. It has been shown that already the addition of small amounts of Si, such as 2 at.%, to the TiAl target material ( $\text{Ti}_{31}\text{Al}_{67}\text{Si}_2$ ) results in a significantly thinner oxide layer after oxidation of the TiAlSiN coating for a specific time compared to coatings deposited using a Si-free  $\text{Ti}_{33}\text{Al}_{67}$  target [9]. The enhanced oxidation stability was accompanied by the formation of a significantly higher amount of anatase (a)  $\text{TiO}_2$  at the expense of rutile (r)  $\text{TiO}_2$ . This observation was attributed to a slower grain growth of a- $\text{TiO}_2$  grains and a subsequently retarded transformation of a- $\text{TiO}_2$  to r- $\text{TiO}_2$ . Due to the retarded formation of r- $\text{TiO}_2$ , the grain coarsening of the rutile phase was less pronounced, leading to the generation of lower compressive stresses, which could crack the protective  $\text{Al}_2\text{O}_3$  top layer [9]. Other researchers, who investigated TiAlSiN coatings with higher Si contents (e.g.  $\text{Ti}_{0.5}\text{Al}_{0.4}\text{Si}_{0.1}\text{N}$  or  $\text{Ti}_{0.34}\text{Al}_{0.58}\text{Si}_{0.08}\text{N}$ ) also found an increasing amount of a- $\text{TiO}_2$  phase and enhanced oxidation resistance for TiAlSiN compared to TiAlN, which could be attributed to the formation of both,  $\text{Al}_2\text{O}_3$  and  $\text{SiO}_2$  barrier layers and a smaller grain size of TiAlSiN coatings [8,18]. Furthermore, Si has shown to increase the diffusion coefficient of Al, thus further promoting the formation of the  $\text{Al}_2\text{O}_3$  protective layer [18]. Studies, which simultaneously changed the Al and Si content in the TiAlSiN coatings reported on higher oxidation stability for higher  $(\text{Al}+\text{Si})/(\text{Ti}+\text{Al}+\text{Si})$  ratios [12,13], where the onset of oxidation could even be delayed to temperatures of 1115 °C with an  $(\text{Al}+\text{Si})/(\text{Ti}+\text{Al}+\text{Si})$  ratio of 0.67 [12].

Although several reports focus on the enhancement of the oxidation stability upon Si addition to TiAlN [7,9] or on the effect of varying  $(\text{Al}+\text{Si})/(\text{Ti}+\text{Al}+\text{Si})$  ratios [8,12–18], literature is lacking a detailed investigation of the influence of the Al content on the oxidation mechanism in TiAlSiN coatings, especially at low Al contents. Furthermore, to the best of our knowledge, no *in-situ* study of the oxidation mechanism of TiAlSiN has been published so far, leaving the temperature dependent phase composition upon oxidation unclear. Thus, in this work, the oxidation sequence of two powdered TiAlSiN



coatings with low Al contents of 2 and 6 at.% was investigated by *in-situ* X-ray diffraction (XRD) and evaluated by Rietveld refinement. Additionally performed differential scanning calorimetry (DSC) measurements of the powdered coatings as well as XRD, scanning electron microscopy (SEM), Raman and X-ray photoelectron spectroscopy (XPS) of an oxidized compact TiAlSiN coating with 6 at.% Al allowed to establish a profound understanding of the oxidation behavior of the TiAlSiN coating system.

## 2. Experimental Methods

The two TiAlSiN coatings investigated in this work were synthesized by cathodic arc evaporation (CAE) using an industrial scale Oerlikon Balzers Innova deposition plant. Targets with an elemental composition of  $\text{Ti}_{76}\text{Al}_4\text{Si}_{20}$  and  $\text{Ti}_{64}\text{Al}_{16}\text{Si}_{20}$  were produced powder metallurgically and used in the arc deposition process to obtain two coatings with different Al contents. Cemented carbide (CC) (92 wt.% WC, 6 wt.% Co and 2 wt.% mixed carbides) in SNUN geometry according to ISO 1832 [19], mild steel foil and single-crystalline sapphire with (0001) orientation were used as substrates. Prior to the CAE deposition process, the coatings were ion-etched in an Ar plasma. Pure  $\text{N}_2$  was used as deposition gas and the pressure and substrate temperature were set to  $3.5 \times 10^{-2}$  mbar and  $480^\circ\text{C}$ , respectively. After deposition, the coated steel foils were dissolved in nitric acid to obtain coating powders, which were used for DSC and *in-situ* XRD investigations. The elemental composition of the as-deposited TiAlSiN coating on CC substrate was determined by elastic recoil detection analysis (ERDA) using a 43 MeV  $\text{Cl}^{7+}$  ion beam.

Images of the surfaces and cross-sections of both TiAlSiN samples in the as-deposited state on CC, as well as of the oxidized coatings on  $\text{Al}_2\text{O}_3$  substrate, were acquired by SEM using a ZEISS GeminiSEM 450, the cross-sections were prepared with a Hitachi IM4000+ ion milling system using  $\text{Ar}^+$  ions. Bruker D8 Advance X-ray diffractometers were applied to investigate the microstructure of the compact TiAlSiN coatings on CC, using  $\text{Cu-K}\alpha$  ( $\lambda = 1.5418 \text{ \AA}$ ) radiation.  $\theta/2\theta$ - scans were performed utilizing a Göbel mirror. The diffraction patterns were recorded with an energy-dispersive Sol-X detector with

a measurement time of 1.0 s per step and a step size of  $0.02^\circ$ . Additionally, powdered coatings were analyzed in Bragg-Brentano geometry with a step-size of  $0.005^\circ$  and a measurement time of 1.0 s per step.

*In-situ* XRD measurements of the powdered  $\text{Ti}_{37}\text{Al}_2\text{Si}_7\text{N}_{54}$  and  $\text{Ti}_{33}\text{Al}_6\text{Si}_7\text{N}_{54}$  coatings were also carried out in Bragg-Brentano geometry. The powdered samples were heated in a high-temperature chamber “HTK 1200 N” by Anton Paar in ambient air. The temperature within the chamber was calibrated using a thermo-couple prior to the measurements. X-ray diffractograms of the TiAlSiN powder samples were measured at room temperature and subsequently between 600 and 1200 °C in steps of 25 °C, while remaining at each temperature step for ~15 min. Each pattern was recorded in a  $2\theta$ -range of 23 to  $47^\circ$ , applying a step-size of  $0.02^\circ$  and a measurement time of 0.5 s/step. The temperature-dependent phase composition of the samples during oxidation was evaluated using the Rietveld refinement approach with the software Topas 6. The influence of instrumental parameters was accounted for by refinement of the XRD pattern of a standard  $\text{LaB}_6$  powder sample (NIST 660c [20]) and applying the determined instrument function to the measured TiAlSiN powder patterns. Crystallographic information files (cif) were taken from the Crystallography Open Database (COD) and allowed to model the occurring phases during oxidation. COD files of TiN (COD-ID: 1011099), r-TiO<sub>2</sub> (COD-ID: 1534781), a-TiO<sub>2</sub> (COD-ID: 1526931) and  $\alpha$ -Al<sub>2</sub>O<sub>3</sub> (COD-ID: 1000017) were used. Difference curves between the recorded and modelled pattern were considered as measure for the quality of fit. Complementary to the *in-situ* powder XRD investigations, DSC and thermogravimetric analysis (TGA) of the TiAlSiN powder samples were performed in synthetic air, using a Setaram Labsys Evo DSC system. ~20 mg of the respective powder were placed into an Al<sub>2</sub>O<sub>3</sub> crucible and heated up to 1200 °C with the same average heating rate that was applied in the *in-situ* XRD measurements (1.7 K/min).

In addition to the investigation of the oxidation mechanism using the powdered coatings, the microstructure of the oxidized TiAlSiN coating with higher Al content

(Ti<sub>33</sub>Al<sub>6</sub>Si<sub>7</sub>N<sub>54</sub>) was studied in detail. Therefore, the Ti<sub>33</sub>Al<sub>6</sub>Si<sub>7</sub>N<sub>54</sub> coating deposited on sapphire substrates was oxidized in a Nabertherm N11/HR furnace in air at 950 °C and 1100 °C, respectively. The temperature was kept constant for 15 min for each oxidation experiment and the samples were allowed to cool down to room temperature outside the furnace. The microstructure of the oxidized samples was again analyzed with the above mentioned diffractometer in grazing incidence geometry. To obtain further information regarding the phase composition of the oxidized TiAlSiN coatings, Raman spectroscopy was performed using a LabRam HR800 spectrometer from Horiba Jobin-Yvon equipped with a frequency-doubled Nd-YAG laser ( $\lambda = 532$  nm). Raman spectra of the TiAlSiN coatings oxidized at 950 and 1100 °C, respectively, were recorded between 100 and 1000 cm<sup>-1</sup>.

To take a closer look at the surface morphology and cross-section of the samples after oxidation SEM investigations, using the same ZEISS instrument as stated above, were carried out on the Ti<sub>33</sub>Al<sub>6</sub>Si<sub>7</sub>N<sub>54</sub> sample after oxidation at 950 °C and 1100 °C. EDX maps of the cross-section and the surface were additionally recorded. To gain insight into the chemical bonding state of the amorphous SiN<sub>x</sub>/SiO<sub>x</sub> phases, the Ti<sub>33</sub>Al<sub>6</sub>Si<sub>7</sub>N<sub>54</sub> coating on sapphire substrate oxidized at 950 °C was investigated by XPS. An Omicron Multi-probe surface analysis system was used, equipped with a DAR 400 X-ray source, an XM 500 quartz crystal monochromator and an EA 125 hemispherical electron analyzer with a 5 channel pulse counting channeltron. An excitation energy of 1486.7 eV (Al-K $\alpha_1$ ) was used, while the pass energy was set to 20 eV. The binding energies of the recorded XPS spectra were corrected according to the calibration data of the spectrometer with Au, Ag and Cu standards [21]. Peak fitting of the XPS spectra was performed using a convolution of Lorentzian and Gaussian peak profiles and a Shirley background function with the software Unifit 2017. A sputter depth profile was recorded by Ar ion sputtering with an ISE 5 cold cathode sputter ion source from Omicron Nanotechnology. An ion energy of 2 keV was chosen for this experiment. The sputter rate was calculated from sputter time and the total layer thickness as determined from the SEM cross-section images. This rate

is known to be dependent on the binding energy of the compound [22]. From different binding energies of the oxide surface layer [23] and the nitride layer [24] the sputter rate of the nitride was estimated to be 2.5 times higher than that of the oxide, leading to a calculated oxide layer thickness which was in good agreement with the SEM measurements.

### 3. Results and Discussion

The elemental composition of the two TiAlSiN coatings was analyzed by ERDA, which allows to determine the quantity of light elements with high accuracy [25]. The composition of the two coatings was found to be  $\text{Ti}_{37}\text{Al}_2\text{Si}_7\text{N}_{54}$  and  $\text{Ti}_{33}\text{Al}_6\text{Si}_7\text{N}_{54}$ , while the composition of the targets was  $\text{Ti}_{76}\text{Al}_4\text{Si}_{20}$  and  $\text{Ti}_{64}\text{Al}_{16}\text{Si}_{20}$ , respectively. Compared to the target composition, both, the Al and the Si content are slightly lower, which can be attributed to more pronounced re-sputtering and gas phase scattering of these light elements [26]. The Si content for both coatings was found to be identical at 7 at.%, thus the influence of the addition of 2 or 6 at.% of Al on the oxidation mechanism can be directly compared. The nitrogen content is slightly overstoichiometric for both TiAlSiN coatings, which was already reported in a previous study on CAE TiAlSiN coatings [27]. This observation could be attributed to the formation of a  $\text{SiN}_x$  phase, which preferably shows a 3:4 stoichiometry of tetrahedrally coordinated  $\text{Si}_3\text{N}_4$  [27]. Impurity levels determined by ERDA were found to be very low at <0.4 at.% for O and <0.2 at.% for C.

In order to study the microstructure of the as-deposited TiAlSiN coatings on CC substrates, SEM images of the cross-sections were taken, which are depicted in Fig. 1a. Both coatings exhibit a fine-grained and feather-like structure, which has been reported by several authors for the addition of Si to Ti(Al)N coatings [28,29]. The small grain size is typically found for this coating system due to the formation of a nanocomposite structure, meaning that nc-TiAlN grains are embedded in an amorphous  $\text{SiN}_x$  tissue phase, which inhibits grain growth [7,30,31]. X-ray diffractograms of the two powdered and compact TiAlSiN coatings were recorded and are shown in Fig. 1b. The standard peak

positions of the different phases, namely face-centered cubic (fcc) TiN (ICDD 00-038-1420), fcc-AlN (ICDD 00-025-1495) and WC (originating from the CC substrate material), are depicted by dashed lines [32]. By comparing the X-ray diffractograms of compact (black) and powdered coatings (orange) it becomes apparent that the peak position is shifted to lower diffraction angles for the compact coatings, which can be attributed to the presence of compressive stresses [33]. Considering the peak position of the powdered coatings, which are essentially free of macroscopic residual stress, a shift to higher diffraction angles compared to the standard peak positions of fcc-TiN can be observed. This shift is found to be more pronounced for the coating with higher Al content ( $\text{Ti}_{33}\text{Al}_6\text{Si}_7\text{N}_{54}$ ) and is commonly reported for TiAlN coatings as a result of the formation of an fcc-TiAlN solid solution and thus, a decrease of the lattice parameter [1,3,34]. Furthermore, it is noteworthy that no wurtzitic AlN (w-AlN) phase is evident in the X-ray diffractograms of the TiAlSiN coatings. It has been reported that Si favors the formation of w-AlN [7,8,35], however, considering the low Al contents of 2 and 6 at.% of the coatings investigated in this study, it is not surprising that no w-AlN forms in the as-deposited coatings. In accordance with literature, the X-ray diffractograms of both coatings do not show the presence of  $\text{TiSi}_x$  or crystalline  $\text{SiN}_x$  phases, indicating that Si is present in an X-ray amorphous  $\text{SiN}_x$  phase, surrounding the nc-TiAlN grains [7,31,36]. However, it should further be considered that Si might - to a certain extent - be additionally present within a TiAlSiN solid solution, where both Al and Si substitute for Ti in the fcc-TiN lattice [7,37].

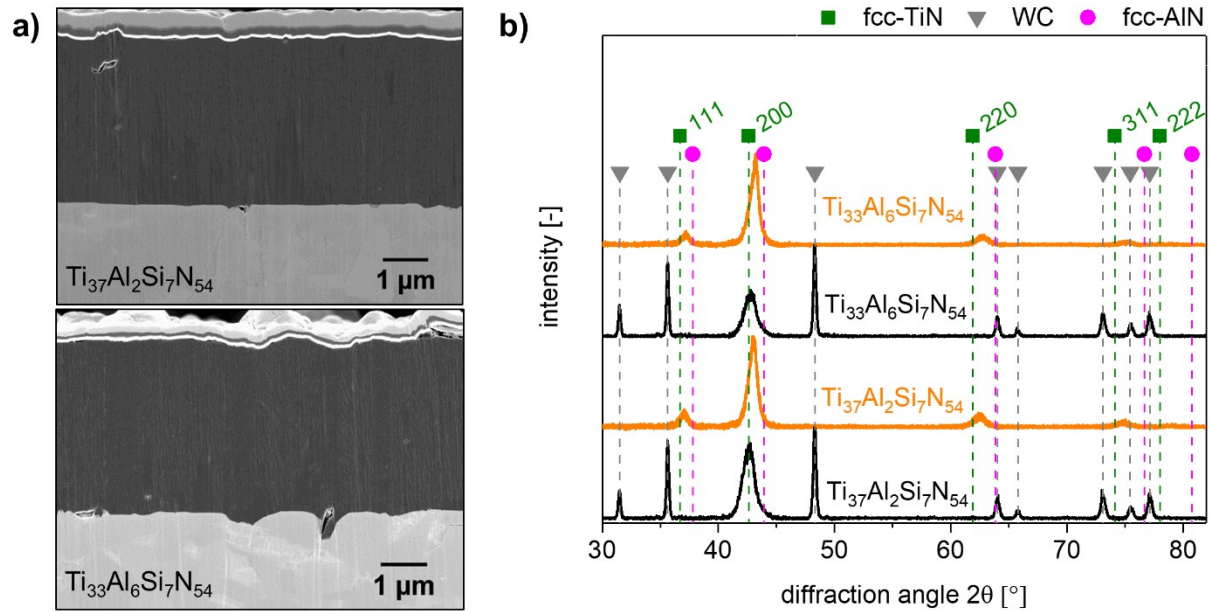


Fig. 1: SEM cross-section images of  $Ti_{37}Al_2Si_7N_{54}$  and  $Ti_{33}Al_6Si_7N_{54}$  (a). X-ray diffractograms of two powdered (orange) and compact (black) TiAlSiN coatings with varying Al content (b).

To monitor the oxidation mechanism of the two TiAlSiN coatings *in-situ*, X-ray diffractograms of the powdered coatings were recorded in steps of 25 °C between 600 and 1200 °C and the respective phase plots are depicted in Fig. 2. The standard peak positions of fcc-TiN (ICDD 00-038-1420), fcc-AlN (ICDD 00-025-1495), r-TiO<sub>2</sub> (ICDD 01-079-5860), a-TiO<sub>2</sub> (ICDD 01-075-2544) and  $\alpha$ -Al<sub>2</sub>O<sub>3</sub> (ICDD 00-042-1468) are again indicated by symbols and dashed lines [32]. All peaks exhibit a slight shift to lower diffraction angles with increasing temperature, which is an effect of the thermal expansion of the lattices. When comparing the phase plots of the  $Ti_{37}Al_2Si_7N_{54}$  (Fig. 2a) and the  $Ti_{33}Al_6Si_7N_{54}$  (Fig. 2b) coating it becomes apparent that oxidation for both powdered coatings starts at ~800 °C, when r-TiO<sub>2</sub> and a-TiO<sub>2</sub> peaks become visible in the X-ray diffractograms. Literature values concerning the onset of oxidation for TiAlSiN coatings vary, depending on the elemental composition of the coating. For example, Chang et al. investigated TiAlSiN coatings with (Al+Si)/(Ti+Al+Si) ratios ranging from 0.23 to 0.67 and found an onset of oxidation between 900 °C and 1115 °C, where higher onset temperatures

correlated with increasing (Al+Si)/(Ti+Al+Si) ratios. The delayed start of oxidation as well as a lower oxidation rate for the higher (Al+Si)/(Ti+Al+Si) ratio was attributed to the formation of a protective oxide layer, which mainly consisted of  $\alpha$ -Al<sub>2</sub>O<sub>3</sub> and inhibited further oxygen diffusion through the coating [12]. For the coatings investigated in the present study, an oxidation onset of ~800 °C is observed for both (Al+Si)/(Ti+Al+Si) ratios of 0.19 or 0.30, which is lower compared to Chang et al. [12]. However, different heating rates might affect the oxidation rate of the coatings, which makes a direct comparison to oxidation onset temperatures of different studies challenging. Another difference, which is observable between the two phase plots is the occurrence of  $\alpha$ -Al<sub>2</sub>O<sub>3</sub> at ~900 °C for Ti<sub>33</sub>Al<sub>6</sub>Si<sub>7</sub>N<sub>54</sub>, which cannot be clearly identified in the phase plot of Ti<sub>37</sub>Al<sub>2</sub>Si<sub>7</sub>N<sub>54</sub>. The formation of a protective Al<sub>2</sub>O<sub>3</sub> layer is typically observed in literature for the oxidation of TiAlSiN coatings [8,12,18]. However, considering the low Al content of only 2 at.% for the Ti<sub>37</sub>Al<sub>2</sub>Si<sub>7</sub>N<sub>54</sub>, peaks related to  $\alpha$ -Al<sub>2</sub>O<sub>3</sub> cannot clearly be identified in the recorded X-ray diffractograms. Another visible difference between the two phase plots can be noticed when taking a closer look at the anatase peak positioned at ~25.5°, which shows a significantly higher intensity for Ti<sub>33</sub>Al<sub>6</sub>Si<sub>7</sub>N<sub>54</sub> compared to Ti<sub>37</sub>Al<sub>2</sub>Si<sub>7</sub>N<sub>54</sub>. In order to quantify this different phase composition, a Rietveld refinement approach was used for the evaluation of both *in-situ* XRD measurements, allowing to monitor the quantitative temperature dependent phase composition continuously between 600 and 1200 °C.

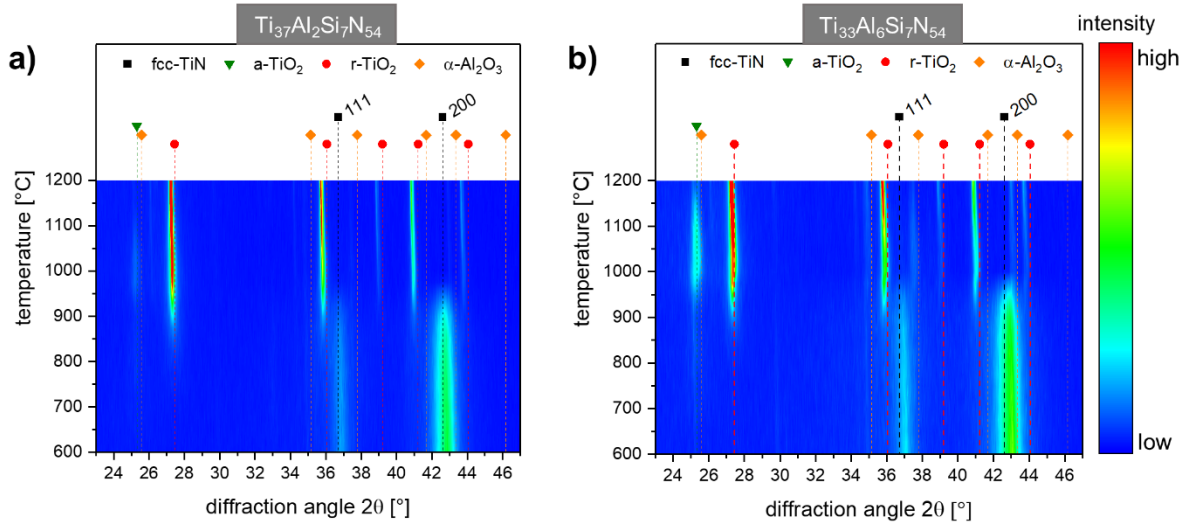


Fig. 2: Phase plots of the X-ray diffractograms recorded by in-situ XRD in ambient air between 600 and 1200 °C for  $Ti_{37}Al_2Si_7N_{54}$  (a) and  $Ti_{33}Al_6Si_7N_{54}$  (b).

The results obtained by Rietveld refinement are summarized in Fig. 3. At a temperature of  $\sim 770$  °C, the amount of fcc-TiAlN starts to decrease for both TiAlSiN coatings. Determination of the quantitative phase composition revealed the presence of  $\sim 90$  wt.% of the fcc-TiAlN phase for the  $Ti_{37}Al_2Si_7N_{54}$  powdered coating at  $\sim 770$  °C, while for the  $Ti_{33}Al_6Si_7N_{54}$  powdered coating still  $\sim 95$  wt.% of the fcc-TiAlN phase were detected, indicating a slightly retarded oxidation onset for the higher Al content. Above  $\sim 770$  °C a continuous increase of both, a-TiO<sub>2</sub> and r-TiO<sub>2</sub> can be observed up to a temperature of  $\sim 1025$  °C, where a-TiO<sub>2</sub> reaches a maximum for both coatings and then continuously decreases up to 1200 °C. Contrarily to the oxidation of binary TiN coatings – where usually only the stable r-TiO<sub>2</sub> modification is formed – the formation of the metastable a-TiO<sub>2</sub> phase has been reported by several authors for Ti(Al)SiN coatings [7,9,38]. This alteration in the oxidation mechanism between TiN and nanocomposite Ti(Al)SiN coatings has generally been attributed to the significantly decreased grain size upon Si addition to Ti(Al)N, leading to a preferred formation of the a-TiO<sub>2</sub> phase, which is known to be stabilized at small grain sizes below  $\sim 11$  nm [38,39]. Chen et al. investigated the changes in oxidation behavior of TiAlN coatings after Si addition *ex-situ* by XRD. It was



found that the oxidation stability was significantly enhanced for TiAlSiN, due to the promoted formation of an Al<sub>2</sub>O<sub>3</sub>-rich top-scale and also a retarded transformation of a-TiO<sub>2</sub> into r-TiO<sub>2</sub> [8]. Similarly, Pfeiler et al. reported on an enhanced oxidation resistance of their coatings upon adding 2 at.% of Si to the TiAlN target material, which was accompanied by a significantly higher content of metastable a-TiO<sub>2</sub> in the formed oxide scale and a retarded anatase-rutile transformation [9]. When comparing the wt.% of the anatase phase occurring during oxidation of Ti<sub>37</sub>Al<sub>2</sub>Si<sub>7</sub>N<sub>54</sub> and Ti<sub>33</sub>Al<sub>6</sub>Si<sub>7</sub>N<sub>54</sub> shown in the present study, it becomes evident that not only the Si content, but also the Al content seem to influence the ratio of r-TiO<sub>2</sub>/a-TiO<sub>2</sub> significantly. While a maximum of 9 wt.% of a-TiO<sub>2</sub> was determined to form for the coating with lower Al content of 2 at.%, a more than twofold increase of the anatase phase fraction to 21 wt.% was found for the coating containing 6 at.% of Al. Since the Si content is identical for both TiAlSiN coatings, the grain size in the as-deposited state of the coatings is not expected to vary strongly, wherefore attributing the much higher anatase phase fraction to a difference in grain size of the coatings seems not to be reasonable. However, a valid explanation for the change in the temperature-dependent phase composition might be a reduced grain coarsening throughout the oxidation process at elevated temperatures, likely as a result of the more efficient formation of a protective  $\alpha$ -Al<sub>2</sub>O<sub>3</sub> top-layer for the coating with higher Al content (Ti<sub>33</sub>Al<sub>6</sub>Si<sub>7</sub>N<sub>54</sub>). The wt.% of the  $\alpha$ -Al<sub>2</sub>O<sub>3</sub> phase was only determined for the oxidation of the Ti<sub>33</sub>Al<sub>6</sub>Si<sub>7</sub>N<sub>54</sub> coating (Fig. 3b), since this phase could not unambiguously be identified in the X-ray diffractograms of the Ti<sub>37</sub>Al<sub>2</sub>Si<sub>7</sub>N<sub>54</sub> coating, owing to the low Al content of 2 at.%. Also, regarding the Ti<sub>33</sub>Al<sub>6</sub>Si<sub>7</sub>N<sub>54</sub> coating, the  $\alpha$ -Al<sub>2</sub>O<sub>3</sub> phase could only be fitted and quantified at higher temperatures  $\geq 1000$  °C, since at lower temperatures the peaks of the fcc-TiAlN and  $\alpha$ -Al<sub>2</sub>O<sub>3</sub> phases strongly overlap. In literature, mostly oxidation studies on TiAlSiN coatings with significantly higher Al contents were conducted, thus the occurrence of  $\alpha$ -Al<sub>2</sub>O<sub>3</sub> was commonly observed by XRD investigations at  $\sim 900$  °C [12].

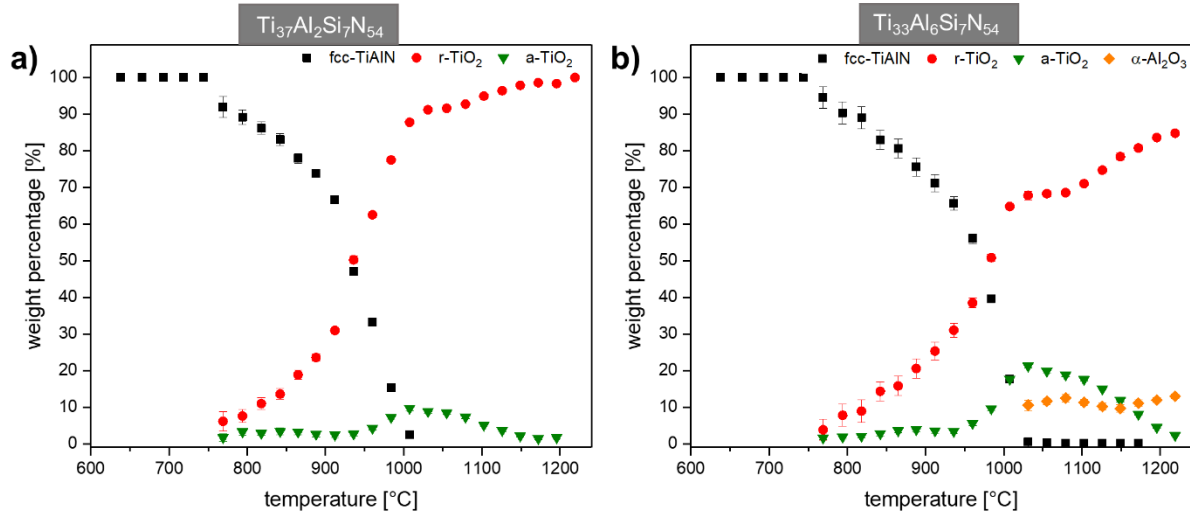


Fig. 3: Evolution of phase fractions in wt.% with increasing oxidation temperature of  $Ti_{37}Al_2Si_7N_{54}$  and  $Ti_{33}Al_6Si_7N_{54}$  powdered coatings evaluated by Rietveld refinement.

Complementary to the *in-situ* XRD investigation, DSC/TGA measurements in synthetic air were carried out for both powdered coatings using an identical average heating rate. The heat flow and TG signal are shown in Fig. 4a and 4b for the oxidation of the  $Ti_{37}Al_2Si_7N_{54}$  and  $Ti_{33}Al_6Si_7N_{54}$  powdered coatings, respectively. While the TG signal for the  $Ti_{37}Al_2Si_7N_{54}$  coating starts to rise slightly at  $\sim 600$  °C, an increase of this signal for the  $Ti_{33}Al_6Si_7N_{54}$  coating is only found above 700 °C, indicating the beginning oxidation of the coatings, whereby the increase in mass seems to be slightly lower for the higher Al content in temperature ranges up to  $\sim 900$  °C. This further corroborates that the oxidation is proceeding slightly slower for the higher Al content. When taking a closer look at Fig. 4a it becomes apparent that the strong exothermic peak with a maximum located at 980 °C also shows a pronounced shoulder at  $\sim 880$  °C. This shoulder can be attributed to the formation of anatase, which subsequently transforms into the stable rutile modification. Similar results were observed in a previous study for DSC measurements of a TiSiN coating in synthetic air, which also clearly exhibited a shoulder of the exothermic peak related to the formation of a-TiO<sub>2</sub> [40]. However, the heat flow signal of the coating with higher Al content in Fig. 4b does not show such a pronounced shoulder, which might be

due to a significantly higher amount of  $\alpha$ -Al<sub>2</sub>O<sub>3</sub> forming during the oxidation process, which potentially leads to a peak overlap, since the formation of  $\alpha$ -Al<sub>2</sub>O<sub>3</sub> has been reported to occur at a temperature of ~900 °C upon oxidation of PVD TiAlSiN coatings [12].

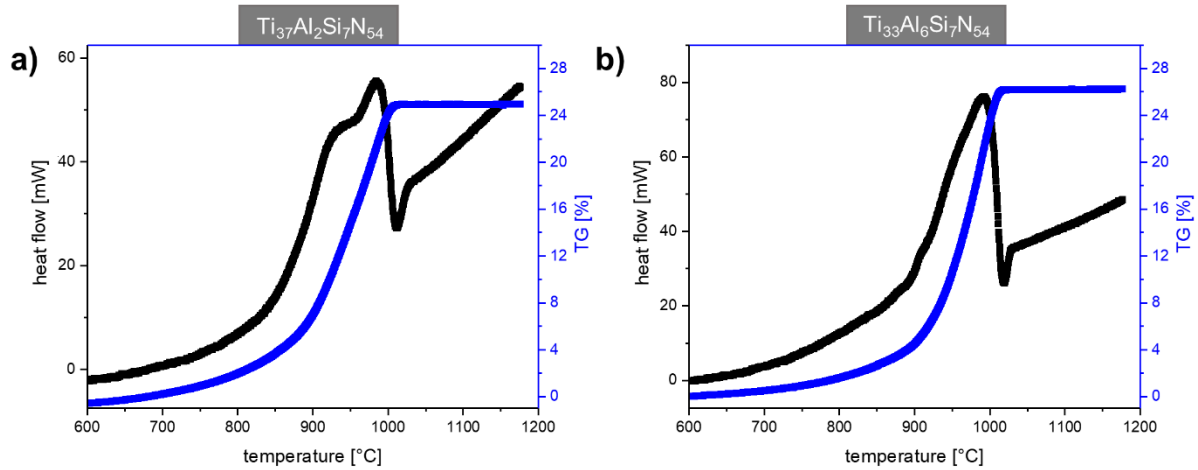


Fig. 4: Heat flow and thermogravimetric signal as a function of the oxidation temperature of powdered  $Ti_{37}Al_2Si_7N_{54}$  (a) and  $Ti_{33}Al_6Si_7N_{54}$  (b) coatings.

In order to not only study the oxidation mechanism, but to also develop a profound understanding of the changes in microstructure upon oxidation, the TiAlSiN coating with higher Al content was additionally investigated in compact state. Therefore, the  $Ti_{33}Al_6Si_7N_{54}$  deposited on a sapphire substrate was annealed in ambient air for 15 min at 950 and 1100 °C, respectively. The X-ray diffractograms of the coating oxidized at the two different temperatures are depicted in Fig. 5a. At 950 °C it becomes apparent that the oxidation of the coating has already started, however fcc-TiAlN still remains the predominant phase. r-TiO<sub>2</sub> can additionally be clearly identified and the peak at ~25° can be assigned to a-TiO<sub>2</sub>, which is in accordance with the oxidation of the powdered coatings, where both TiO<sub>2</sub> modifications were found at a temperature of 950 °C. When increasing the temperature to 1100 °C, significantly sharper peaks can be observed, indicating grain coarsening. No fcc-TiAlN peaks are present anymore, signifying full oxidation of the

coating at 1100 °C, which is again consistent with results obtained from *in-situ* powder XRD measurements. Furthermore, peaks originating from the  $\alpha$ -Al<sub>2</sub>O<sub>3</sub> phase are visible. Since the presence of  $\alpha$ -Al<sub>2</sub>O<sub>3</sub> makes it difficult to differentiate between the a-TiO<sub>2</sub> peak and the  $\alpha$ -Al<sub>2</sub>O<sub>3</sub> peak at ~25°, additionally Raman spectra of the oxidized coating were acquired, shown in Fig. 5b. Standard peak positions of the individual phases in the Raman spectra are indicated by symbols and dashed lines according to ref. [41–43]. The Raman spectrum of the Ti<sub>33</sub>Al<sub>6</sub>Si<sub>7</sub>N<sub>54</sub> coating oxidized at 950 °C clearly reveals a substantial amount of a-TiO<sub>2</sub> being present within the coating. Hardly any fcc-TiAlN bands can be observed although the X-ray diffractograms still revealed a significant amount of this phase at 950 °C. However, it needs to be kept in mind that the Raman intensity of the oxide phases is considerably higher, thus, masking the low intensity bands of the fcc-TiAlN phase. At 1100 °C, the amount of the a-TiO<sub>2</sub> phase has strongly decreased compared to the Raman spectrum at 950 °C, which is consistent with the investigation of the oxidation mechanism on the powdered coating and can be attributed to the transformation of anatase into the stable rutile modification due to extension of a critical grain size [38]. Peaks assigned to  $\alpha$ -Al<sub>2</sub>O<sub>3</sub> could not be clearly identified, since they are partly overlapping with the peaks of r-TiO<sub>2</sub> with the most intense peak expected to be located at 420 cm<sup>-1</sup>. Additionally,  $\alpha$ -Al<sub>2</sub>O<sub>3</sub> is also known to exhibit a low Raman scattering efficiency [44].

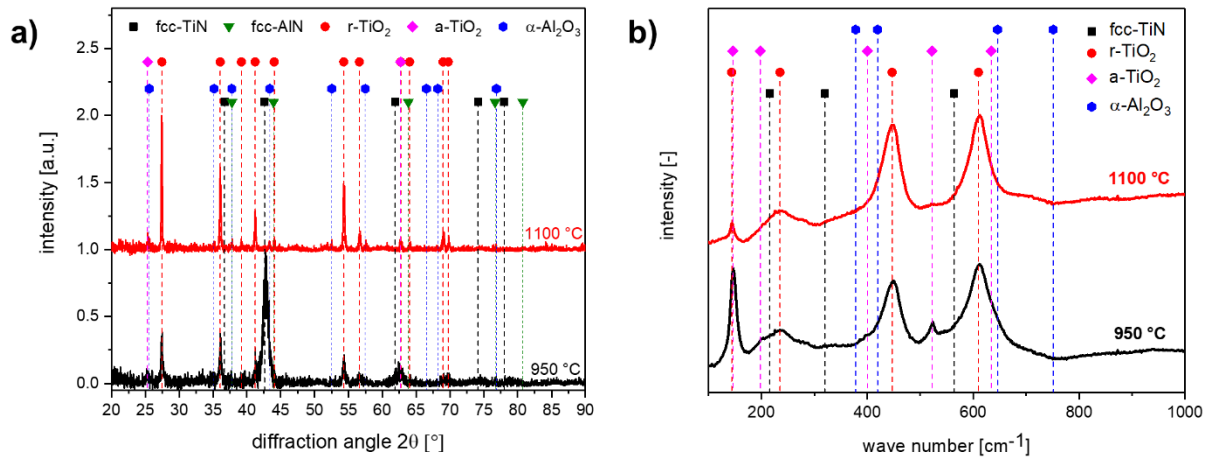


Fig. 5: X-ray diffractograms (a) and Raman spectra (b) of a  $Ti_{33}Al_6Si_7N_{54}$  coating on sapphire substrate oxidized at 950 and 1100 °C for 15 min each.

Since it is not feasible to observe the oxidation of the amorphous  $SiN_x$  phase by XRD measurements, additional XPS depth-sputter experiments were carried out on the partially oxidized  $Ti_{33}Al_6Si_7N_{54}$  sample annealed at 950 °C. These measurements allowed to evaluate the quantitative fraction of the elements Ti, Si, Al, N and O as well as the ratio of SiN/SiO as a function of the sputter depth until reaching the substrate material and are depicted in Fig. 6. It has to be pointed out that the quantitative evaluation by XPS helps to visualize trends, but cannot be regarded as a precise quantitative analysis of the coating composition. There is – to some extent - the possibility of preferential sputtering as well as sputter induced chemical decomposition and, therefore, shifts in element ratios and core level binding energies [45,46]. Considering the elemental fraction in the lower diagram of Fig. 6 it becomes apparent that the Al content is highest up to a sputter depth of ~150 nm and then decreases, correlating with the formation of an  $Al_2O_3$  top layer at the surface of the coating, which has frequently been reported in literature for the oxidation of TiAlSiN coatings [8,12,14,18]. XRD measurements of the compact coating oxidized at 950 °C, shown in Fig. 5a, could not clearly confirm the presence of  $\alpha$ - $Al_2O_3$ , possibly due to only small amounts of this phase being present. However, XPS results now indicate the

occurrence of  $\alpha$ - $\text{Al}_2\text{O}_3$  already at temperatures of 950 °C. At the same time, a low content of Si can be found in the surface near region up to a sputter depth of ~600 nm, where the Si fraction is observed to rise. Above a sputter depth of 600 nm, the oxygen content continuously decreases while the N content increases, meaning that a depth is reached where the coating is not fully oxidized. Once the substrate is reached, the Al and O content are found to increase again, owing to the fact that sapphire was chosen as substrate material. Chen et al. similarly evaluated the XPS depth profile of a TiAlSiN coating with 16 at.% of Si and 6 at.% of Al after oxidation at 800 °C for 1 h and - on the contrary to our results - found a rather constant ratio of Ti, Si and Al over the coating thickness, indicating no outward diffusion of elements or formation of an  $\text{Al}_2\text{O}_3$  top layer [13]. They attributed this absent Al enrichment to either the low Al content within their coating or to the low oxidation temperature of 800 °C. However, since the  $\text{Al}_2\text{O}_3$  enrichment in the surface near region clearly became apparent for the  $\text{Ti}_{33}\text{Al}_6\text{Si}_7\text{N}_{54}$  coating with an identically low Al content of 6 at.% in our study, rather the oxidation temperature seems to have an influence whether the formation of an  $\text{Al}_2\text{O}_3$  top layer is fostered or not.

Due to the reason that the oxidation of the  $\text{SiN}_x$  phase cannot be monitored by XRD it was attempted to evaluate the  $\text{SiN}_x/\text{SiO}_x$  ratio over the sputter depth and the results are depicted in the upper diagram of Fig. 6. Above a sputter depth of ~600 nm, the  $\text{SiN}_x/\text{SiO}_x$  ratio increases, meaning that – as expected – the quantity of the non-oxidized  $\text{SiN}_x$  phase rises at increasing coating depth. To compare the degree of oxidation of the crystalline TiAlN phase and the amorphous  $\text{SiN}_x$  phase at the same coating depth, the respective Ti2p and Si2p spectra at two different sputter depths of 600 and 1500 nm are shown in Fig. 7. According to binding energies found in literature [47,48], four different components, namely  $\text{TiO}_2$ ,  $\text{TiO}_x\text{N}_y$ , TiN and metallic Ti, can be assigned to contribute to the Ti2p core level spectra shown in Fig. 7a, for a sputter depth of 600 nm. When taking a look at the respective peak areas of the individual components,  $\text{TiO}_2$  appears to be the dominant phase. When considering the Si2p peak at an identical sputter depth of 600 nm,

$\text{SiN}_x$  and  $\text{SiO}_x$  can be identified as contributing components according to their binding energies [49–51], where  $\text{SiN}_x$  is the dominant phase and the quantification revealed a ratio of  $\sim 1.2$  for  $\text{SiN}_x/\text{SiO}_x$ . Thus, it can be concluded that at an identical  $\text{Ti}_{33}\text{Al}_6\text{Si}_7\text{N}_{54}$  coating depth a higher fraction of the crystalline TiAlN is oxidized compared to the amorphous  $\text{SiN}_x$  phase, which appears to be more resistant to oxidation. At a higher sputter depth of 1500 nm the Ti2p core level spectra (Fig. 7b) reveal a larger fraction of non-oxidized TiN compared to the sputter depth of 600 nm, however, still a significant amount of  $\text{TiO}_2$  and  $\text{TiO}_x\text{N}_y$  can be detected. The Si2p peak at a sputter depth of 1500 nm shows that primarily  $\text{SiN}_x$  can be found and only small amounts of  $\text{SiO}_x$  can be detected, leading to a ratio of  $\sim 10$  for  $\text{SiN}_x/\text{SiO}_x$ , again confirming the superior oxidation resistance of the amorphous  $\text{SiN}_x$  phase over the crystalline TiAlN phase.

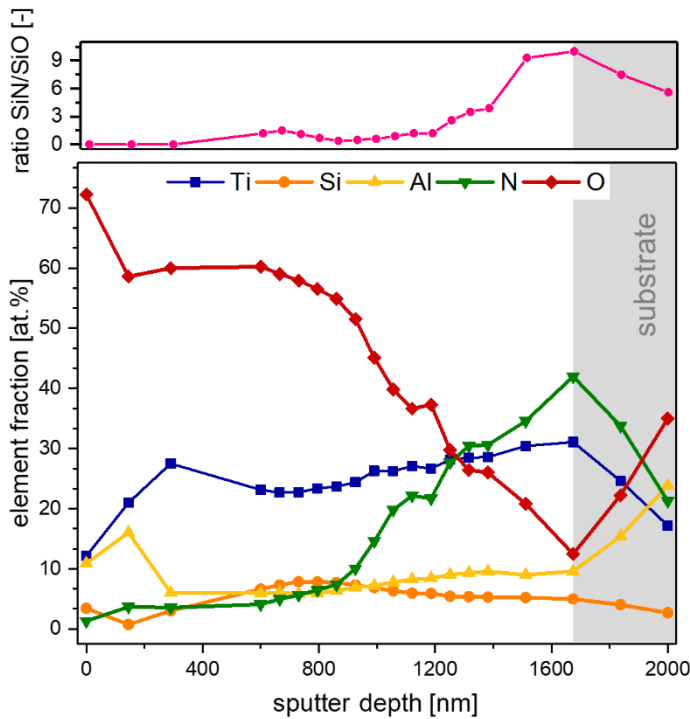


Fig. 6: Molar ratio of  $\text{SiN}/\text{SiO}$  and quantitative element fraction of Ti, Si, Al, N and O as a function of sputter depth determined from XPS depth-sputter experiment of a  $\text{Ti}_{33}\text{Al}_6\text{Si}_7\text{N}_{54}$  coating oxidized at 950 °C for 15 min.

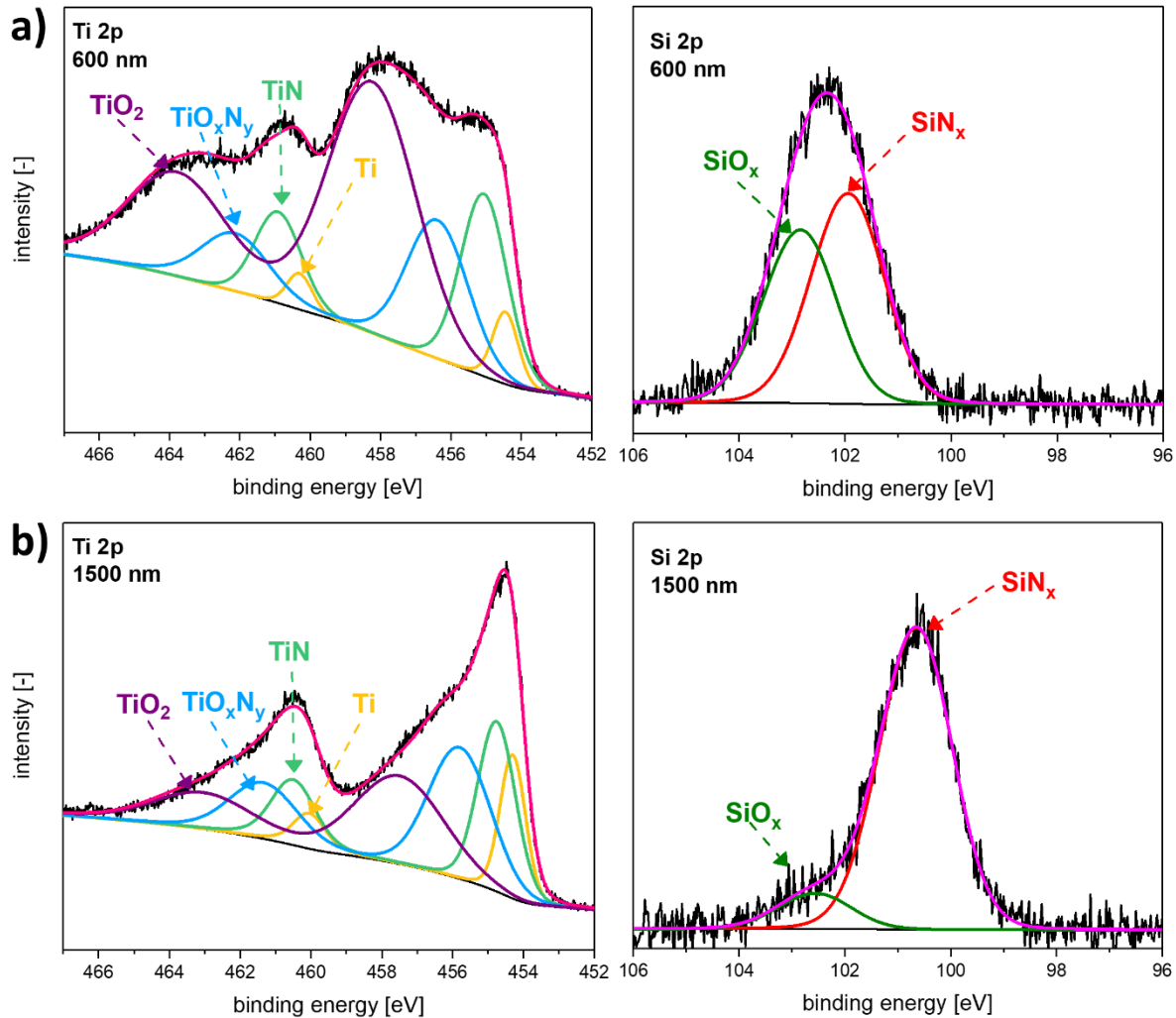


Fig. 7: XPS spectra of the Ti2p and Si2p peaks at sputter depths of 600 nm (a) and 1500 nm (b). A peak fit of the individual contributing components and their respective assignment is shown.

The microstructure of the TiAlSiN coating after oxidation was further monitored by recording SEM images and corresponding EDX maps. In Fig. 8, the images of the coating after oxidation at 950 °C are shown. As already expected from the results obtained by XRD (Fig. 5a), only the top part of the coating – meaning approximately 600 nm – is oxidized while the rest of the coating remains non-oxidized. This is clearly visible when taking a look at the O intensity, which rapidly decreases once the interface between the oxidized layer and the non-oxidized coating area is reached. In literature, usually the formation of a dense  $\text{Al}_2\text{O}_3$  toplayer is reported for TiAlSiN coatings with higher Al



content, which should hinder further O diffusion into the coating [8,12,14,18]. For the  $\text{Ti}_{33}\text{Al}_6\text{Si}_7\text{N}_{54}$  coating investigated in this study, also a thin  $\text{Al}_2\text{O}_3$  toplayer can be found, which however seems to be partly interrupted by the growth of  $\text{TiO}_2$  grains, thus allowing for O to further penetrate the coating. This is in agreement with the quantitative element fraction determined by XPS (Fig. 6), which revealed the highest Al content in the surface region of the coating. Below the  $\text{Al}_2\text{O}_3$  toplayer, a  $\text{TiO}_2$  rich layer depleted in Si can be found, followed by a clearly Si-enriched zone consisting of amorphous  $\text{SiO}_x$ , which is again consistent with results obtained by XPS measurements.

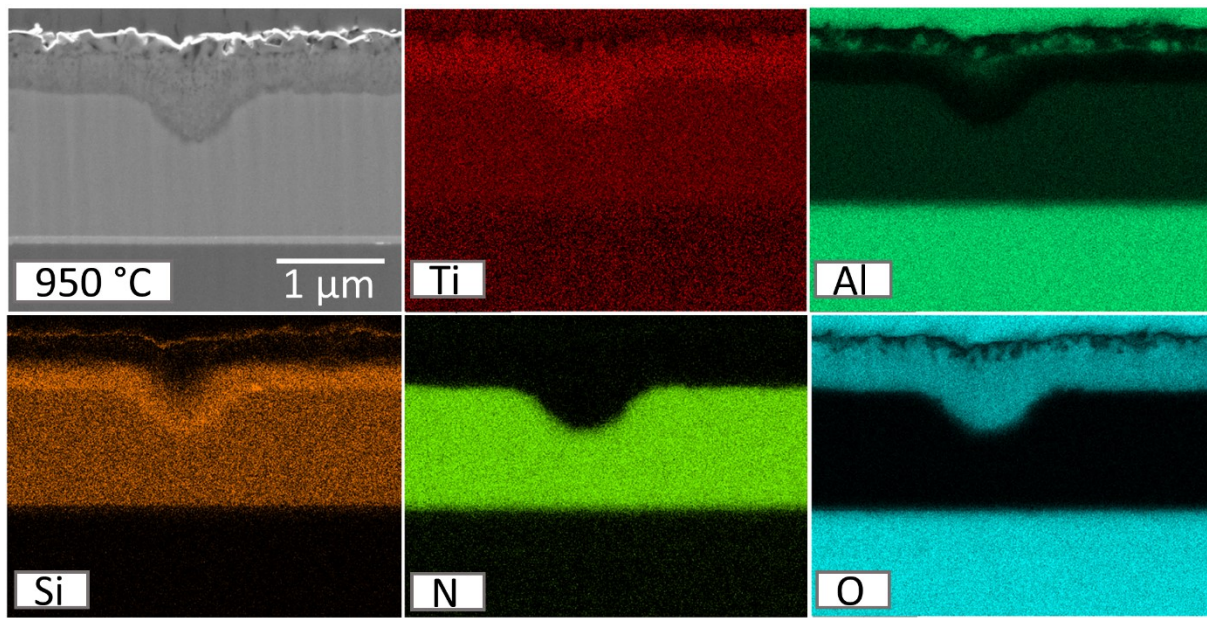


Fig. 8: SEM image and corresponding EDX maps of the  $\text{Ti}_{33}\text{Al}_6\text{Si}_7\text{N}_{54}$  coating on sapphire substrate annealed at 950 °C for 15 min in ambient air.

Further SEM images were taken after annealing the sample in air at a higher temperature of 1100 °C, which are depicted in Fig. 9. The microstructure has drastically changed compared to oxidation of the coating at 950 °C. No  $\alpha\text{-Al}_2\text{O}_3$  top layer is visible, instead strongly enlarged  $\text{TiO}_2$  grains enclosing smaller  $\alpha\text{-Al}_2\text{O}_3$  grains dominate the upper region of the fully oxidized TiAlSiN coating. Below these  $\text{TiO}_2$  grains the coating appears to be porous and still more fine-grained, likely owing to the presence of the

amorphous  $\text{SiO}_x$ , which appears to be exclusively distributed in this lower area of the coating, hindering extensive grain growth of the  $\text{TiO}_2$ . Taking into account the results obtained by SEM investigations, the oxidation mechanism for  $\text{TiAlSiN}$  coatings with low Al contents of  $\sim 6$  at.% can be described as follows: First, Al diffuses towards the surface, forming a thin protective  $\alpha\text{-Al}_2\text{O}_3$  which is subsequently broken by the coarsening of  $\text{TiO}_2$  grains. Thus, more pronounced in-diffusion of oxygen into the coating takes place, leading to further growth of the  $\text{TiO}_2$  grains, which eventually fully enclose the  $\alpha\text{-Al}_2\text{O}_3$  grains. Meanwhile,  $\text{SiO}_x$  is enriched below these enlarged  $\text{TiO}_2$  grains and hinders extensive grain growth in the lower region of the coating.

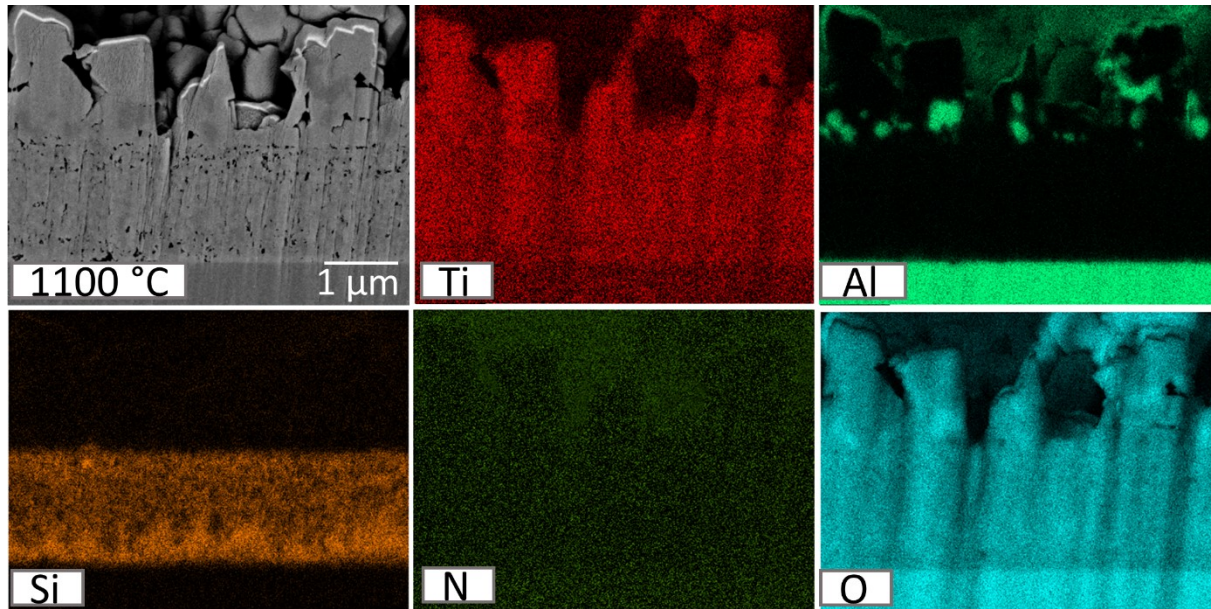


Fig. 9: SEM image and corresponding EDX maps of the  $\text{Ti}_{33}\text{Al}_6\text{Si}_7\text{N}_{54}$  coating on sapphire substrate annealed at  $1100\text{ °C}$  for 15 min in ambient air.

#### 4. Conclusions

Two powdered  $\text{TiAlSiN}$  hard coatings, namely  $\text{Ti}_{37}\text{Al}_2\text{Si}_7\text{N}_{54}$  and  $\text{Ti}_{33}\text{Al}_6\text{Si}_7\text{N}_{54}$ , were investigated regarding their oxidation mechanism up to  $1200\text{ °C}$  by *in-situ* XRD and Rietveld refinement. It was found that both coatings exhibit a good oxidation resistance up to  $\sim 770\text{ °C}$ , followed by the formation of not only  $r\text{-TiO}_2$  but also metastable  $a\text{-TiO}_2$ ,

which can be attributed to the nanocomposite structure of the TiAlSiN coatings consisting of nc-TiAl(Si)N embedded in amorphous SiN<sub>x</sub>. The presence of the amorphous SiN<sub>x</sub> hinders grain growth and thus, promotes the formation of the anatase phase. Furthermore, it was observed that the maximum quantity of the a-TiO<sub>2</sub> phase fraction was significantly higher for the coating with higher Al content of 6 at.%, likely owing to a more sufficiently suppressed grain growth during oxidation, due to more pronounced formation of the protective  $\alpha$ -Al<sub>2</sub>O<sub>3</sub>. Additionally, the microstructure of the compact Ti<sub>33</sub>Al<sub>6</sub>Si<sub>7</sub>N<sub>54</sub> was investigated after oxidation for 15 min at 950 and 1100 °C, respectively. XRD and Raman spectroscopy revealed no full oxidation of the coating at 950 °C and in accordance with *in-situ* XRD measurements of the powdered coating, the presence of a-TiO<sub>2</sub> and r-TiO<sub>2</sub> was confirmed. The amount of a-TiO<sub>2</sub> was then found to strongly decrease at 1100 °C due to transformation into the stable rutile modification. Furthermore, the coating appeared fully oxidized and the presence of  $\alpha$ -Al<sub>2</sub>O<sub>3</sub> could be detected at this temperature. XPS depth-sputter experiments and SEM investigations allowed to gain deeper insight into the microstructure, revealing the presence of an  $\alpha$ -Al<sub>2</sub>O<sub>3</sub> top layer, partly broken by the growth of TiO<sub>2</sub> grains after oxidation at 950 °C. XPS measurements further indicated a superior oxidation resistance of the amorphous SiN<sub>x</sub> phase over the crystalline TiAlN, since at identical sputter depths less SiN<sub>x</sub> was oxidized compared to the nc-TiAlN. SEM images taken after annealing the Ti<sub>33</sub>Al<sub>6</sub>Si<sub>7</sub>N<sub>54</sub> sample at 1100 °C in air revealed an entirely oxidized coating with strongly coarsened TiO<sub>2</sub> grains at the top of the coating, which fully surrounded smaller  $\alpha$ -Al<sub>2</sub>O<sub>3</sub> grains. Below this TiO<sub>2</sub>/Al<sub>2</sub>O<sub>3</sub> top-layer the coating appeared porous and significantly more fine-grained compared to the upper region of the coating, which can be attributed to the presence of SiO<sub>x</sub> in the substrate-near region. The results of this work provide insight into the changes in oxidation mechanism when varying the Al content of TiAlSiN coatings and further establish a profound understanding of the oxidized microstructure of TiAlSiN coatings with low Al content by complementary applying several advanced characterization techniques.

## 5. Acknowledgments

The authors would like to thank Bernhard Sartory (Materials Center Leoben Forschung GmbH) for the SEM investigations. Parts of this research were carried out at ELBE at the Helmholtz-Zentrum Dresden-Rossendorf e.V., a member of the Helmholtz Association (proposal no. 20002122-ST). We would like to thank Dr. Frans Munnik for assistance. The financial support by the Austrian Federal Ministry for Digital and Economic Affairs and the National Foundation for Research, Technology and Development is gratefully acknowledged.

## 6. References

- [1] W. Münz, Titanium aluminum nitride films: A new alternative to TiN coatings, *J. Vac. Sci. Technol. A Vacuum, Surfaces, Film.* 4 (1986) 2717–2725.
- [2] H.A. Jehn, Multicomponent and multiphase hard coatings for tribological applications, *Surf. Coat. Technol.* 131 (2000) 433–440.
- [3] A. Kimura, H. Hasegawa, K. Yamada, T. Suzuki, Effects of Al content on hardness, lattice parameter and microstructure of  $Ti_{1-x}Al_xN$  films, *Surf. Coat. Technol.* 120–121 (1999) 438–441.
- [4] Y.C. Chim, X.Z. Ding, X.T. Zeng, S. Zhang, Oxidation resistance of TiN, CrN, TiAlN and CrAlN coatings deposited by lateral rotating cathode arc, *Thin Solid Films.* 517 (2009) 4845–4849.
- [5] H.G. Prengel, A.T. Santhanam, R.M. Penich, P.C. Jindal, K.H. Wendt, Advanced PVD-TiAlN coatings on carbide and cermet cutting tools, *Surf. Coat. Technol.* 94–95 (1997) 597–602.
- [6] B. Grossmann, M. Tkadletz, N. Schalk, C. Czettl, M. Pohler, C. Mitterer, High-temperature tribology and oxidation of  $Ti_{1-x-y}Al_xTa_yN$  hard coatings, *Surf. Coat. Technol.* 342 (2018) 190–197.
- [7] F. Pei, H.J. Liu, L. Chen, Y.X. Xu, Y. Du, Improved properties of TiAlN coating by combined Si-addition and multilayer architecture, *J. Alloys Compd.* 790 (2019) 909–

- 916.
- [8] L. Chen, B. Yang, Y. Xu, F. Pei, L. Zhou, Y. Du, Improved thermal stability and oxidation resistance of Al–Ti–N coating by Si addition, *Thin Solid Films*. 556 (2014) 369–375.
- [9] M. Pfeiler, J. Zechner, M. Penoy, C. Michotte, C. Mitterer, M. Kathrein, Improved oxidation resistance of TiAlN coatings by doping with Si or B, *Surf. Coat. Technol.* 203 (2009) 3104–3110.
- [10] G.S. Kim, B.S. Kim, S.Y. Lee, J.H. Hahn, Effect of Si content on the properties of TiAl–Si–N films deposited by closed field unbalanced magnetron sputtering with vertical magnetron sources, *Thin Solid Films*. 506–507 (2006) 128–132.
- [11] D. Rafaja, A. Poklad, V. Klemm, G. Schreiber, D. Heger, M. Šíma, M. Dopita, Some consequences of the partial crystallographic coherence between nanocrystalline domains in Ti–Al–N and Ti–Al–Si–N coatings, *Thin Solid Films*. 514 (2006) 240–249.
- [12] Y. Chang, S. Yang, High temperature oxidation behavior of multicomponent TiAlSiN coatings, *Thin Solid Films*. 518 (2010) 34–37.
- [13] T. Chen, Z. Xie, F. Gong, Z. Luo, Z. Yang, Correlation between microstructure evolution and high temperature properties of TiAlSiN hard coatings with different Si and Al content, *Appl. Surf. Sci.* 314 (2014) 735–745.
- [14] A. Vennemann, H. Stock, J. Kohlscheen, S. Rambadt, G. Erkens, Oxidation resistance of titanium–aluminium–silicon nitride coatings, *Surf. Coat. Technol.* 174–175 (2003) 408–415.
- [15] M. Parlinska-Wojtan, A. Karimi, O. Coddet, T. Cselle, M. Morstein, Characterization of thermally treated TiAlSiN coatings by TEM and nanoindentation, *Surf. Coat. Technol.* 188–189 (2004) 344–350.
- [16] L. Xin, Q. Chen, Y. Teng, W. Wang, A. Sun, S. Zhu, F. Wang, Effects of silicon and multilayer structure of TiAl(Si)N coatings on the oxidation resistance of Ti6Al4V, *Surf. Coat. Technol.* 228 (2013) 48–58.

- [17] J. Wu, N. He, H. Li, X. Liu, L. Ji, X. Huang, J. Chen, Deposition and characterization of TiAlSiN coatings prepared by hybrid PVD coating system, *Surf. Interface Anal.* 47 (2014) 184–191.
- [18] L. Zhu, M. Hu, W. Ni, Y. Liu, High temperature oxidation behavior of  $Ti_{0.5}Al_{0.5}N$  coating and  $Ti_{0.5}Al_{0.4}Si_{0.1}N$  coating, *Vaccum.* 86 (2012) 1795–1799.
- [19] I.S. 1832:2017, Indexable Inserts for Cutting Tools, International Organization for Standardization, Geneva, Switzerland, 2017., (n.d.).
- [20] The certification of standard reference material 660C for powder diffraction | NIST, (n.d.). <https://www.nist.gov/publications/certification-standard-reference-material-660c-powder-diffraction> (accessed June 25, 2020).
- [21] NIST, X-ray photoelectron spectroscopy database, (n.d.). <https://srdata.nist.gov/xps/> (accessed January 24, 2023).
- [22] M.P. Seah, T.S. Nunnery, Sputtering yields of compounds using argon ions, *J. Phys. D. Appl. Phys.* 43 (2010) 253001.
- [23] Y. Pan, Z. Luo, Y.-C. Chang, K.-C. Lau, C.Y. Ng, High-Level ab Initio Predictions for the Ionization Energies, Bond Dissociation Energies, and Heats of Formation of Titanium Oxides and Their Cations ( $TiO_n/TiO_n^+$ ,  $n = 1$  and  $2$ ), *J. Phys. Chem. A.* 121 (2017) 669–679.
- [24] D.R. Lide, ed., *CRC Handbook of Chemistry and Physics*, in: 85th ed., CRC Press: Boca Raton, FL, 2006: pp. 9–58.
- [25] W. Assmann, H. Huber, C. Steinhausen, M. Dobler, H. Glückler, A. Weidinger, Elastic recoil detection analysis with heavy ions, *Nucl. Instruments Methods Phys. Res. B.* 89 (1994) 131–139.
- [26] A.O. Eriksson, J.Q. Zhu, N. Ghafoor, M.P. Johansson, J. Sjölen, J. Jensen, M. Odén, L. Hultman, J. Rosén, Layer formation by resputtering in Ti–Si–C hard coatings during large scale cathodic arc deposition, *Surf. Coat. Technol.* 205 (2011) 3923–3930.

- [27] H. Fager, J.M. Andersson, J. Lu, M.P. Johansson Jöesaar, M. Odén, L. Hultman, Growth of hard amorphous Ti-Al-Si-N thin films by cathodic arc evaporation, *Surf. Coat. Technol.* 235 (2013) 376–382.
- [28] A. Flink, T. Larsson, J. Sjölen, L. Karlsson, L. Hultman, Influence of Si on the microstructure of arc evaporated (Ti,Si)N thin films; evidence for cubic solid solutions and their thermal stability, *Surf. Coatings Technol.* 200 (2005) 1535–1542.
- [29] J.Q. Zhu, M.P. Johansson-Jöesaar, P. Polcik, J. Jensen, G. Greczynski, L. Hultman, M. Odén, Influence of Ti-Si cathode grain size on the cathodic arc process and resulting Ti-Si-N coatings, *Surf. Coatings Technol.* 235 (2013) 637–647.
- [30] C.-L. Chang, J.-W. Lee, M.-D. Tseng, Microstructure, corrosion and tribological behaviors of TiAlSiN coatings deposited by cathodic arc plasma deposition, *Thin Solid Films.* 517 (2009) 5231–5236.
- [31] A. Miletić, P. Panjan, B. Škorić, M. Čekada, G. Dražič, J. Kovač, Microstructure and mechanical properties of nanostructured Ti–Al–Si–N coatings deposited by magnetron sputtering, *Surf. Coat. Technol.* 241 (2014) 105–111.
- [32] S. Gates-Rector, T. Blanton, The Powder Diffraction File: a quality materials characterization database, *Powder Diffr.* 34 (2019) 352–360.
- [33] R. Daniel, K.J. Martinschitz, J. Keckes, C. Mitterer, The origin of stresses in magnetron-sputtered thin films with zone T structures, *Acta Mater.* 58 (2010) 2621–2633.
- [34] I.A. Abrikosov, A. Knutsson, B. Alling, F. Tasnádi, H. Lind, L. Hultman, M. Odén, Phase Stability and Elasticity of TiAlN, *Materials (Basel)*. 4 (2011) 1599–1618.
- [35] A. Flink, J.M. Andersson, B. Alling, R. Daniel, J. Sjölen, L. Karlsson, L. Hultman, Structure and thermal stability of arc evaporated  $(\text{Ti}_{0.33}\text{Al}_{0.67})_{1-x}\text{Si}_x\text{N}$  thin films, *Thin Solid Films.* 517 (2008) 714–721.
- [36] L. Zhu, C. Song, W. Ni, Y. Liu, Effect of 10 % Si addition on cathodic arc evaporated TiAlSiN coatings, *Trans. Nonferrous Met. Soc. China.* 26 (2016) 1638–1646.

- [37] S. Carvalho, L. Rebouta, A. Cavaleiro, L.A. Rocha, J. Gomes, E. Alves, Microstructure and mechanical properties of nanocomposite (Ti,Si,Al)N coatings, *Thin Solid Films*. 398–399 (2001) 391–396.
- [38] D. Pilloud, J.F. Pierson, M.C. Marco de Lucas, A. Cavaleiro, Study of the structural changes induced by air oxidation in Ti-Si-N hard coatings, *Surf. Coatings Technol.* 202 (2008) 2413–2417.
- [39] Y. Hu, H.L. Tsai, C.L. Huang, Effect of brookite phase on the anatase-rutile transition in titania nanoparticles, *J. Eur. Ceram. Soc.* 23 (2003) 691–696.
- [40] Y. Moritz, C. Saringer, M. Tkadletz, A. Stark, N. Schell, I. Letofsky-Papst, C. Czettl, M. Pohler, N. Schalk, Oxidation behavior of arc evaporated TiSiN coatings investigated by in-situ synchrotron X-ray diffraction and HR-STEM, *Surf. Coat. Technol.* 404 (2020) 126632.
- [41] L. Kernazhitsky, V. Shymanovska, T. Gavrilko, V. Naumov, L. Fedorenko, V. Kshnyakin, J. Baran, Laser-excited excitonic luminescence of nanocrystalline TiO<sub>2</sub> powder, *Ukr. J. Phys.* 59 (2014) 246–253.
- [42] N. Saoula, S. Djerourou, K. Yahiaoui, K. Henda, R. Kesri, R.M. Erasmus, J.D. Comins, Study of the deposition of Ti/TiN multilayers by magnetron sputtering, *Surf. Interface Anal.* 42 (2010) 1176–1179.
- [43] L.I. Berezhinsky, V.P. Maslov, V.V. Tetyorkin, V.A. Yukhymchuk, Investigation of Al-ZERODUR interface by Raman and secondary ion mass-spectroscopy, *Semicond. Physics, Quantum Electron. Optoelectron.* 8 (2005) 37–40.
- [44] H. Barshilia, B. Deepthi, K.S. Rajam, K.P. Bhatti, S. Chaudhary, Growth and characterization of TiAlN/CrAlN superlattices prepared by reactive direct current magnetron sputtering, *J. Vac. Sci. Technol. A Vacuum, Surfaces, Film.* 27 (2009) 29–36.
- [45] G. Greczynski, D. Primetzhofer, L. Hultman, Reference binding energies of transition metal carbides by core-level x-ray photoelectron spectroscopy free from



- Ar<sup>+</sup> etching artefacts, *Appl. Surf. Sci.* 436 (2018) 102–110.
- [46] G. Greczynski, D. Primetzhofer, J. Lu, L. Hultman, Core-level spectra and binding energies of transition metal nitrides by non-destructive x-ray photoelectron spectroscopy through capping layers, *Appl. Surf. Sci.* 396 (2017) 347–358.
- [47] J.F. Moulder, W.F. Stickle, P.E. Sobol, K.D. Bomben, *Handbook of X-ray Photoelectron Spectroscopy: A Reference Book of Standard Spectra for Identification and Interpretation of XPS Data*, Perkin-Elmer Corporation, Eden Prairie, Minnesota, USA, 1992.
- [48] M.-H. Chan, F.-H. Lu, X-ray photoelectron spectroscopy analyses of titanium oxynitride films prepared by magnetron sputtering using air/Ar mixtures, *Thin Solid Films*. 517 (2009) 5006–5009.
- [49] I. Bertóti, Characterization of nitride coatings by XPS, *Surf. Coatings Technol.* 151–152 (2002) 194–203.
- [50] J. Procházka, P. Karvánková, M.G.J. Vepřek-Heijman, S. Vepřek, Conditions required for achieving superhardness of  $\geq 45$  GPa in nc-TiN/a-Si<sub>3</sub>N<sub>4</sub> nanocomposites, *Mater. Sci. Eng. A.* 384 (2004) 102–116.
- [51] N. Jehanathan, Y. Liu, B. Walmsley, J. Dell, M. Saunders, Effect of oxidation on the chemical bonding structure of PECVD SiN<sub>x</sub> thin films, *J. Appl. Phys.* 100 (2006) 123516.